

The role of lattice defects in the catalytic oxidation of methanol over graphite catalysts

vorgelegt von
Diplom-Chemiker
Emilio Sanchez-Cortezon
aus Alicante/Spanien

Von der Fakultät II – Mathematik und Naturwissenschaften-

Der Technischen Universität Berlin
zur Erlangung des akademischen Grades
Doktor der Naturwissenschaften
- Dr. rer. nat. -

genehmigte Dissertation

Promotionsausschuß:

Vorsitzender: Prof. Dr. Gernot Renger

Berichter: Prof. Dr. Martin Lerch

Berichter: Prof. Dr. Robert Schlögl

Tag der wissenschaftlichen Aussprache: 19. März 2002

Berlin 2002

D 83

Acknowledgment

I would like to thank Prof. R. Schlögl the opportunity to conduct my PhD. thesis in Berlin. When I first visited his lab some years ago, I came with very little knowledge of what a PhD. really means. I got the theoretical background in Alicante, but it was during m PhD. that I got involved more and more in heterogeneous catalysis, characterization techniques, mathematics, statistics, and physical chemistry. It is during the PhD. Thesis that I did really starting to learn about chemistry-physics-and mathematics. I am not alone out there; many other people may think the same about it. One of the things that I have to thank Prof. R. Schlögl is that he always was willing to make something new. When I had a new idea, he did not tell me to stop doing it, "go ahead, try it, and we'll see if it works or not". The freedom that I felt during my PhD. is one of the most important things that I have to thank him, and I choose this opportunity to do it.

Pelu, mi amor, que puedo decir o escribir, para que entiendas lo mucho que me importas y lo mucho que te quiero. Este trabajo lo he escrito mirando tu foto, donde siempre me estabas sonriendo. Te lo dedico a ti especialmente.

Going abroad was one of the most important things that I did in those old days back in Alicante. Escape from my hometown, go abroad, and meet new people. Spending most of my time in the lab, explains that most of my friends in Berlin are people related to the Institute. I have met some very interesting people in the lab like A. Nagy. He was the first person that I met here in Berlin and I received lots of help from him, we had really a very good time going out in Berlin in different clubs and cafes. M. M. Günter, I finished it (ya era hora-It was time) and most of it I owe it to you, my friend. So many hours in the lab and now we did it. J. Find and D. Herein, always together, introduced me to XRD, Hefe Weizen, and many other things. G. Mestl, I have to help you a lot during my Thesis and I learnt a lot concerning heterogeneous catalysis and Raman Spectroscopy. Go ahead with chemometrics to make things easier to see and you are going to be ahead of many classical people. T. Rühle helped me a lot understanding how to mill, to destroy and to create what was going to be the main idea of this PhD. O. Timpe, what can I say Olaf, thanks a lot for helping me so much with that flat. Spending a little of time having a cup of coffee (man, the old coffee machine is gone) can really create a scientific atmosphere to discuss. I don't remember how much time (we spent during measurements, of course) in that room. T. Belz, you are one of the few people that I would say knows what carbon materials are. M. Dieterle, I hope you have fun at BASF World or China, wherever you go, have fun. H. Selber, thanks a lot for the LaTeX tips (I Hate LATEX because I do not understand it). A. Blume, I have to thank you for all the times you helped me when was stacked with my beloved old computer. M. Schur, don't forget what we talked about making New Interesting Scientific Journals, like Jour. of B Science or Jour. N.I compounds. And last, but not of importance: Nadia-Vladimir-Dimitri one of the nicest and friendliest group at Fritz.

Para Pelu, Horses, horses, horses (Patty Smith)

Selbständigkeitserklärung

Hiermit erkläre ich, die vorliegende Arbeit selbständig und ohne fremde Hilfe verfasst zu haben und nur die angegebene Literatur und Hilfsmittel verwendet zu haben.

In der vorliegenden Arbeit wurde die mechanische Aktivierung von Kohlenstoffmaterialien untersucht und ihr Einfluss auf die katalytischen Eigenschaften von gemahlenen Graphit aufgezeigt. Es wurde eine Korrelation zwischen der Struktur des gemahlen Graphits und der katalytischen Aktivität in der partiellen Oxidationsreaktion von Methanol zum Formaldehyd aufgestellt. Es wurde festgestellt, dass die Basalflächen des Graphits für die aktiven Zentren bei der Oxidation von Methanol verantwortlich sind, während Defekte und amorphe Bereiche keine katalytische Aktivität zeigen. Zwei verschiedene Arbeitsbedingungen wurden in der mechanischen Aktivierung untersucht: zum einen trockene Bedingungen und zum anderen die Anwesenheit von Hexan während des Mahlvorgangs. Es wurde festgestellt, dass unter trockenen Bedingungen eine graduelle Zerstörung des Graphitstruktur verursacht wird. Dies wurde durch die Verbreiterung des Röntgenbeugungsreflexen, (00l) und (hk0), und die Zunahme von unerlaubten Ramanpeaks (D) beobachtet. Verlängerte Mahlzeiten verursachten eine zunehmende Zerstörung des Graphitstruktur. Die Anwesenheit von Hexan schützt die kristallographische (hk0) Richtung jedoch nicht die (00l). Diese bevorzugte Zerstörung der Graphitstruktur in der (00l) Richtung verursachte eine deutliche Zunahme der BET Oberfläche. Mahlen unter trockenen Bedingungen erzeugte ebenfalls Defekte und die Umwandlung einer perfekten Struktur in eine amorphe Struktur, und zugleich eine Abnahme des Verhältnisses von Basalfläche:Defekten. Mahlen in der Anwesenheit von Hexan trennte vorzugsweise die Basalflächen und verursachte eine Zunahme im Verhältnis Basalfläche:Defekten. Deswegen zeigten die trocken gemahlenen Proben eine geringere Aktivität im Vergleich zur ursprünglichen Probe und zur gemahlenen Probe in der Anwesenheit von Graphit. Der Grund warum Basalflächen Aktiv für die partielle Oxidation von Methanol vorteilhaft sind, muss auf den metallische Charakter der Basalflächen zurückgeführt werden. Graphit ist in der Basalebene ein Metall mit delokalisierten π -Elektronen. Die π -Elektronen werden zu antibindenden Orbitale des Sauerstoffmoleküls übertragen. Diese Übertragung resultiert in einer Aktivierung und Schwächung der O-O Bindung und erzeugt eine aktivierte Sauerstoffspezies die weiter mit dem Methanolmolekül reagiert.

Schlagwörter: Kohlenstoff, Struktur, Katalyse, Oxidation.

The mechanical activation and its influence in the catalytic properties of graphite were studied in this work. A correlation was found between the structure of milled graphite and the catalytic activity in the partial oxidation of methanol to formaldehyde. It could be proofed, that the basal planes are the active sites for the oxidation of methanol, whereas the defect sites are non-active. Two different working conditions were studied in the mechanical activation of graphite: dry conditions or the presence of hexane in the milling chamber. It was found, that the dry conditions destroyed the structure of graphite. This statement was proven by a widening of the XRD reflections, (00l) and (hk0), and by the increase of the non-allowed Raman peaks associated with a decrease of the particle size. Increasing milling time caused a more dramatic reduction of the graphite crystals and the introduction of disorder. The presence of hexane in the milling chamber protected the (hk0) crystallographic direction, but not the (00l). This preferential reduction of the graphite crystal in the (00l) direction caused a significant increase of the BET surface area. Milling under dry conditions caused the introduction of defects and the decrease of the ratio basal planes:Defects. On the other hand, the presence of hexane caused an increase of that ratio. This is the reason why the dry milled samples showed a smaller activity than the initial and the milled hexane samples. The reason why the basal planes are active for the partial oxidation of methanol comes from their metallic character. Graphite is a metal in the basal plane with delocalised π -electrons. These delocalised π -electrons are transferred to antibonding orbitals in the oxygen molecule causing an activation and weakening the O-O bond giving an activated oxygen species, that can react with methanol.

Keywords: Carbon, Structure, Catalysis, and Oxidation

1	Index of Tables	10
2	Index of Figures	12
3	Index of Formula	16
4	List of Abbreviations	17
5	Introduction	19
5.1	Carbon 19	
5.1.1	Structure, physical and chemical properties of carbon materials	19
5.1.2	Carbon in catalysis	22
5.1.3	Carbon combustion with molecular oxygen	23
5.1.4	Methanol oxidation to formaldehyde	24
5.1.5	Graphite as model system for the oxidative dehydrogenation of methanol	24
5.1.6	Scope of this work	25
5.1.7	Chemometrics Data Analysis	25
5.2	Mechanical activation of solids	26
5.2.1	Tribochemistry	26
5.2.2	Mechanical activation of graphite	27
6	Characterization of the mechanically activated graphite	29
6.1	BET surface area and morphology of the mechanically activated graphite	29
6.1.1	BET surface area	29
6.1.2	Morphology	29
6.2	Geometric structure of mechanically activated graphite	35
6.2.1	X-ray diffraction	35
6.2.2	Raman spectroscopy	47
6.3	Electronic structure of the mechanically activated graphite	67
6.3.1	X-ray photoelectron spectroscopy	67
6.3.2	Ultraviolet photoelectron spectroscopy	70
6.3.3	Electron energy loss spectroscopy	71
6.3.4	K-edge X-ray absorption spectroscopy	71
7	Chemical reactivity of the mechanically activated graphite	73
7.1	Combustion reactivity of mechanically activated graphite	73
7.1.1	Introduction	73
7.1.2	Results 73	
7.1.3	Calculation of apparent activation energies of combustion	75
7.2	Catalytic activity of the mechanically activated graphite	77
7.2.1	Characterization after reaction	77

7.2.2	Thermal desorption spectroscopy of oxygen complexes	78
7.2.3	Catalytic activity in the partial oxidation of methanol	80
8	Conclusions	87
8.1	Structural changes upon milling	87
8.2	Reactivity Changes upon milling	88
8.2.1	Carbon combustion	88
8.2.2	Methanol oxidation	90
9	Appendix 92	
9.1	Appendix A: Experimental apparatus	92
9.2	Appendix B: Methodology	94
9.2.1	Analysis of variance	94
9.2.2	Response surface methods	96
9.2.3	Principal component analysis	100
9.2.4	Partial-least-squares	103
9.2.5	Simplisma	104
10	Bibliography	105
11	Lebenslauf	108

1 Index of Tables

Tab. 1: Reactions catalyzed by carbon from [32].	22
Tab. 2: Set of experimental conditions used to obtain milled samples and nomenclature used for the samples.	28
Tab. 3: XRD results of milled graphite samples. Split-Pearson VII fit of the XRD diffractograms, m_L = low angle exponent associated to asymmetry toward higher d-spacing values and m_R = right angle exponent associated to asymmetry toward lower d-spacing values.	36
Tab. 4: Effect of milling on hexane in the characteristic 100-101 _{hex} and 101-012 _{rhom} reflections. The fit was performed with the Voigt Function. The amount of phases was calculated using the respective H_i values, for hexagonal phase $H_{100}=6$, $H_{101}=12$, and for the rhombohedral phase $H_{101}=4$, $H_{012}=4$.	38
Tab. 5: ANOVA analysis. List of calculated crystallite sizes in Å for the crystallographic [002] and [110] directions calculated from the fitting of the Split-Pearson VII function. Parameter A denotes the duration of the milling ($A_1= 0$, $A_2= 72$, and $A_3= 168$ hr) and parameter B denotes the presence of hexane during the milling ($B_1=no$, $B_2= yes$)	40
Tab. 6: Complete two-way ANOVA summary showing the SS for the parameters A, B, the interaction A×B, and the experimental error. F test with 99.9% confidence level.	40
Tab. 7: Evolution of the intensity ratios I_D/I_G and I_D/I_G and the position of the G band upon milling.	50
Tab. 8: PCA results corresponding to the classification of Raman spectra. Laser power effect (0.14 and 14 mW) in the Raman spectrum for sample d72.	56
Tab. 9: Percentage of variance captured for the X and Y descriptors for several scalings before PLS analysis.	59
Tab. 10: SIMPLISMA analysis of the Raman spectra for the mechanically activated samples. The starting material and HOPG were included in the analysis. The mean and the standard deviation of each pure spectral component: pristine graphite band at 1580 cm^{-1} and milled with bands at 1150, 1333, and 1620 cm^{-1} is shown for each sample.	63
Tab. 11: Comparison of the C1s fitting for HOPG, the starting sample and the h168 and d168 samples. The sample h168 was sputtered in Ar^+ at 3keV for 20 min. The C1s signal of HOPG was fitted with the asymmetric Gaussian convoluted DS function and the other peaks with GL functions. Γ and C are the respective FWHM and the content of each signal.	68
Tab. 12: Comparison of the O1s fittings for the starting sample and the milled samples h168 and d168. Additionally, the h168 sample was sputtered with Ar^+ for 20 min with energy of 3 keV. All fits were conducted with combined Gauss-Lorentzian functions.	69
Tab. 13: Comparison between the on-set and end temperature of combustion of the two catalyst series in the TPO-DTG profiles Experimental conditions: heating rate 0.5 K/min, reactant flow 100 ml ($O_2:N_2=1$) /min}. Apparent activation energies calculated from the TPO experiments using the Kissinger's method [34].	75
Tab. 14: Effect of the reaction $MeOH:O_2$ in the structural parameters of the milled graphite catalysts. Split-Pearson VII fit of the XRD diffractograms, m_L = low angle exponent associated to asymmetry toward higher d-spacing values and m_R = right angle exponent associated to asymmetry toward lower d-spacing values (a.r. = after reaction).	77
Tab. 15: List of experiments conducted for the RSM studies with the starting AF-s, and the mechanically activated samples d72, d168, and h168.	80
Tab. 16: List of coefficient for the different models calculated for the yield of CH_2O with the standard deviation of each coefficient. The sign † denotes coefficients, which are statistically significant after conducting the t-test with a confidence level of 99%.	81
Tab. 17: ANOVA Table for the model Y_{CH_2O} (%) for the studied samples h168, <i>starting</i> , d72, and d168, showing the explained sum of squares by the model, the residual sum of squares, and the total sum of squares. The calculated F- and R^2 -value are also shown. ° Model corrections: terms	

O_2 , O_2^2 , and $T \times O_2^2$ were omitted.

82

Tab. 18: Results of Principal component analysis with data generated as $y=5+2x$ and $z=y+2x$. 102

2 Index of Figures

Abb. 1: Structure of diamond showing the tetrahedral coordination of C. The lines indicate the cubic unit cell containing 8 C atoms [66].	19
Abb. 2: Structure of the α –(hexagonal) and β –(rhombohedral) forms of graphite.	20
Abb. 3: C60 Structure.	21
Abb. 4: Bent sheets are stacked concentrically and randomly representing a fullerene black sample (A). On the other hand, a few of those stacks are oriented with the a-axis parallel to the electron beam (B). Covalent bonded between these sheets affect the graphitizability of the sample (C) from [61].	21
Abb. 5: Structural model of carbon blacks [61].	22
Abb. 6: Effect of the carbonaceous structure in the partial oxidation of methanol to formaldehyde. TPRS-experiment with the reaction conditions of MeOH:O ₂ ratio of 3.01, the GHSV of 11700 h ⁻¹ and 5 K/min as heating rate.	24
Abb. 7: Effect of the milling time and the experimental conditions in the evolution of the BET surface area.	29
Abb. 8: SEM micrograph of the <i>starting</i> material.	30
Abb. 9: SEM micrograph of the materials d72 (top) and d168 (bottom).	30
Abb. 10: SEM micrograph of the milled material h168.	31
Abb. 11: TEM micrograph of the <i>starting</i> material.	31
Abb. 12: TEM micrograph of the milled material d168.	32
Abb. 13: TEM micrograph of the milled material d168.	32
Abb. 14: TEM micrograph of the milled material d168.	33
Abb. 15: TEM micrograph of the milled material h168 (left). The right image shows the d-spacing along the [110] direction.	33
Abb. 16: ED pattern for the starting material (left), d168 (middle), and h168 (right).	34
Abb. 17: XRD diffractograms of the milled samples in presence and absence of hexane after 168 hr compared to the <i>starting</i> material, showing regions corresponding to the 002 reflections (B), 100-101 _{hex} ; 101-012 _{rhom} (C), and 110 (D) analyzed in this work.	36
Abb. 18: Progression of the 002 reflection with milling time in the presence (left) and absence (right) of hexane. The absence of hexane in the milling chamber resulted in a drastic increase of the FWHM of this reflection, a shift to higher d-spacing values, and to an asymmetry to higher d-spacing values compared to milling in the presence of hexane.	36
Abb. 19: Evolution with milling time of the 100-101 _{hex} and 101-012 _{rhom} reflections in the presence (left) and absence of hexane (right).	37
Abb. 20: Evolution with milling time of 110 reflection in the presence (left) and absence (right) of hexane.	38
Abb. 21: ANOVA results: plot of effects and interaction between the milling duration and the experimental milling conditions in the [002] crystallographic direction (× effect of time in the reduction of the crystallite size in the [002] direction, squares experimental values for d series, and circles for h series).	41
Abb. 22: ANOVA results: plot of effects and interaction between the milling duration and the experimental milling conditions in the [110] crystallographic direction (× effect of time in the reduction of the crystallite size in the [110] direction, squares experimental values for d series, and circles for h series).	41
Abb. 23: Simulation of increasing the d-spacing value in the [002] direction (above) and hexagonal	

-> rhombohedral transformation (bottom).	42
Abb. 24: Theoretical diffractograms simulating an increase of the d-spacing value of the basal planes from $d_{002}=3.35$ to 3.38 Å. Right plot shows the displacement of the 002 reflection upon increasing d-spacing distance.	43
Abb. 25: Calculated diffractograms showing the increase of the amount of the rhombohedral graphite upon milling. The <i>starting</i> and milled graphite AF-s after 72 hours in presence of hexane were compared with the theoretical diffractograms (top). Figure bottom shows the increase of the rhombohedral 101-012_{\rho} reflections from 0 to 100% upon milling.	43
Abb. 26: Structural model: Rotation along the c-axis, [001] direction. Structure of hexagonal graphite showing the characteristic ABABA stacking with the three main 002, 100, 110 directions. The rotation of graphite sheets along the c-axis, [001] direction creates interferences, known as Moiré patterns, causing the asymmetries of the 110 reflection observed with XRD.	44
Abb. 27: Calculated diffractograms simulating a rotation of basal planes along the [001] direction (left). Comparison of two rotation models, Rotation {z-1} and 2, showing the appearance of hk0 reflections at higher 2θ compared to the expected position 110 (right).	44
Abb. 28: Structural model: Rotation structural models along the a-axis. Normal and side view of the resulting tilted graphene planes.	45
Abb. 29: Calculated diffractogram simulating a rotation of graphene planes along the a-axis (left). Due to the rotation along the a-axis a peak appears at higher d-values, marked by \times , and another one at lower d-values, marked by $+$. This latter peak has no physical meaning. Comparison of two rotation models showing the appearance of 00l and hk0 reflexes at higher 2θ compared to the expected positions of the 002 and 110 reflections (right).	46
Abb. 30: The graphite stretching modes: Raman and Infrared active vibrational modes [17].	48
Abb. 31: Evolution of the Raman spectra for the samples milled in the absence (left) and in the presence (right) of hexane. The stretching modes correspond to the first phonon mode for graphite appearing at 1333 , 1580 , and 1618 cm^{-1} , respectively.	50
Abb. 32: First-order Raman spectra of RFL and AF-s graphite measured with 14 mW laser power. These two samples studied are representative for crystalline carbon; note the low intensities of the 1333 and 1620 cm^{-1} bands.	51
Abb. 33: Dependence of the structure of the studied sample with the effect of the laser power on the position of the E_{2g} vibrational mode. Graphite RFL $^{\circ}$, larger flakes, showed almost no effect, whereas AF-s (+), smaller flakes, showed a downshift from 1581 to 1576 cm^{-1}	52
Abb. 34: Representative spectra taken for the sample d72 with two different laser powers: (A) 0.14 mW , (B-C) 14 mW . The evolution of the spectra recorded with 14 mW led to the transformation of spectra of group B into C.	53
Abb. 35: 3D-Plot of the relationship between the band ratios I_D/I_G , I_D/I_D , and I_D/I_G for the sample d72 measured at different laser powers 0.14 and 14 mW	54
Abb. 36: Plot of scores, t, corresponding to the first and second PC for the X matrix descriptor corresponding to the problem of the laser power [0.14 - 14 mW].	55
Abb. 37: (A) Mean 1st-order Raman spectra of the sample d72 measured with 0.14 and 14 mW laser power. (B-C) Loading plot, p, corresponding to the 1st and 2nd PC. The spectral region marked by \times and $+$ represent two negatively correlated graphite species.	56
Abb. 38: Effect of the laser power and graphite structure on the first-order Raman	57
Abb. 39: Dependence of the Raman intensity for the mechanically activated graphite samples under dry conditions on the milling time.	57
Abb. 40: Direct correlation between decrease of XRD coherence lengths in the [002] direction and the increase of the I_D/I_G intensity ratio.	58
Abb. 41: Direct correlation between decrease of XRD coherence lengths in the [110] direction and	

the increase of the I_D/I_G intensity ratio.....	58
Abb. 42: First component p1 for the X (left) and q1 for the Y descriptor (right). The first component corresponding to the Raman data set (left) has three main features, two positively correlated, marked by \times , appearing at 1333 and 1620 cm^{-1} and one feature negatively correlated with the above cited at 1580 cm^{-1} , marked by +. The first component found in the XRD data set (right) has several positively correlated features which correspond to the broadening of the graphite reflections, marked by \times , and several features negatively correlated with the latter ones, marked by +, which correspond to the original sharp graphite reflections.	60
Abb. 43: Score plot of the first component t1 for the X descriptor and u1 for the Y descriptor. As the first component t1 increases upon milling so increases the first component u1.....	60
Abb. 44: Residuals corresponding to a milled sample after 168 hours in the absence of hexane for the Raman spectra (left) and for the XRD diffractogram (right).	61
Abb. 45: Comparison of different PLS Raman-XRD models. (A) 1st PC, p1, of the PLS analysis for 3 different models: a) Y descriptor, whole XRD-diffractogram; b) Y descriptor, [002] direction; and c) Y descriptor, [110] direction. Positively (\times) correlated modes and negatively (+) correlated mode. (B) 1st PC, q1, of the Y descriptor: whole XRD-diffractogram line (solid line), (box) model for the [002] direction, see the broadening and asymmetry (\times) and the sharp 002 reflection (+). (C) 1st PC, q1, of the PLS analysis of the Y descriptor: whole XRD-diffractogram (right) and model of the [110] direction (left). See the positive correlation of broadening and asymmetry (\times) and the negative correlation of the sharp 110 reflection (+).	62
Abb. 46: Pure spectral components found in the first-order Raman spectrum of graphite. The first spectral component has only one stretching mode at 1580 cm^{-1} (bottom), assigned to the E_{2g} vibrational mode of HOPG. The second one presents two main bands appearing at 1333 and 1620 cm^{-1} , and a slight shoulder at 1150 cm^{-1} (top).....	63
Abb. 47: 3D-Phonon dispersion curves calculated from the Born-von Kármán ¹ model (left) and the pure spectral components found with SIMPLISMA (right).	64
Abb. 48: Electron diffraction pattern of the <i>starting</i> material showing the 100, 110 and -110} reflections. The [100], [110], and [-110] directions as well as their respective d-spacing values are showed. The [110] and [-110] have different d-spacing values and are not crystallographic similar.	65
Abb. 49: The [110] and [-110] crystallographic directions in the graphite lattice. Both directions are clearly different, with different d-spacing values and different number and position of carbon atoms in each direction.	65
Abb. 50: Illustration proposed for the simultaneous appearance of two Raman forbidden modes. Any cut in the graphite lattice represented by the dotted line or any point defect affects both the [110] and [-110]} crystallographic directions.	66
Abb. 51: C1s XPS spectra of the milled graphite samples after 168 hours in both presence and absence of hexane, HOPG, <i>starting</i> material, and sputtered graphite after milling in the presence of hexane for 168 hours.	67
Abb. 52: O1s XPS spectra of the milled graphite samples after 168 hours in both presence and absence of hexane, <i>starting</i> material, and sputtered graphite after milling in the presence of hexane for 168 hours.	69
Abb. 53: UPS Hell valence band spectra of the milled graphite samples after 168 hours in both presence and absence of hexane, <i>starting</i> material, and sputtered h168 sample.	70
Abb. 54: EELS spectra of <i>starting</i> graphite (bottom curve), milled graphite in presence and absence of hexane after 168 hours, and sputtered h168 sample (top curve).	71
Abb. 55: XAS comparison of for the starting (bottom curve) and milled graphite in absence of hexane after 168 hours (top curve).	72
Abb. 56: Effect of the milling time in the reactivity of the dry milled samples.	74
Abb. 57: Effect of the milling time in the reactivity of the hexane milled samples.	74

Abb. 58: TDS spectra for the desorption of CO ₂ and H ₂ corresponding to the starting and d168 samples	78
Abb. 59: TDS spectra for the desorption of CO and H ₂ O corresponding to the starting and d168 samples	79
Abb. 60: TDS spectra of CO ₂ desorption after O ₂ 748 K treatment of the <i>starting</i> and d168 samples.	79
Abb. 61: CH ₂ O response surface calculated for the sample h168.	82
Abb. 62: CH ₂ O response surface for the <i>starting</i> sample.	83
Abb. 63: CH ₂ O response surface calculated for the sample d72	84
Abb. 64: CH ₂ O response surface calculated for the sample d168.	84
Abb. 65: Effect of increasing temperature on the CH ₂ O yield. Progressive milling in the absence of hexane leads to a decrease of activity.	85
Abb. 66: CH ₂ O-selectivity vs. MeOH-conversion for the (+) starting, (×) h168, and (box) d72 samples	86
Abb. 67: Comparison of the combustion reactivity for the starting and d168 sample normalized to the surface area.	89
Abb. 68: Decomposition of the data matrix X into the scores, T , (eigenvalues) and loadings, P , (eigenvectors) matrices (top) and decomposition using the SVD algorithm (bottom).....	101
Abb. 69: Example of PCA analysis. A) 3-D plot of generated data with $y=5+2x$ and $z=y+2x$. B) Score plot t_1 vs. t_2 . C) Loading plot of the first principal component.....	102

3 Index of Formula

Formula carbon combustion:

Eq. 1-5 23,88

Formula catalyzed reactions-mechanical activation:

Eq. 7-8 27

Formula Raman spectroscopy:

Eq. 9-10 47

Formula Kissinger Method:

Eq. 11 75

Formula Catalysis:

Eq. 12-15 80,82-83

Formula Analysis of Variance:

Eq. 16-20 93-95

Formula Response Surface Methods:

Eq. 21-43 95-99

Formula Principal Component Analysis:

Eq. 44-46 100

Formula Partial Least Squares:

Eq. 47-50 102

Formula Simplisma:

Eq. 51-55 103

4 List of Abbreviations

$A_{2u}+2B_{2g}+E_{1u}+2E_{2g}$: Vibrational modes

ANOVA: Analysis of Variance

Å: Angstrom

BET: Surface area Brunauer-Emmett-Teller

BSU: Basic structural unit

C_a : Basal active sites

C_b : Defect sites

DTG: Differential thermogravimetry

D: Disorder Raman Mode

E_A : Activation energy

ED: Electron diffraction

EELS: Electron energy loss spectroscopy

FWHM Γ : Full width half maximum

F: Fischer test value

G: Active raman mode

GHSV: Gas-hourly-space-velocity

Hi: Highly oriented pyrolytic graphite

HOPG: Multiplicity of the crystallographic planes

L_a : Crystallite size in the graphite a axis

m_L : left angle asymmetry exponent

m_R : right angle asymmetry exponent

MLR: Multiple linear regression

ν : Degrees of freedom

PCA: Principal component analysis

PC: Principal component

ϕ : Heating rate

PLS: Partial-least-squares

RSM: Response Surface Methods

SEM: Scanning electron microscopy

SS: Sum of squares

Simplisma: Simple-to-use interactive self-modeling mixture analysis

TEM: Transmission electron microscopy

TDS: Temperature desorption spectroscopy

TG: Thermogravimetry

T_{max}: Temperature where the maximum oxidation occurs

TPO: Temperature programmed oxidation

TPRS: Temperature programmed reaction spectroscopy

UHV: Ultra high vacuum

UPS: Ultraviolet photoelectron spectroscopy

V: Variance

XPS: X-ray photoelectron spectroscopy

XRD: X-ray diffraction

X: Matrix X,...

Y_{CH₂O}: Yield of formaldehyde

5 Introduction

5.1 Carbon

This chapter discusses the structure, physical and chemical properties of carbon materials. The different applications of carbon materials in catalysis are introduced and an overview of the catalytic partial oxidation of methanol to formaldehyde is presented. The investigation of graphite as model catalyst for the oxidation of methanol and the role of lattice defects in the carbon combustion and the partial oxidation of methanol are introduced as objectives for this PhD. thesis.

5.1.1 Structure, physical and chemical properties of carbon materials

Carbon was known since ancient times in the form of charcoal and soot and was mainly used as a source of energy or as a pigment. Later in the XVII century it was recognized as a chemical element. Diamond and graphite were known to be different forms of carbon, as well as the relationships between carbon, charcoal, CO₂, and carbonates at the end of that century. Carbon occupies the seventeenth place of terrestrial element abundance and occurs as a native element (graphite, diamond) and in combined form mainly as carbonates. In addition, it forms a minor part of the atmosphere as CO₂ [26]. The great bulk of carbon is immobilized in the form of coal, limestone, chalk, dolomite and other deposits.

5.1.1.1 Carbon materials

- Diamond

Diamond is a solid in which each carbon atom is sp³ hybridized and tetrahedrally coordinated by 4 other carbon atoms at a distance of 1.5445 Å. The carbon atoms are arranged in a lattice of cubic symmetry, as shown in Abb 1. In addition, a rare hexagonal modification of diamond called Lonsdalite exists. As in diamond, each carbon atom is tetrahedrally coordinated, but the tetrahedra are hexagonal arranged with a wurzite-type structure.

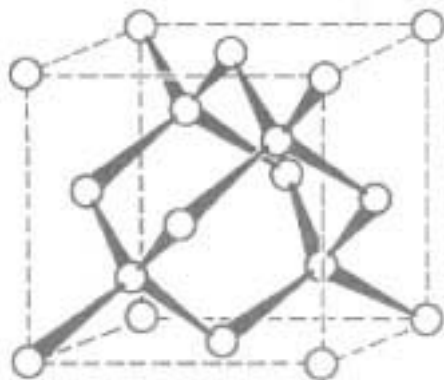


Abb. 1: Structure of diamond showing the tetrahedral coordination of C. The lines indicate the cubic unit cell containing 8 C atoms [66].

Diamond at normal temperatures and pressures is a metastable modification of graphite and is interconvertible to graphite by heating above 1900 K in inert atmospheres. It is an electric insulator with an extreme hardness and high heat conductance. Its extreme hardness makes diamond to one of the most important materials used for cutting tools.

- Graphite

Graphite occurs as α -(hexagonal) and β -(rhombohedral) graphite and is a black lamellar solid. Whereas the stacking order in α -(hexagonal) of the carbon sheets is ABAB..., the stacking order of β -(rhombohedral)-graphite is ABCABC.... Abb. 2 shows both structures.

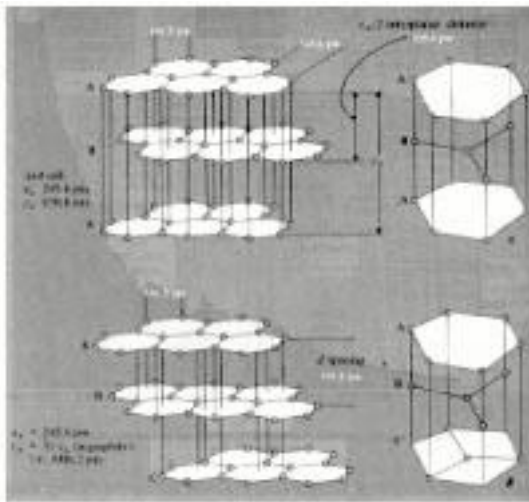


Abb. 2: Structure of the α -(hexagonal) and β -(rhombohedral) forms of graphite.

The C-C distance in both forms of graphite is 1.415 Å and the interlayer distance between carbon sheets is 3.354 Å. α -(hexagonal)-graphite is the most stable form at normal pressures and temperatures. Both forms are interconvertible by heating above 1300 K ($\beta \rightarrow \alpha$) [26] or by milling $\alpha \rightarrow \beta$) [4,7]. In the sheets, each carbon atom is threefold coordinated and sp^2 hybridized sharing one electron to a delocalized system. Weak forces, sometimes wrongly referred to as van-der-Waals, exist between the carbon sheets. The differences between forces strongly covalent in the sheets and weak between sheets results in a strong anisotropy of this solid. The delocalized π system in the sheets is responsible for the good electronic conductivity of graphite within the sheets resulting in metallic properties (semimetal), whereas the poor electron conductivity perpendicular to the graphite sheets results in insulating properties.

- Fullerene

Other modifications of carbon are the fullerenes which are molecular solids discovered in the 80's by Kroto and coworkers [38]. The molecular structure of the C₆₀ molecule is depicted in Abb. 3, in which 60 carbon atoms form a perfect symmetrical closed structure. In each C₆₀ molecule, there are 10 hexagons and 12 pentagons.



Abb. 3: C60 Structure

C60 can be produced with the graphite discharge method [5]. A strong electric current is set between two graphite electrodes in a chamber in inert atmospheres and the graphite anode is vaporized. The C60 molecules are formed in the gas phase as well as a by-product called fullerene black. The yield of C60 and higher C-containing molecules such as C70 is very low, around 5-9 % [5]. The by-product fullerene black is the main product and is a black amorphous solid. A model of its structure is presented in Abb. 4.

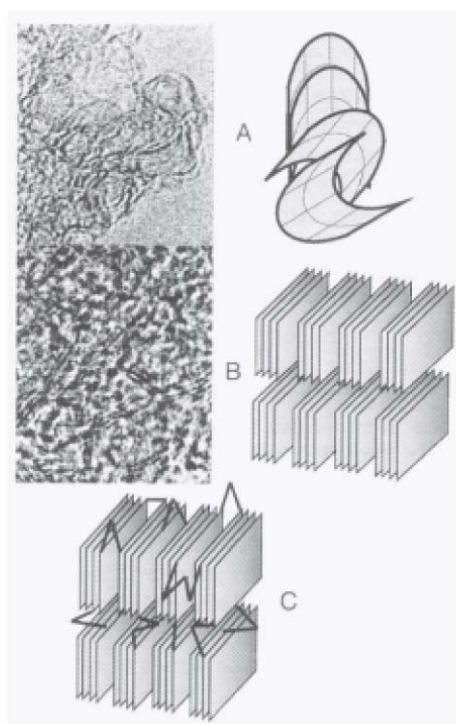


Abb. 4: Bent sheets are stacked concentrically and randomly representing a fullerene black sample (A). On the other hand, a few of those stacks are oriented with the a-axis parallel to the electron beam (B). Covalent bonded between these sheets affect the graphitizability of the sample (C) from [61].

These materials contain in its structure both six- and fivefold coordinated carbon rings, which confer them interesting reactivity properties. Aggregates of small bent graphite sheets build up their structures.

- Other carbon materials

Other important carbon materials are activated carbons, carbon blacks, and carbon fibers. These carbon materials are industrially produced from natural sources in the case of the activated carbons, from the combustion of hydrocarbons in oxygen deficient atmospheres in the case of carbon blacks [61], and from polymerization reactions in the case of both activated carbons and carbon fibers. The activated carbon and carbon fibers materials are activated physically and/or chemically to achieve high surface areas. This activation is a controlled oxidation of the surface. The high porosity of these materials confer them very good adsorbent properties for which purpose they are mainly used.

The structure of carbon blacks resembles that of fullerene blacks, see Abb. 5. Very small graphite crystallites form rounded aggregates, but in this case the sheets are not bended but straight.

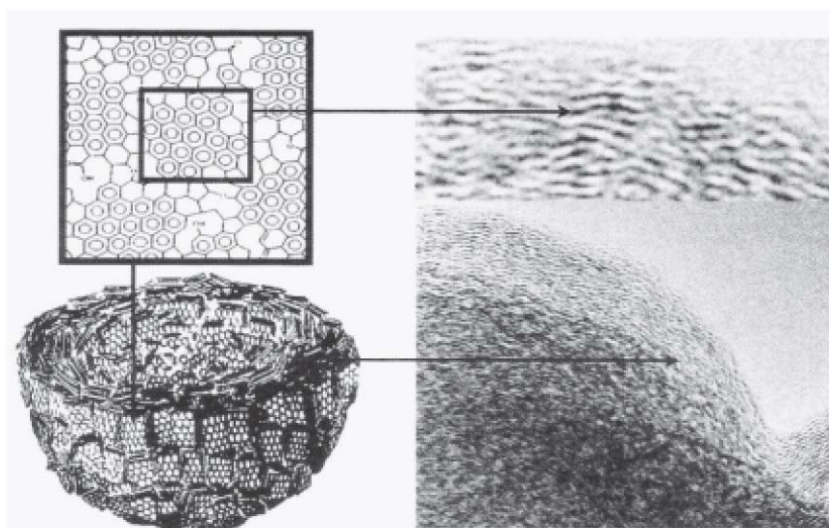


Abb. 5: Structural model of carbon blacks [61].

5.1.2 Carbon in catalysis

Carbon, in the forms of blacks and activated carbon, is used mainly as a support for the active phase in heterogeneous catalysis [56]. Examples of this application are the hydrogenation of functionalized hydrocarbons [56] and the synthesis of NH_3 [2,25]. In hydrogenation reactions, the main purpose of the carbon support is to provide a large surface area to maintain an active metal phase such as platinum highly dispersed. The catalyst developed for the NH_3 synthesis contains promoted ruthenium supported on a special form of carbon with a high ratio of basal to prism surfaces. This morphology controls the performance and the stability of the catalyst.

Carbon can also be used as catalyst on its own [32]. Carbon catalyzes the formation of phosgene (COCl_2) and diverse chlorinated alkenes and alkanes. Carbon also works as a catalyst in several oxidation reactions summarized in Tab. 1:

Tab. 1: Reactions catalyzed by carbon from [32].

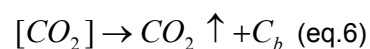
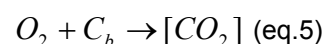
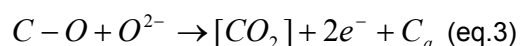
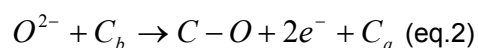
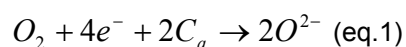
Formation of
Phosgene

Cl ₂ S
Chlorinated alkanes and alkenes
<u>Oxidation of</u>
H ₂ S to S
SO ₂ to H ₂ SO ₄
NO to NO ₂

The inorganic impurities present in the carbon, due to the natural origin of the sample, is a factor that surely influences the catalyst activity. Such influence can be either positive, if it catalyzes or co-catalyzes the desired reaction, or negative, acting as a poison or catalyzing undesired reactions. It is very important to determine exactly what acts as the real catalyst and if the presence of small impurities interfere or not in the reaction studied. The latter can be avoided studying model systems with a controlled level of purity. A real industrial catalyst has a higher degree of complexity, which makes their fundamental study a difficult and long task.

5.1.3 Carbon combustion with molecular oxygen

Carbon combustion has received much interest in research [3,27,43,47,61,81,8]. The main application of coal is still its combustion for the production of energy. The following reactions schematize the combustion of carbon with molecular oxygen:



The activation of adsorbed oxygen, eq. 1, is the initial step in the combustion of carbon [43]. Due to the metallic character of the graphite basal planes (C_a) with delocalized π -electrons, these π -electrons are donated to π^* antibonding orbitals of the O_2 molecule resulting in a weakening and, thus, activation of the O-O bond. These activated oxygen species, O^{2-}_{ads} and/or O_{ads} [3], will diffuse on the basal plane until they reach a point defect, edge, or a terrace, (C_b), eq. 2. There, they stick to the substrate, return the electrons to the carbon material and form a covalent bond with the substrate, eq. 3. The mobility of oxygen was evidenced by Walker and coworkers [81] studying the combustion of graphon with both $^{16}O_2$ and $^{18}O_2$ and measuring the product distribution of $C^{16}O$ - $C^{18}O$ and $C^{16}O_2$ - $C^{18}O_2$ - $C^{16}O^{18}O$. The sum of the previous equations is eq. 4. As the temperature is increased, the desorption of carbon oxygen-groups is facilitated, resulting in the combustion of carbon and in an increased rate of the cycle oxygen-activation-defect fixation, eq. 5.

The fundamental idea of using carbon as an oxidation catalyst is to interfere with the activation-fixation cycle by co-adsorbing an organic acceptor for activated oxygen using C_a as active site avoiding C_b as destructive site. This substrate should react with oxygen and desorb easier from the catalytic surface as in the case of more conventional oxidation catalysts such as oxides and metals. The role of surface-oxygen groups could be beneficial in helping to chemisorb (polarity) or activate (acid-base character of OH-functions) the organic substrate.

5.1.4 Methanol oxidation to formaldehyde

Formaldehyde serves as an intermediate in numerous industrial processes [77], explaining the importance of its synthesis from the industrial point of view. In 1867 Hoffman synthesized for the first time CH_2O passing $MeOH$ over a heated Pt spiral. The two main catalysts used nowadays are silver (BASF Process) and a mixed oxide composed of molybdenum and iron (Formox Process) [77]. The search for new technical catalysts is not only motivated by the fundamental understanding reached in the silver-oxygen system [41,48], but also by the desire to set-up small scale productions with easy-to-use catalysts.

5.1.5 Graphite as model system for the oxidative dehydrogenation of methanol

The catalytic activity of carbon materials has been addressed only very recently. The catalytic activity of carbon materials was reported in the partial oxidation of methanol to formaldehyde [59]. Considering carbonaceous samples, the carbon structure plays a fundamental role for the catalytic activity. Figure \ref{xch2oa} shows the activity of diverse carbon materials such as: polycrystalline graphite, activated carbon, carbon black and fullerene black.

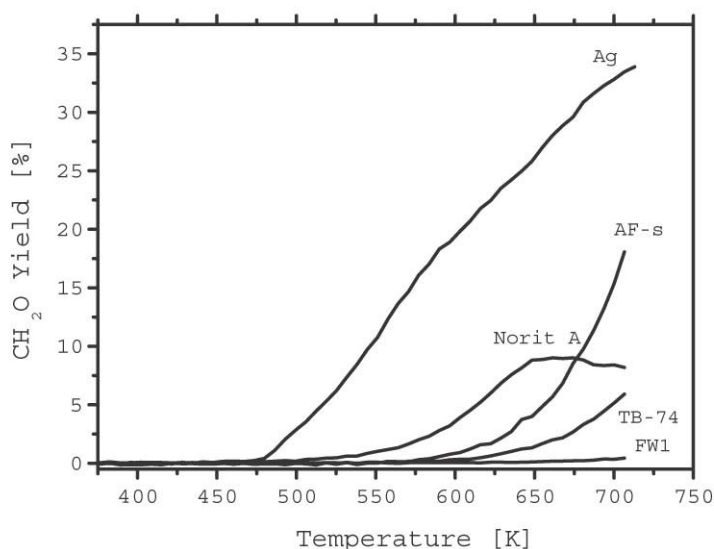


Abb. 6: Effect of the carbonaceous structure in the partial oxidation of methanol to formaldehyde. TPRS-experiment with the reaction conditions of $MeOH:O_2$ ratio of 3.01, the GHSV of 11700 h^{-1} and 5 K/min as heating rate.

The characteristic structure of low-surface area graphite exhibiting a structure with large well-ordered basal planes seems to be positively correlated with the selective oxidation of methanol. Amorphous carbonaceous structures with high-surface areas are not able to catalyze the oxidation of methanol, but gasify under reaction conditions. From these results shown in Figure \ref{xch2oa}, the presence of defects seems to be negatively correlated with the catalytic activity.

5.1.6 Scope of this work

The scope of this work is to elucidate the role of defects in the carbon combustion and in the partial oxidation of methanol to formaldehyde. Since amorphous carbon samples which have a high density of defects do not catalyze the partial oxidation of methanol, the introduction of defects into a well crystalline sample, such as graphite, should decrease the activity of the catalyst. To this end mechanical treatments were performed on graphite AF-s introducing different kinds of defects. The milled samples were characterized with numerous bulk and surface sensitive techniques and the reactivity of the mechanically activated samples was studied in the combustion and in the partial oxidation of methanol. The combustion of carbon materials was used as a chemical probe for the effect of the introduction of defects.

5.1.7 Chemometrics Data Analysis

In this Thesis several statistical data analysis methods were used to help us finding and understand the correlations between variables and to determine significant effects of selected variables. Traditionally statistical methods such as Analysis of Variance (ANOVA) and Response Surface Methods (RSM) were used in the analysis of characterization and catalysis data. ANOVA is a statistical tool used in experimental design and quality engineering [71] to determine the significance of effects and interactions from various parameters. ANOVA is employed to determine whether differences between sets of samples are significant with respect to the difference within a sample's set. RSM play an important role in the field of experimental design [10,36,55] and are based on the least squares estimation of a function (variable measured) which depends on a certain number of independent variables.

Additionally less traditional statistical methods were also employed in the analysis of the obtained data. The large amount of data provided nowadays by the research point out the necessity of using statistical procedures. Patterns of association exist in many data sets, but the relationships between samples can be difficult to discover when the data matrix exceeds three or more variables. Furthermore, the experimental spectra usually contain mixtures of different components, which may influence the spectra. In many cases the pure spectrum of a determined compound is not available in the literature. Exploratory data analysis can reveal hidden patterns in complex data by reducing the information to a more comprehensible form. Such a chemometric analysis can expose possible outliers and indicate whether there are patterns or trends in the data. Exploratory algorithms such as principal component analysis (PCA) are designed to reduce large complex data sets into a series of optimized and interpretable views. These views emphasize the natural groupings in the data and show which variables most strongly influence those patterns. PCA finds applications in diverse fields such as: analytical chemistry [13], astronomy [30], and microbiology [78]. As it is still difficult to quantitatively correlate the two analytical methods, a substantial effort is placed on a robust statistical evolution of the data sets. One of the best-suited techniques to solve the collinearity problem is the partial least-squares projection to latent structures (PLS) [20]. The main applications of this technique are calibration of spectra in analytical chemistry and Quantitative-Structure-Activity-Relationship, QSAR. In this way, more robust calibrations can be accomplished as with the conventional way. QSAR builds structure-activity models relating the chemical structure with the catalytic activity.

5.2 Mechanical activation of solids

This chapter describes methods and applications of mechanical activation of solids. The introduction of structural and electronic defects caused by the destruction of long range order is briefly discussed. Thermodynamical considerations of the changes that occur in the solid upon milling were given. This chapter also presents previous results of investigations of the mechanical activation of graphite

5.2.1 Tribochemistry

Mechanical activation like grinding and milling defines a process in which a material is submitted to high pressures in the form of impacts, deformations, and stress. Since ancient times people have known that chemical reactions can be induced by mechanical energy, e.g. by friction or impact. In prehistoric times, people generated light with the aid of flint stones.

The term tribochemistry was given by Oswald in 1911 to denote those chemical reactions affected by mechanical energy [54]. Tamman [72] in the 1920s, Fink in the 1930's [22], and later Bowden and Tabor [9], studied the influence of mechanical treatment on the reactivity of solids. It was not until the 1970s that scientific investigations on the mechanism of the transfer of mechanical energy on solids begun.

Tribochemistry investigates chemical and physical changes due to the impact of mechanical energy on solids. These changes depend not only on the intensity, duration, and experimental conditions of the treatment, but as well on the solid itself. Mechanical activation introduces both structural and electronic defects and, besides, often changes in the surface area [8] causing an increase of the free energy of the solid. The final state of the milled material depends as well on the type of milling set-up used and on the materials used to build these mill set-ups, such as stainless-steel, WC, and agate. The different milling apparatuses used are stirred, vibratory, and planetary ball- and shaker mills. The destruction of the long-order periodicity in a solid results in an increase of its entropy, which can lead to thermodynamically less stable. states (metastable). The increase of the free energy of the system divides itself between the metastable. state and the energy responsible for the increase of the reactivity of the solid. For example, Rühle *et al.* mechanically milled F_2O_3 [57] and give a nice introduction in the effects of mechanical activation and the rise of the free energy of a solid.

5.2.1.1 Applications

- Amorphous alloys

Until recently amorphous metallic alloys were exclusively synthesized by rapid cooling. The material either was cooled below the crystallization temperature from the molten phase with cooling rates between 10^6 and 10^{10} K/s or condensed from the vapor phase onto a cold substrate [11]. These alloys are used for high temperature applications.

Schwarz *et al.* [65] reported for the first time the preparation of an amorphous alloy by a solid state reaction of pure polycrystalline metals. The mechanism of mechanical activation has been described by Benjamin and Volin [6]. In this process a blend of elemental or alloy powders is subjected to highly energetic compressive impact forces in a ball-mill. These impact forces lead to

a repeated cold welding and fracture of powder particles resulting in a lamellar structure of the powder particles. A review on the formation of amorphous alloys by mechanical activation was recently given by Weeber *et al.* [81] .

- Creation of thermodynamically unstable phases

There are two classical examples where the mechanical activation of a solid transforms one phase into another one, which is thermodynamically less stable.

1. $\{\beta\}$ - PbO_2 : stable. at room temperature transforms into the $\{\alpha\}$ - PbO_2 modification upon milling, which is stable. at higher pressures.
2. CaCO_3 : the stable form calcite is transformed into aragonite , which is stable. at higher temperatures.

In both cases, a total transformation into the less stable form is not observed, but an equilibrium of both phases. Milling is equal to a high-pressure and/or a high-temperature treatment.

- Catalysis

The idea of using mechanical activation in heterogeneous catalysis is to create a more reactive catalyst due to an increase of the surface area, dispersion of the active component over a support, and to increase the amount of electronic and geometrical defects. One example is the dispersion of MoO_3 over Al_2O_3 [46]. Mechanical milling of both materials results in the dispersion of the active phase avoiding the use of wet chemical methods. Another example is the mechanical activation of Fe_2O_3 (Hematite) for the H_2 production from H_2O [63]:



and in the SCR of NO with CO [58]:



In the first case hematite was mechanically activated to form magnetite in a H_2 atmosphere and in the second case in air. After the activation the catalyst shows a significant higher conversion due to the introduction of lattice defects and an increase of the surface area, which results in an increase of active sites.

5.2.2 Mechanical activation of graphite

5.2.2.1 Overview

The results concerned with the mechanical activation of graphite will be briefly presented. Bacon

[4] and Boehm *et al.* [7] reported the loss of long-order periodicity upon mechanical activation detected by XRD. After this initial work an increased interest in this field is observed only recently. From the work conducted by Tang *et al.* [73], an amorphization of graphite was observed with HR-TEM upon milling in dry conditions. This amorphization was explained to be caused by the presence of metal impurities like WC, Co or Fe, which stabilize amorphous carbon structures. The presence of such impurities was caused by the milling set up used in the experiments. WC balls were used where Co is added as binder [26]. The characterization of the milled samples using HR-TEM showed the destruction of the graphite lattice upon milling. Hermann *et al.* [29] milled graphite using different devices made from agate, WC, and stainless steel. He explained the different structures obtained for equal milling times as a difference of the density of the materials resulting in a difference of the efficiency of energy transfer to graphite. Welham *et al.* [8] also studied the amorphization upon milling of graphite and active carbon in dry conditions with XRD and found similar results to the above cited works. Niwase *et al.* [52] monitored the amorphization of graphite upon milling in dry conditions using Raman spectroscopy. The author found a decrease of the crystallite size upon prolonged milling.

There are two reports relating the mechanical activation of graphite to the reactivity in the combustion with oxygen [29,8]. In both studies, the reactivity measurements were conducted with high heating rates, 20 K/min [29] and 25 K/min [8], respectively. Both authors found an increase of reactivity upon milling, which could not be correlated to the increase of BET surface area but to a distortion of the atomic short-range order. However, the presence of transition metals, such as Fe, Co, Cr, and W in the samples found with spark source mass spectroscopy would have considerably affected the combustion rate by catalysis driving the reaction into diffusion limiting conditions. Therefore, a comparison of those combustion activities cannot be accomplished.

5.2.2.2 Experimental

The material used in this study was graphite AF-spezial (99.5% purity, Kropfmühl AG, Germany). The mechanical activation was conducted in a Retsch centrifugal ball mill S2. The crucible and the balls (diameter of 10 mm) were made of agate. The ratio sample to ball weight was 1:4 and the filling volume around to 70%. The acceleration employed for all the experiments was 50 kg/ms². Since it is known [69] that the experimental milling conditions play a decisive role on the final milled product, a solvent was added into the milling chamber to study its effect. Two series of samples were obtained, one in the presence of the non-polar solvent hexane, h-series, and one under dry conditions, d-series. Samples were taken after 0, 3, 24, 72, and 168 hours, respectively. Tab. 2 summarizes the set of experiments conducted in the milling chamber.

Tab. 2: Set of experimental conditions used to obtain milled samples and nomenclature used for the samples.

Samples	Nomenclature	
Graphite AF-s	starting	
Milled samples time [hours]	Hexane	Dry
3	h3	d3
24	h24	d24
72	h72	d72
168	h168	d168

6 Characterization of the mechanically activated graphite

6.1 BET surface area and morphology of the mechanically activated graphite

In this chapter, the changes in the surface area and in the bulk morphology upon milling are discussed. It is shown that not only the milling time, but also the experimental milling conditions play a decisive role in the final surface area. TEM and ED images show different structural changes within the two series.

6.1.1 BET surface area

Abb. 7 shows the progression of the surface area with increased milling time. It can be noted that the presence of hexane has a pronounced effect on the surface area of graphite under mechanical activation. The presence of hexane promotes an increase in the BET surface area over the entire treatment time and after 168 hr milling the BET surface area is 8 times larger than in the *starting* material. The absence of hexane resulted in an initial increase of the surface area and a decrease upon extended milling times, due to recombination.

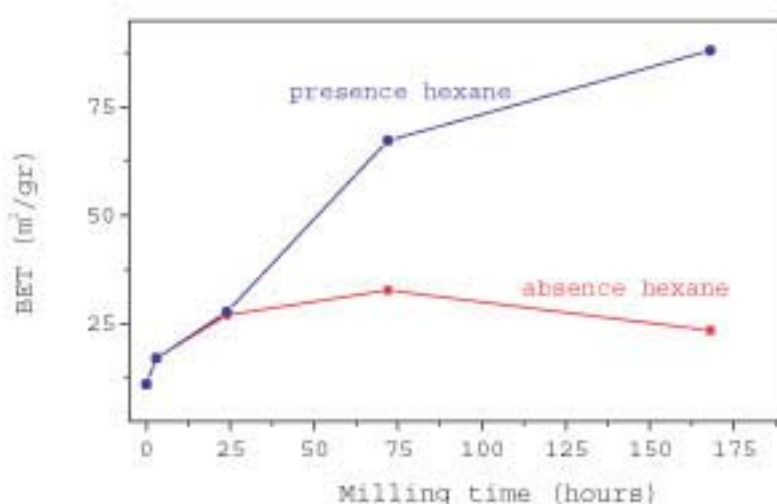


Abb. 7: Effect of the milling time and the experimental conditions in the evolution of the BET surface area.

6.1.2 Morphology

6.1.2.1 Scanning electron microscopy (SEM)

Figure 3.2 shows a typical SEM micrograph of the *starting* material. The sample shows flakes of several μm in size with a polygonal shape. This morphology can be appreciated from the well-defined edges and terraces.

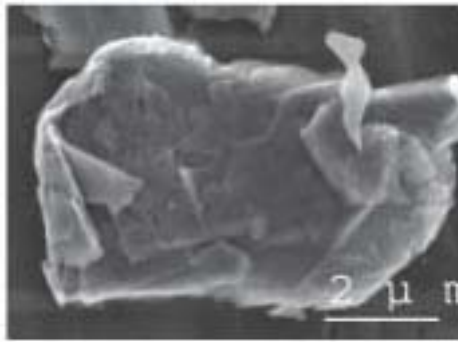


Abb. 8: SEM micrograph of the *starting* material.

Milling in the absence of hexane caused a decrease in the particle size as seen in the SEM micrograph in Figure 3.3, which shows the morphology of the d72 and d168 samples.

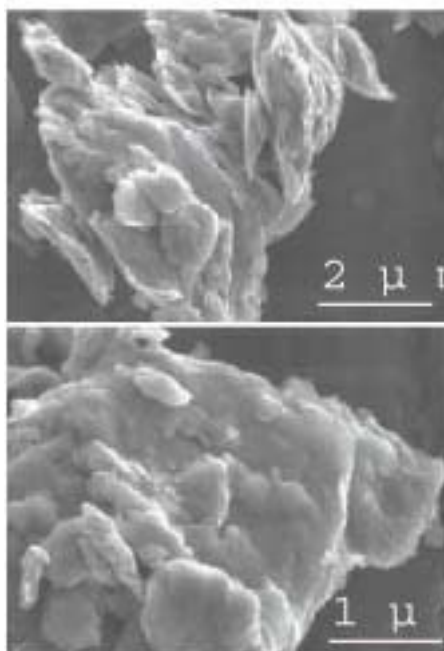


Abb. 9: SEM micrograph of the materials d72 (top) and d168 (bottom).

As the material was mechanically activated, the polygonal flakes transformed into spherical particles. The image indicates a severe destruction of the crystallites and a loss of crystallinity. On the other hand, when the material is milled in the presence of hexane, differences are found in the morphology compared to the *starting* material and the samples from the d series. The sample h168, shown in Figure 3.4, contains a mixture of polygonal flakes and spherical particles. The flakes are, however, no longer compact but show signs of an exfoliation process.

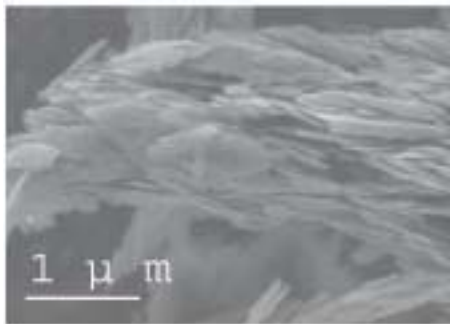


Abb. 10: SEM micrograph of the milled material h168.

It is suggested that the hexane presence might increase the lubrication and thus allows the shearing between the basal planes and prevents the recombination. No signs of intercalation were found by X-ray diffraction (shown in Chapter 4) or indications of impurities by EDX in any sample.

6.1.2.2 High-resolution-TEM

The SEM micrographs showed changes in the morphology of the activated material, especially in the absence of hexane. High-resolution transmission electron microscopy (HRTEM) and electron diffraction (ED) were conducted to study the structure and the defect concentration in both materials after seven days of milling pre-treatment compared to the *starting* material.

The TEM image shown in Abb. 11 corresponds to the *starting* material showing large and thick particles.

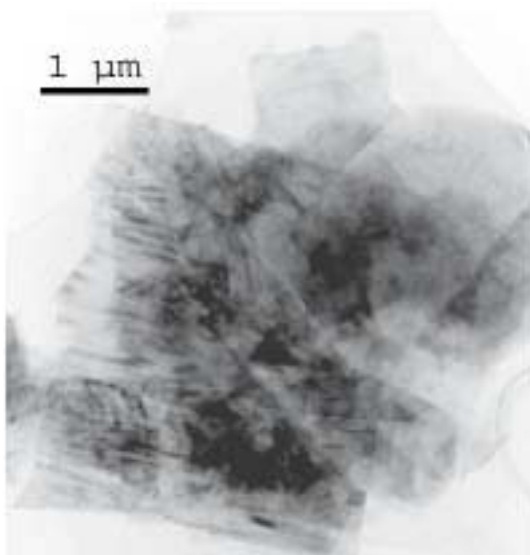


Abb. 11: TEM micrograph of the *starting* material.

The HR-TEM images of the sample d168 show even more pronounced differences to the precursor microstructure as shown in Abb. 12-14. The absence of hexane in the milling chamber causes a higher degree of amorphization. The presence of multiple defects is shown in both images (Abb.

12-13). The graphite sheets are broken and even bent crystallites are present.

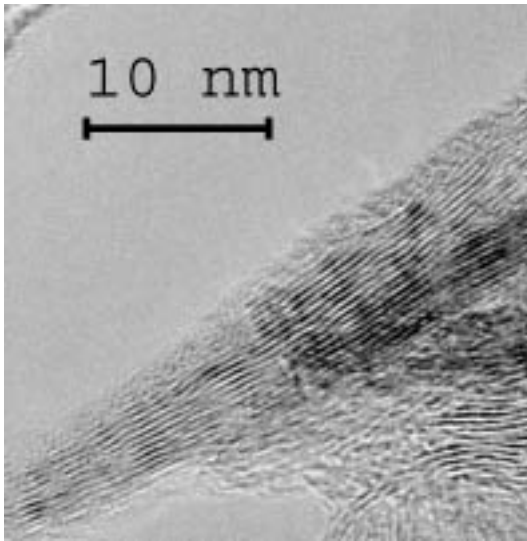


Abb. 12: TEM micrograph of the milled material d168.

These images further show the destruction of the graphite sheets into basic structural units (BSU) of a few nm size. These BSU are stacked to packages separated by defect zones, which might be created by segregating and clustering of individual defects to minimize the extra lattice energy brought into the system by milling.

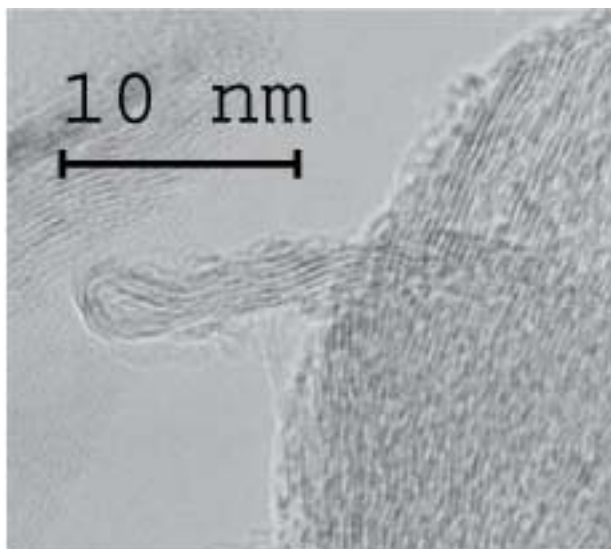


Abb. 13: TEM micrograph of the milled material d168.

The three-dimensional character of the microstructure is largely defined by the inclusion of debris from broken graphene sheets in between the stacks of the BSUs. In Abb. 13 however, it can be seen that milling also caused the creation of non-six membered carbon giving rise to fullerene-like bending of carbon sheets. At the same time, some well-defined graphite crystallites remain, see Abb. 14. This shows that residual very thin graphite flakes coexist with the amorphous domains.

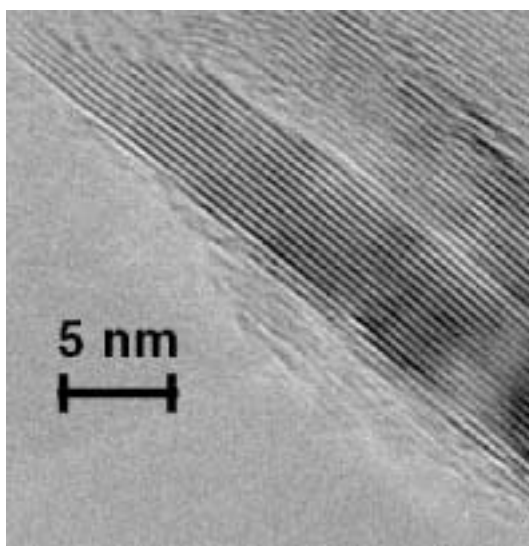


Abb. 14: TEM micrograph of the milled material d168.

The sample h168 shows marked differences as compared to the sample d168, as can be seen from Abb. 15. The particles are much thinner than those of the *starting* material. These observations agree with the observed SEM morphology and the large specific surface area. The d-spacing value was measured to 123 pm along the [110] direction.

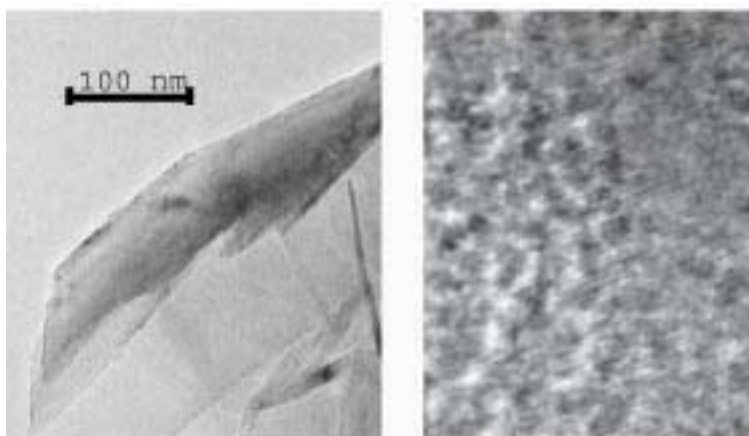


Abb. 15: TEM micrograph of the milled material h168 (left). The right image shows the d-spacing along the [110] direction.

6.1.2.3 Electron diffraction (ED)

The ED pattern of the *starting* material, Abb.16 left, shows the spots of the 100, 200, and 110 reflections, respectively. The presence of spots and rings indicates a fraction of crystallites with a well-ordered in-plane structure to coexist with other fractions with significant turbostratic disorder.



Abb. 16: ED pattern for the starting material (left), d168 (middle), and h168 (right).

The corresponding diffraction pattern of the milled sample in the absence of hexane d168 in Abb.16 (middle) reveals complete amorphization and the loss of texture appears as a 002 diffraction ring. This means that within the overall flaky morphology, there must be present a significant volume fraction of carbon with its stacking direction not being parallel to the average basal plane of the flake. Such situations can be seen in all HR-TEM images of Figures 3.6-8. The ED pattern of the sample h168 is shown in Abb.16 (right). The diffraction pattern in form of spots and rings as compared to the one in Abb.16 (left) reveals the reduction in platelet thickness associated with the reduced turbostratic disorder in each flake. The presence of amorphous carbon in the textured form is evidenced by the rings around the hk reflections and the absence of a 002 ring, which proves that three-dimensional aggregates of distorted carbon (carbon black or "soot") have not been formed.

6.2 Geometric structure of mechanically activated graphite

In this chapter, the changes in the geometric structure upon milling are discussed. Mechanical activation leads to a transformation from crystalline into amorphous carbon. Different structural models are presented to explain asymmetries of several reflections found in the XRD diffractograms during the amorphization process. Raman spectroscopy and XRD were correlated to explain the simultaneous appearance of two Raman forbidden modes as the crystallite size decreases.

6.2.1 X-ray diffraction

6.2.1.1 Results

From the diffraction patterns presented in Abb. 17 of samples d168 and h168, significant changes in the graphite structure are evidenced compared to the *starting* sample. The *starting* graphite is highly crystalline as seen by the small peak width FWHM Γ . Significant changes can be appreciated in the profiles and in the FWHM of the reflections of milled graphite. Three main reflections presented in Abb. 17 have been analyzed: 002_{hex} (B), 100_{hex}; 101_{hex}; 101_{rhom}; 012_{rhom} (C), and 110_{hex} (D). No evidence of crystalline impurities, either in the *starting* material or from the milling media was detected.

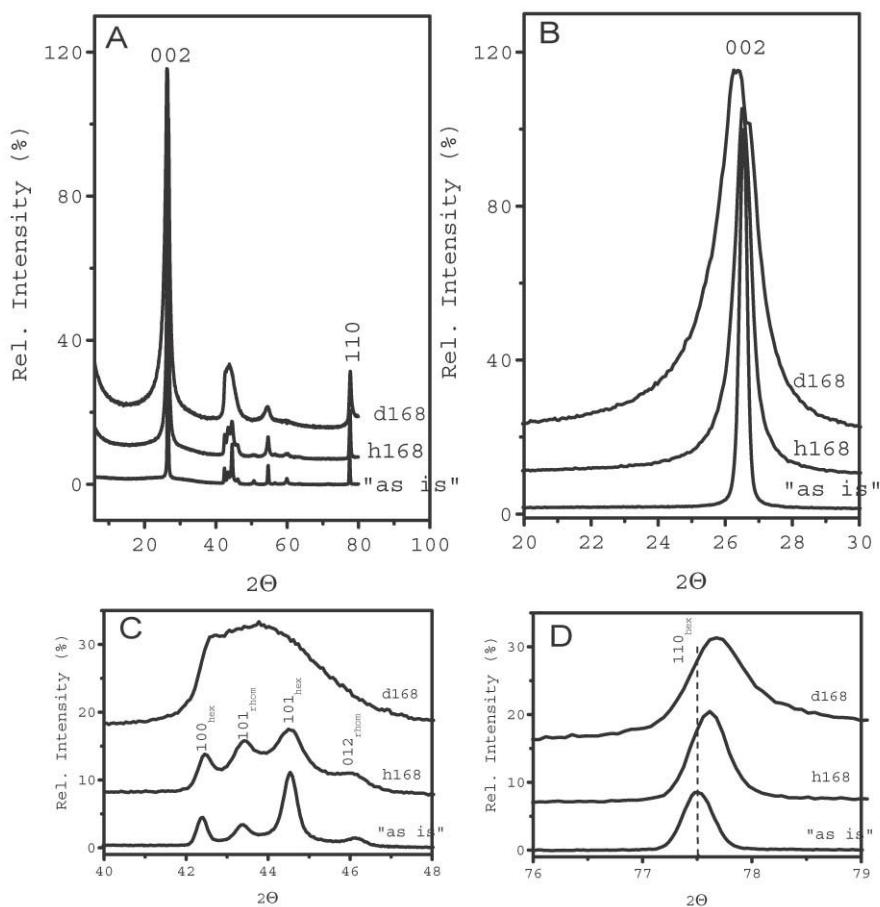


Abb. 17: XRD diffractograms of the milled samples in presence and absence of hexane after 168 hr compared to the *starting* material, showing regions corresponding to the 002 reflections (B), 100-101_{hex}; 101-012_{rhom} (C), and 110 (D) analyzed in this work.

Tab. 3: XRD results of milled graphite samples. Split-Pearson VII fit of the XRD diffractograms, m_L = low angle exponent associated to asymmetry toward higher d-spacing values and m_R = right angle exponent associated to asymmetry toward lower d-spacing values.

Sample	d_{002} [pm]	Γ_{002} [2 θ]	m_L	d_{110} [pm]	Γ_{110} [2 θ]	m_R
<i>starting</i>	335	0.255	1.975	123	0.316	4
h3	335	0.281	1.87	123	0.352	6
h24	335	0.295	1.438	123	0.319	3.61
h72	335	0.411	0.827	123	0.369	2.72
h168	335	0.576	0.723	123	0.386	1.83
d3	335	0.300	1.63	123	0.357	4
d24	335	0.357	1.077	123	0.341	1.86
d72	336	0.778	0.778	122	0.508	0.90
d168	338	1.445	0.618	122	0.635	0.51

The progression of the 002 reflection milled in either hexane (left) or under dry conditions (right) is compared in Abb. 18.

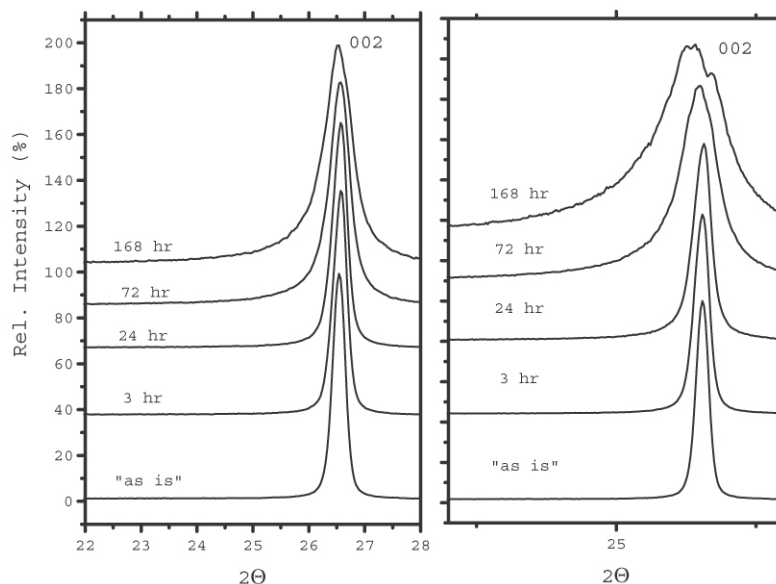


Abb. 18: Progression of the 002 reflection with milling time in the presence (left) and absence (right) of hexane. The absence of hexane in the milling chamber resulted in a drastic increase of the FWHM of this reflection, a shift to higher d-spacing values, and to an asymmetry to higher d-spacing values compared to milling in the presence of hexane.

Milling under hexane results in a progressive broadening and an increasing asymmetry to higher d-spacings. The fit the profile of this reflection was obtained with the asymmetric Split-Pearson VII function. For the samples milled under hexane the 002 reflection shows a slight increase both in the FWHM and in the m_L value, see Tab.3. This latter value is associated with the asymmetry to lower 2θ values for $m_i=1$ a symmetric Voigt function is obtained). The absence of hexane caused more pronounced changes in the 002 reflection compared to the h-series, as shown in Abb. 18 (right). The profiles are exceedingly more broadened and show greater asymmetry with a tailing to larger d-spacing values. In addition, the peak maxima are also shifted up to 338 pm, see Tab.3. Tab. 3 presents the results of the fitting with the Split-Pearson VII function. This asymmetry to higher d_{002} values was also observed for the h-series. The m_L parameter continuously became smaller for the d-series reaching a value of 0.618 after 7 days of milling.

The evolution with milling of the 100-101_{hex} and 101-012_{rhom} reflections presented in Abb. 19 (left) shows differences in the presence of hexane. The symmetric profiles of the reflections permitted their fitting using the Voigt function, and the results of the fitting are presented in Tab.4. All reflections except 012_{rhom} remain at the same d-spacing value. This latter reflection shifts to higher d-spacings for the sample h168. All reflections show an increase of the FWHM upon prolonged milling time.

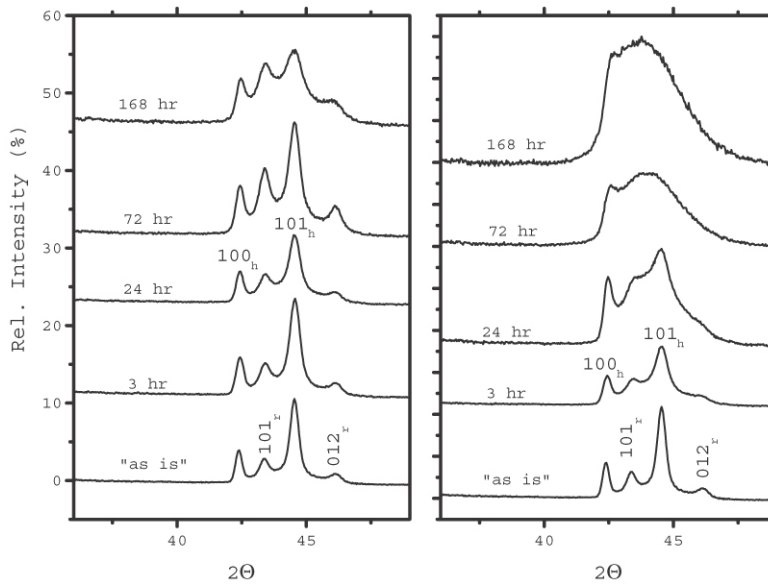


Abb. 19: Evolution with milling time of the 100-101_{hex} and 101-012_{rhom} reflections in the presence (left) and absence of hexane (right).

Tab. 4 also lists the relative areas corresponding to the hexagonal and the rhombohedral form of graphite and their respective FWHM values. The multiplicity of the corresponding planes H_i were included in the calculation to determine the fractions of the respective modifications. The rhombohedral reflections 101 and 012 increase remarkably with prolonged milling time. This structural modification caused by powdering-milling has been known since the fifties [4,7].

Tab. 4: Effect of milling on hexane in the characteristic 100-101_{hex} and 101-012_{rhom} reflections. The fit was performed with the Voigt Function. The amount of phases was calculated using the respective H_i values, for hexagonal phase $H_{100}=6$, $H_{101}=12$, and for the rhombohedral phase $H_{101}=4$, $H_{012}=4$.

Sample	Hexagonal					Rhombohedral				
	d_{100}	d_{101}	Γ_{100}	Γ_{101}	Σ	d_{101}	d_{012}	Γ_{101}	Γ_{012}	Σ
	[pm]	[pm]	[2 θ]	[2 θ]		[pm]	[pm]	[2 θ]	[2 θ]	
<i>starting</i>	213	203	0.30	0.42	6.73	208	196	0.56	0.64	7.46
h3	213	203	0.35	0.50	6.54	208	196	0.61	0.72	7.94
h24	213	203	0.33	0.57	6.23	208	196	0.67	0.78	8.60
h72	213	203	0.36	0.58	5.57	208	196	0.59	0.65	10.35
h168	213	203	0.41	0.97	5.33	208	197	0.85	1.08	10.88

In the case of the dry samples the effect of milling in the 100-101 hexagonal and 101-012 rhombohedral reflections shows a different evolution, as shown in Abb. 20 (right). While the position of the 100 reflection remained constant, its profile became more asymmetric to lower d-spacing values. On the other hand, the 101 reflection shifted to higher d-spacing values and became more symmetric with a nearly Gaussian intensity distribution after 24 hours. The reflections grow such broad, that is impossible to separate and analyze them.

The profile of the 110 reflection shows a slight asymmetry to lower d-spacing values opposite to what was found for the 002 reflection for the samples milled in the presence of hexane, as shown in Abb. 20 (left). This reflection shifted slightly to lower d-spacing values with a gradual broadening, see Tab. 3.

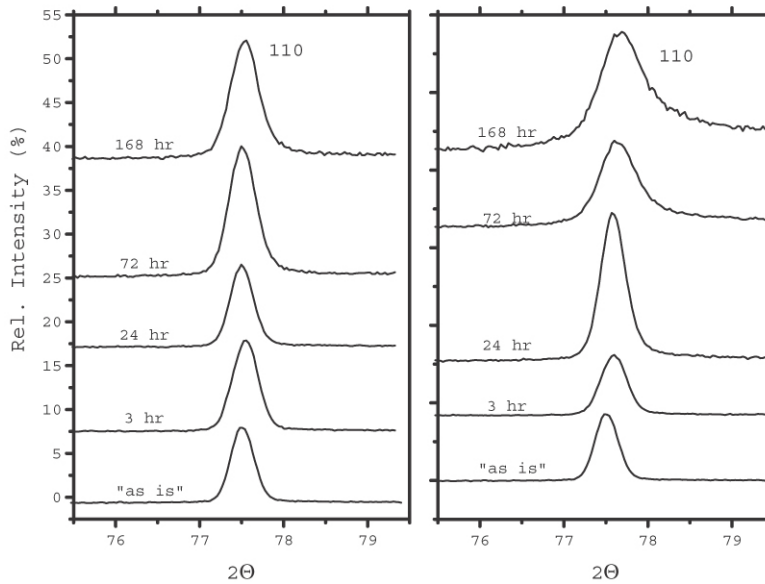


Abb. 20: Evolution with milling time of 110 reflection in the presence (left) and absence (right) of hexane.

The observed asymmetry of the 002 reflection correlates to the enhanced asymmetry detected for the 110 reflection and consequently m_R , which quantifies the asymmetry to lower d-values, as shown in Abb. 20 (right) and Tab 3. Both reflections show a more severe broadening compared to the h-series.

In conclusion, the dry milling conditions were much more severe in the destruction of long-range order as indicated by the broadening and asymmetry of the diffraction profiles. Tab. 3 reveals that the asymmetry in the 002 reflection for the d-series is larger than for the h-series. Milling in dry conditions is more suited for achieving a controlled degree of stacking disorder of graphite. To account for structural changes in the graphene planes the FWHM of 100 and the 110 must be analyzed. The loss of the long-range periodicity along the h00 and 0k0 directions is also more significant under dry milling conditions in parallel to the trend for the stacking order reduction.

6.2.1.2 Analysis of variance (ANOVA) of the effect of milling time and experimental conditions

Since the presence of hexane preserves the crystallinity within the graphene planes and an interaction between the BET and the experimental conditions was found, the following analysis was conducted. The crystallite sizes along the [002] and [110] crystallographic directions were submitted to ANOVA analysis to determine to what extent one of these crystallographic directions was affected upon milling in presence or absence of hexane. The parameters studied were the milling time, the experimental milling conditions, and the interaction between both factors. The samples studied were the *starting* and milled graphite after 72 and 168 hr both in presence and absence of hexane.

ANOVA is an statistical tool used in experimental design and quality engineering [71] to determine effects of parameters and interactions. ANOVA measures the variation between samples and decomposes the variation or sum of squares (SS), in this case the crystallite sizes S_{002} and S_{110} into the variation explained by the parameter milling duration, presence of hexane, the interaction between these two parameters, and the variation due to the experimental error always present when a quantity is measured.

The analysis is presented in the Appendix. Tab. 5 presents the different experiments and the values of the crystallite sizes for the crystallographic planes d_{002} and d_{110} . The experiments were replicated to calculate the variation of the experimental error.

Tab. 5: ANOVA analysis. List of calculated crystallite sizes in Å for the crystallographic [002] and [110] directions calculated from the fitting of the Split-Pearson VII function. Parameter A denotes the duration of the milling ($A_1= 0$, $A_2= 72$, and $A_3= 168$ hr) and parameter B denotes the presence of hexane during the milling ($B_1=no$, $B_2= yes$)

		S ₀₀₂			S ₁₁₀	
		[Å]			[Å]	
Param. A						
Param. B	A ₁	A ₂	A ₃	A ₁	A ₂	A ₃
B ₁	284.7	93.3	50.2	267.3	178.5	142.8
	284.5	80.5	49.8	267.0	171.8	138.5
B ₂	284.7	176.6	123.4	267.3	246.3	233.1
	284.5	176.2	124.0	267.0	233.9	225.6

Tab. 6 shows the complete ANOVA analysis where the SS for each parameters is presented as well as the F-value test. The F-test shown in Appendix B shows that all parameters, milling time and experimental conditions, as well as the interaction between them are significant with a confidence level of 99.9%.

Tab. 6: Complete two-way ANOVA summary showing the SS for the parameters A, B, the interaction $A \times B$, and the experimental error. F test with 99.9% confidence level.

		S_{002}			S_{110}			
Source	SS	ν	V	F	SS	ν	V	F
A	79771	2	39885	2909	15886	2	7943	250
B	7440	1	7440	542	7874	1	7874	248
$A \times B$	6192	2	3096	225	4220	2	21	66
error	82	6	13		190	6	31	
TOTAL	93486	11			28171	11		

The parameter milling time (A) is more important to affect the crystallite size in the [002] direction, highest Variance (V), followed by the experimental conditions, and the interaction between both parameters, respectively. In the [110] direction, both parameters have the same importance, see the V-value, followed by the interaction between them. Abb. 21 clearly shows that both parameters, milling time and experimental conditions, significantly reduce the crystallite size in both directions. In the [002] direction, the absence of hexane has a more significant effect in the reduction of the crystallite size, but after 168 hr the decrease is less strong, and thus the differences for both conditions decrease.

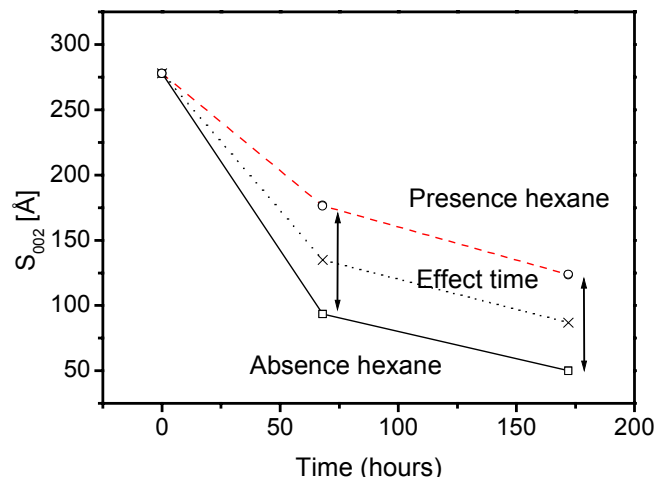


Abb. 21: ANOVA results: plot of effects and interaction between the milling duration and the experimental milling conditions in the [002] crystallographic direction (\times effect of time in the reduction of the crystallite size in the [002] direction, squares experimental values for d series, and circles for h series).

On the other hand, the crystallite size along S_{110} presents another behavior, see Abb. 22.

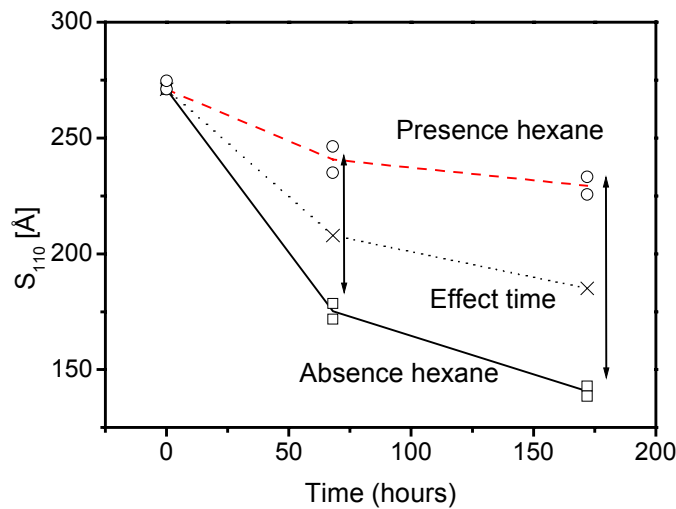


Abb. 22: ANOVA results: plot of effects and interaction between the milling duration and the experimental milling conditions in the [110] crystallographic direction (\times effect of time in the reduction of the crystallite size in the [110] direction, squares experimental values for d series, and circles for h series).

The duration of the milling shows the same effect, i.e. decreasing the crystallite size. But in this case, milling in the absence of hexane causes a more drastic decrease in this direction than in the presence of hexane. The differences between milling treatments increases with time indicating that the milling in absence of hexane continues to destroy the periodicity on the graphene plane. This means that the crystal is preferentially broken in the c-axis direction for both conditions with increasing milling time and the presence of hexane inhibits or retards the destruction on the graphene planes along the [110] direction.

6.2.1.3 Simulations of the asymmetries of the [002] and [110] directions

Several structural models were analyzed to explain the observed asymmetries of the 110 and 002 reflections, respectively. The first case concerns the increase of the d-spacing value in the [002] direction and second case the increase of the rhombohedral phase in the milled graphite samples, see Abb. 23.

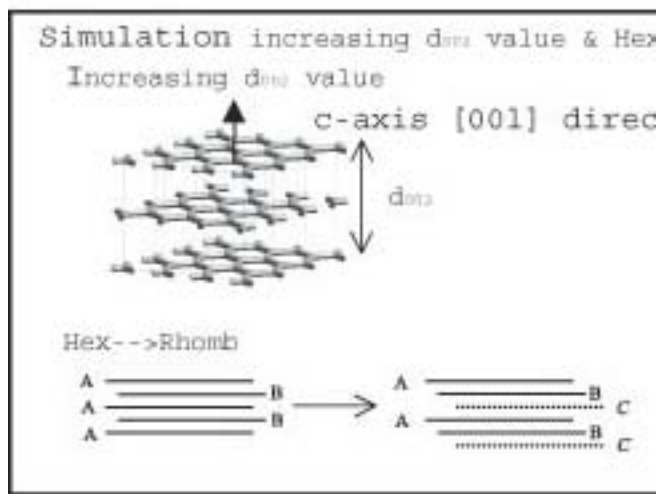


Abb. 23: Simulation of increasing the d-spacing value in the [002] direction (above) and hexagonal ->rhombohedral transformation (bottom).

Abb. 24 shows the calculated diffractograms of several graphite structures with increasing d-spacing values in the c direction from $d_{002} = 3.35$ to 3.38 Å. The increase in the d_{002} value shifts the position of the 002, 101, and 104 reflections to lower 2θ values. On the other hand, the positions of the 100 and 110 reflections remain fixed. Therefore, the existence of graphite domains with different d-spacing values explains the asymmetry of the 002, but not of the 110 reflection.

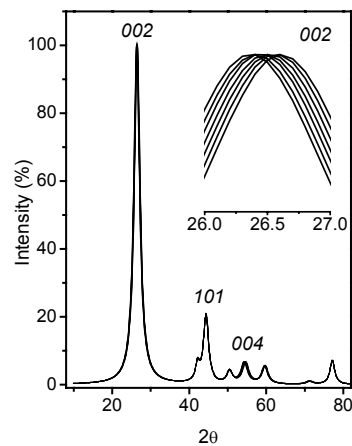


Abb. 24: Theoretical diffractograms simulating an increase of the d-spacing value of the basal planes from $d_{002}=3.35$ to 3.38 Å. Right plot shows the displacement of the 002 reflection upon increasing d-spacing distance.

The transformation upon milling from hexg into rhomb graphite was also simulated to show the increase of the 101 - 012_{rhomb} reflections, see Abb. 25. This transformation also introduces one weak reflection appearing at $2\theta=80.67$ near to the 110 reflection, but it cannot explain the pronounced asymmetry found in the milled samples.

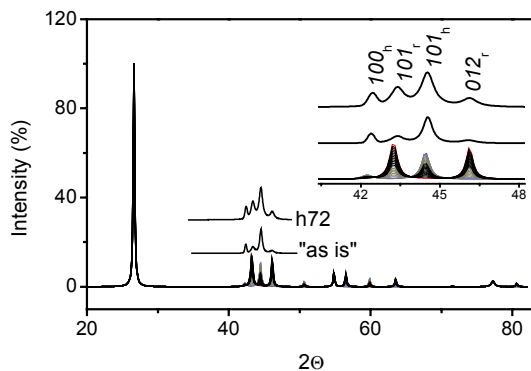


Abb. 25: Calculated diffractograms showing the increase of the amount of the rhombohedral graphite upon milling. The *starting* and milled graphite AF-s after 72 hours in presence of hexane were compared with the theoretical diffractograms (top). Figure bottom shows the increase of the rhombohedral 101 - 012_{rhomb} reflections from 0 to 100% uponmilling.

Two different structural modifications were tested to explain the asymmetry of the 110 reflection: rotation of adjacent basal planes along the c -axis and along the a -axis. The rotation along the c -axis was studied with two models based on a graphite crystal consisting of 5 graphene sheets with dimensions $a=b=100$ Å and $c=75$ Å, see Abb. 26 for more details. The graphite sheets were rotated in one case, Rot z -1 model, in steps of 0.5 degrees for successive layers and in steps of 1 degree

for the Rot z-2 model. The resulting fragment was used as a new unit cell to calculate the resulting diffractograms.

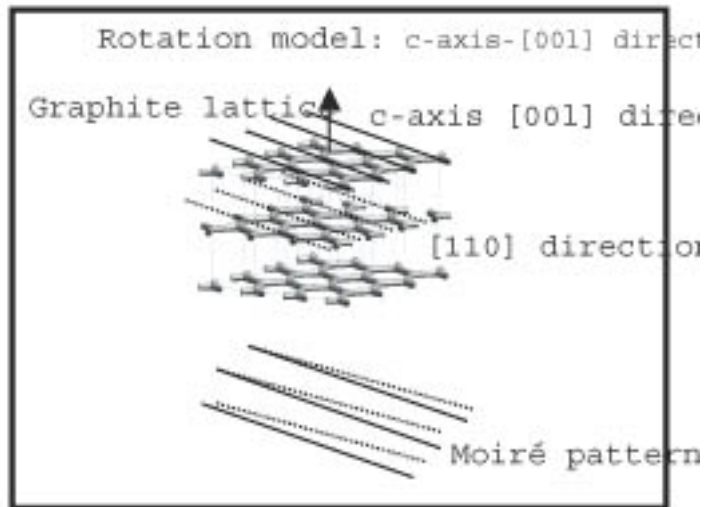


Abb. 26: Structural model: Rotation along the c-axis, [001] direction. Structure of hexagonal graphite showing the characteristic ABABA stacking with the three main 002, 100, 110 directions. The rotation of graphite sheets along the c-axis, [001] direction creates interferences, known as Moiré patterns, causing the asymmetries of the 110 reflection observed with XRD.

Comparing the models in Abb. 27, it is clear that the rotation along the c-axis has several effects on the diffractogram. The most relevant changes occur in the 110 reflection. There is a shift to higher 2θ values like in the observed experimental results. This c-rotation does not shift the 002 reflection to lower 2θ values as expected, since the d-spacing value remains fixed in the model. Whether this c-axis rotation in real crystals decreases the van der Waals interaction between adjacent sheets leading to an increased d-value cannot be confirmed with this calculation.

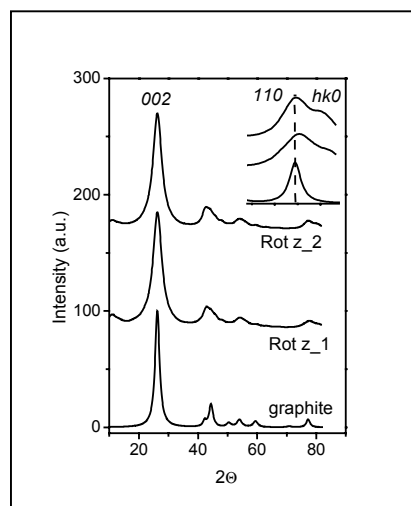


Abb. 27: Calculated diffractograms simulating a rotation of basal planes along the [001] direction (left). Comparison of two rotation models, Rotation {z-1} and 2, showing the appearance of $hk0$ reflections at higher 2θ compared to the expected position 110 (right).

The rotation model along the a-axis which leads to tilted graphene planes and separating the sheets is presented in Abb. 28. Two different rotation models along the a-axis were analyzed. The first model Rot x-1 was constructed as follows: the middle sheet of the same fragment used for the Rot z models was not rotated and the adjacent upper two were rotated with an angle of 0.5 and 1 degrees while the adjacent lower two sheets were rotated with an angle of -0.5 and -1 degrees, respectively. The second model Rot x-2 differs with the first model in the degree of rotation, which in this case was 1 and 2 degrees, respectively.

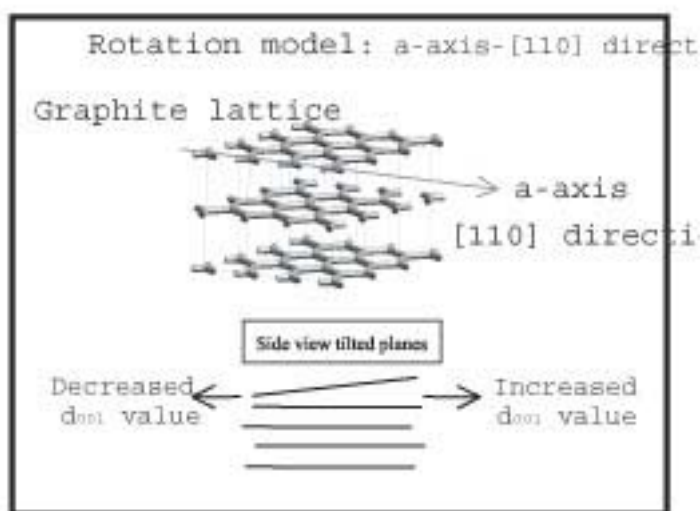


Abb. 28: Structural model: Rotation structural models along the a-axis. Normal and side view of the resulting tilted graphene planes.

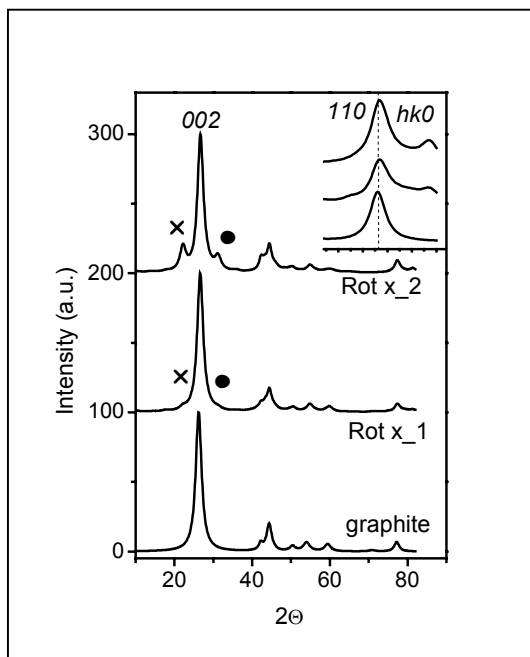


Abb. 29: Calculated diffractogram simulating a rotation of graphene planes along the a-axis (left). Due to the rotation along the a-axis a peak appears at higher d-values, marked by x, and another one at lower d-values, marked by +. This latter peak has no physical meaning. Comparison of two rotation models showing the appearance of 00l and hkl reflexes at higher 2θ compared to the expected positions of the 002 and 110 reflections (right).

Abb. 29 shows the simulation calculated from the model presented above. This results in the appearance of additional 00l reflections at higher d-values, marked as x. The rotation of the sheets separates the sheets, but also brings together the sheets explaining the 00l peak at lower d-values, marked as +, which have, however, no physical meaning, see Abb. 28. At the same time, this rotation resulted in the appearance of hkl reflections at higher 2θ values.

6.2.1.4 Conclusions on the structural models

6.2.1.4.1 002 Asymmetry

The 002 reflection showed an asymmetry to higher d-spacing values upon milling, see Abb. 18 and Tab. 3 where the m_L value of the asymmetric Split-Pearson VII function showed the continuous progression towards more asymmetric profiles. Furthermore, a significant shift upon milling was observed for this reflection, from 335 to 337 pm shown in Tab.3. This asymmetry and the shift to higher d-spacing values can be explained by a turbostratic disorder of the graphene sheets. Simulations show that the presence of different graphite domains with increasing d-spacing values shifts the 00l and crossed hkl reflections to lower 2θ values, see Abb. 24. The reason for this asymmetry is the presence of domains with higher d-spacing values, which can be explained by a partial rotation of adjacent graphene planes along the c-axis, [00l], and/or a-axis. The van der Waals forces between graphene planes are weak and facilitate the translation and rotation between them.

The rotation by a small degree along the c-axis is presented in Abb. 26 and, in principle, does not separate the basal planes since there is no shift of the 00l reflections, shown in Abb. 27. The calculation indeed did not show any changes of the 00l reflection, but as the adjacent graphene sheets are rotated from their positions, a weakening of the bonding between adjacent sheets could occur, resulting in an increase of the d-spacing between them. Another possibility of rotation is along the a-axis presented in Abb. 28. In this case, the basal planes are tilted resulting in an increase of the d_{002} spacing value as can be appreciated in the calculation of the resulting diffractogram, shown in Abb. 29. However, this latter rotation maybe less likely since more energy will be needed.

6.2.1.4.2 110 Asymmetry

With increasing milling time the 100 and 110 reflections showed both a loss in the long range periodicity (Tab.3) and an asymmetry, shown in Abb. 19 and 20 but in contrast to the 002 reflection, to lower d-values. The overlap of the hexagonal 100 with the rhombohedral 101 reflection renders its analysis difficult. Therefore, only the 101 reflection was studied. This reflection also shifted upon milling from 1.23 Å, in the *starting* material, to 1.22 Å after 168 hr of milling. The value given in the literature for the 110 distance is 1.23 Å [39]. The rotation models discussed provide an explanation for the observed shift and asymmetry. In Abb. 26, the crystal structure of hexagonal graphite is shown, where the crystallographic planes $hk0$ are shown as lines for clarification. The rotation of adjacent graphene planes along the c-axis merges the [100] and [110] directions which may interfere resulting in a constructive interference occurring at lower d-spacing values, see Abb. 26. This type of interference is called Moiré patterns [78].

Furthermore, the two c-axis rotation models revealed the appearance of higher $hk0$ reflections at higher 2θ values resulting in the observed asymmetry, see Abb. 27. At the same time, the rotation along the a-axis also explains the observed asymmetry. The tilted graphene sheets also caused the appearance of higher $hk0$ reflexes leading to the shift and asymmetry of the 110 reflection observed in the experimental data, see Abb. 29 where the combined tilted-rotation models are presented together with the sample d-168 for comparison. Therefore, the rotation of graphene planes, along [00l] and a rotation along the a-axis leading to adjacent tilted graphene planes, results in the observed asymmetry found in the more distorted samples.

Not only rotations but also translations along the a-axis occur upon milling. Milling in the presence of hexane caused a smaller loss of long order compared to milling in the absence of hexane, see Tab. 3. The 002 reflection did not shift and was less asymmetric. Further, the 110 reflections are also narrower and less affected in position or asymmetry. The preservation of the crystallinity of these samples facilitates the transformation from hexagonal into rhombohedral graphite upon milling. The amount of the rhombohedral phase clearly increased upon milling. Milling causes the gliding of graphene sheets due to the weak forces between them. These translations change the stacking order from hexagonal *ABABA* to rhombohedral *ABCABC*. This effect occurs both in presence and in absence of hexane. The difference between the two treatments is the fact, that the presence of hexane protects the crystallinity in the graphene sheets. This transformation has no effect onto the 002 or 110 asymmetries.

6.2.2 Raman spectroscopy

6.2.2.1 Introduction

Raman spectroscopy has been used for the characterization of all kind of carbon materials [15,16,17,18,49,52,76]. In the late sixties, Tuinstra *et al.* [76] were the first to characterize the first-

order Raman spectra of different carbons, e.g. highly crystalline graphite, polycrystalline graphite, and glassy carbons. One sharp mode at 1575 cm^{-1} was found to be specific for crystalline graphite. HOPG, pristine graphite, belongs to the D6h symmetry and possesses the following vibrational modes [17,76]:

$$\Gamma = 2A_{2u} + 2B_{2g} + E_{1u} + 2E_{2g} \text{ (eq.9).}$$

The main stretching modes of the graphite lattice are represented in Abb. 30.

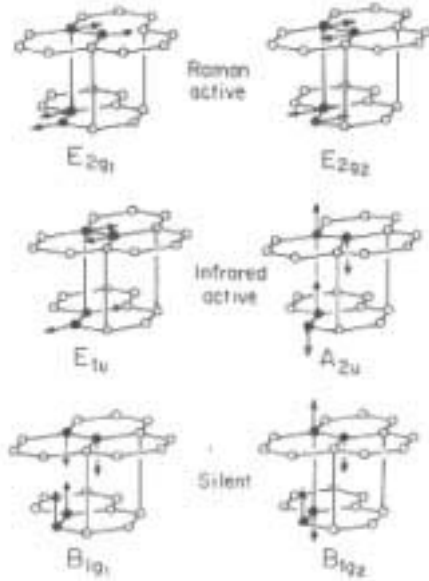


Abb. 30: The graphite stretching modes: Raman and Infrared active vibrational modes [17].

The A_{2u} and E_{1u} modes are IR, and the E_{2g} modes are Raman active appearing at 42 and 1580 cm^{-1} , respectively. The first Raman active mode 42 cm^{-1} is very difficult to measure and only one Raman mode is observed, the E_{2g} mode at 1580 cm^{-1} , called G. The position of this mode is known to vary from $1565\text{--}1580\text{ cm}^{-1}$ [15,17,18,19,21,23,35,60,76]. The frequency variation of this mode was attributed to a laser-induced overheating which was corroborated by studies of the temperature dependence of the graphite Raman spectrum [19,21,23]. A downshift of the characteristic G band of graphite was observed with increasing temperature.

The reduction of the graphite crystallite size and the introduction of defects cause the appearance of new features in both, the first and second order Raman spectrum of graphite [15,17,18,35,60,76]. These new features appear at $\sim 1330\text{--}1360$ and 1620 cm^{-1} in the first-order spectrum. Tuinstra located the first mode at 1355 cm^{-1} and called it D, for disordered carbon samples. The authors [76] interpreted this new mode as a particle-size effect due to the reduction of the graphite crystallite size and proposed an empirical relationship between the ratio intensity of these bands to determine the crystallite size:

$$L_a = k \frac{I_G}{I_D}, \text{ (eq.10)}$$

where L_a is the crystallite size, k a constant and I_G and I_D are the intensities of the 1575 and 1335 cm^{-1} bands, respectively. The broad frequency interval in which the D band was reported [15,17,18,19,21,23,35,45,60,76,8] mainly depends on the laser excitation and the type of carbon samples used. A linear relationship between the position of the D band and the excitation wavelength was found for graphite [33,80]. The phonon dispersion relation of graphite [1,42] has been calculated in the past, and the most widely accepted calculation is the one reported by Al-Jishi *et al.*¹. From the phonon dispersion curves, the origin of the two main disorder-induced modes has been explained in terms of maxima in the density of states. The disorder-induced D line was associated with a large density of phonon states [12,49] and the linewidth of this disordered-induced band was found to be highly sensitive to disorder in the graphite lattice [12]. A second contribution [12,49] appears near 1620 cm^{-1} , called D', reflecting the high density of phonon states for mid-zone phonons. However, there is still a debate whether these two bands arise simultaneously or represent different carbon species. In disordered systems, the crystallite size may become comparable to phonon coherence length which leads to a relaxation of the k-selection rule which restricts Raman scattering to zone-center modes [12,16,17]. For disordered systems, contributions from phonon branches at higher k-values may occur especially for maxima in their density of states, such as for the D mode for zone-edge phonons.

Niwase *et al.* [52,53] studied the changes in the Raman spectra after progressive milling and damages induced by ion-bombardment. A correlation was found between the upshift of the G band at 1580 cm^{-1} with the degree of amorphization. This result is in contradiction with those reported by Cuesta *et al.* [15], where this correlation was not so clear for graphite-like materials. Niwase *et al.* [52] also reported an increase of the intensity ratios I_D/I_G and $I_{D'}/I_G$, which was attributed to a decrease of the crystallite size and the introduction of lattice distortions.

A systematic study was conducted to elucidate the assignment of the two disorder bands to a clearly defined carbon species. Progressive amorphization occurred upon milling, especially when the material was activated under dry conditions. XRD measurements showed a significant decrease of the crystallite sizes along the [00l], [h00], and [hk0] directions. This was in agreement with HR-TEM images of the milled substances which showed distorted graphite crystallites. Raman measurements were also conducted to follow the progressive amorphization and to correlate XRD structural parameters with Raman spectral features. As it is still difficult to correlate quantitatively the two analytical methods, a substantial effort is placed on a robust statistical evaluation of the data sets. One of the best suited techniques to solve the collinearity problem is the partial least-squares projection to latent structures (PLS) [20,31]. The main applications of this technique are calibrations of spectra in analytical chemistry and the evaluation of Quantitative-Structure-Activity-Relationship, QSAR. The first uses the whole recorded spectrum to calibrate the response for different concentrations. A QSAR model relates the structure descriptor, X , with the activity descriptor Y .

6.2.2.2 Results

The Raman characterization was conducted in the wavenumber interval from 950 to 2000 cm^{-1} . Representative Raman spectra of the milled material for both series are plotted in Abb. 31 and the evolution of the intensity I_D/I_G and $I_{D'}/I_G$ ratio upon milling is presented in Tab. 7.

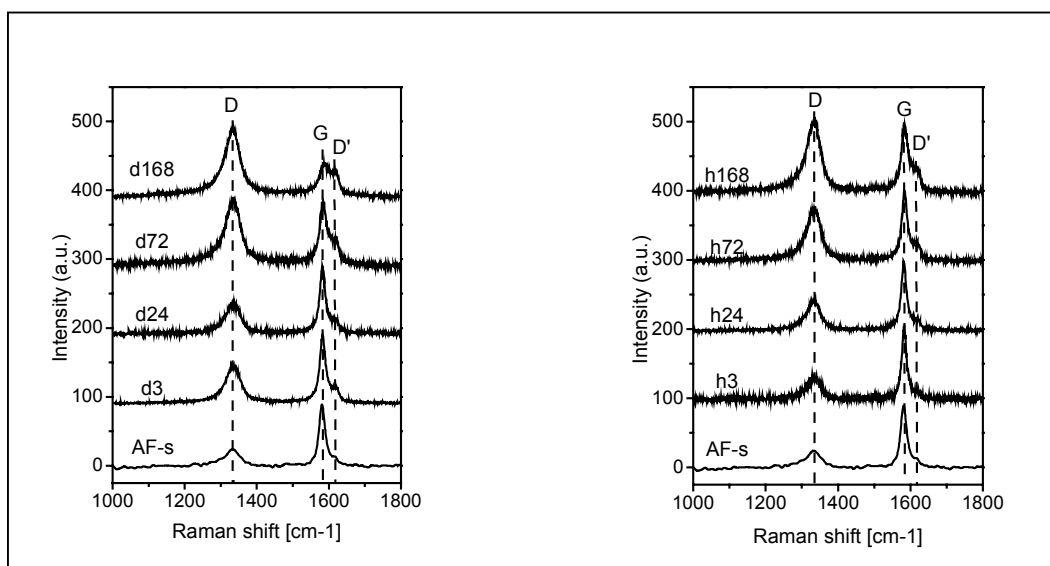


Abb. 31: Evolution of the Raman spectra for the samples milled in the absence (left) and in the presence (right) of hexane. The stretching modes correspond to the first phonon mode for graphite appearing at 1333, 1580, and 1618 cm^{-1} , respectively.

There is a shift of the G band to higher wavenumbers. At the same time the ratios I_D/I_G and $I_{D'}/I_G$ increase their values and the bands D and G are broadened. The position of the band D remains fixed and is located around 1333 cm^{-1} . The changes accomplished with milling in air are more prominent than those under hexane. The shift of the G band is more significant as well as the decrease of the intensity of the G stretching mode. In agreement with the XRD results, there is a correlation between duration and the experimental conditions of the milling experiments and the destruction of the long-range ordering. Thus Raman spectroscopy confirms the reduction of crystallite size upon milling in agreement with previous reports in the literature [52].

Tab. 7: Evolution of the intensity ratios I_D/I_G and $I_{D'}/I_G$ and the position of the G band upon milling.

Sample	I_D/I_G	$I_{D'}/I_G$
starting	0.35	0.11
h3	0.38	0.10
h24	0.42	0.11
h72	0.65	0.16
h168	1.10	0.25
d3	0.44	0.13
d24	0.46	0.16
d72	1.25	0.36
d168	2.11	0.42

6.2.2.3 Effect of laser power

The Raman spectra shown before Abb. 31 were recorded with 0.14 mW power laser. This has the disadvantage of low signal to noise ratios, but using low power lasers avoids the overheating of the sample. The effect of the laser power depends on the graphite studied. Two examples will be presented here.

- Crystalline samples

The first-order Raman spectra of crystalline graphite samples graphite RFL and AF-s were measured with 14 mW laser power. Abb. 32 shows the main stretching modes in the first-order Raman spectra of these samples. The main stretching mode E_{2g} vibrational mode appears at 1581 cm^{-1} .

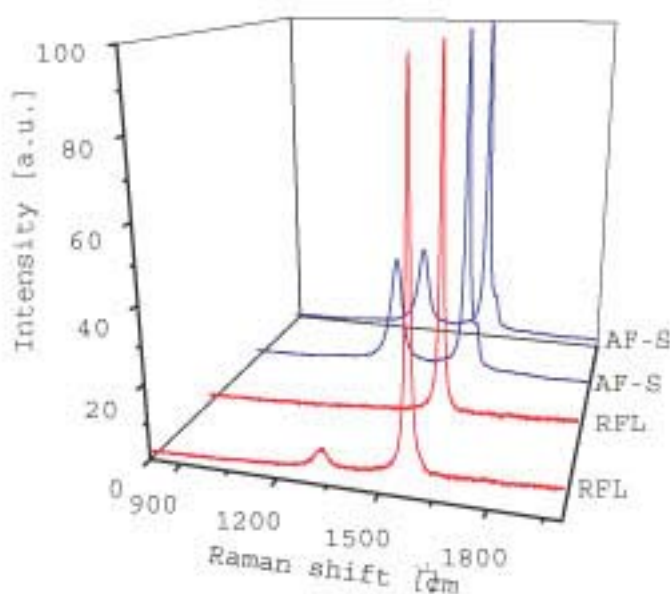


Abb. 32: First-order Raman spectra of RFL and AF-s graphite measured with 14 mW laser power. These two samples studied are representative for crystalline carbon; note the low intensities of the 1333 cm^{-1} and 1620 cm^{-1} bands.

Graphite RFL is more crystalline than the AF-s, evidenced by the appearance of the G band only in some parts of the material. Also the I_D/I_G and I_{D+G}/I_G ratios are smaller for RFL. In Abb. 33, the main E_{2g} stretching mode is plotted and a downshift to 1576 cm^{-1} can be observed. This downshift has been already reported in the literature and it is assigned to overheating of the sample.

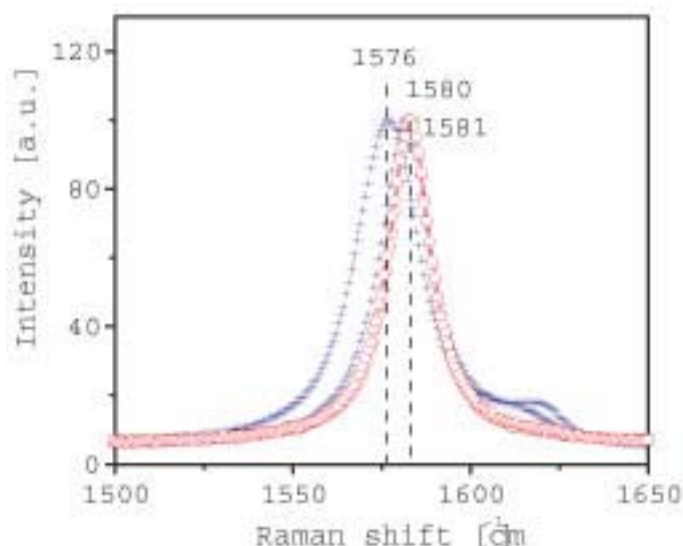


Abb. 33: Dependence of the structure of the studied sample with the effect of the laser power on the position of the E_{2g} vibrational mode. Graphite RFL °, larger flakes, showed almost no effect, whereas AF-s (+), smaller flakes, showed a downshift from 1581 to 1576 cm^{-1} .

No temporal evolution of the spectra under excessive laser exposure could be found. The appearance of the E_{2g} mode between 1581 and 1576 cm^{-1} indicates that some parts of the graphite flakes are influenced by the laser power and others not. Furthermore, the more crystalline the sample the less it is then influenced by the laser power. This might indicate that large graphene planes are more efficient in dissipating the heat, whereas smaller particles cannot, therefore showing the downshift of the G band.

- Milled graphite samples

The sample d72 was submitted to Raman measurements with two different laser powers: 0.14 and 14 mW. The different Raman spectra are presented in Abb. 34, where group A was recorded with 0.14 mW, and group B-C, recorded with 14 mW laser power, respectively.

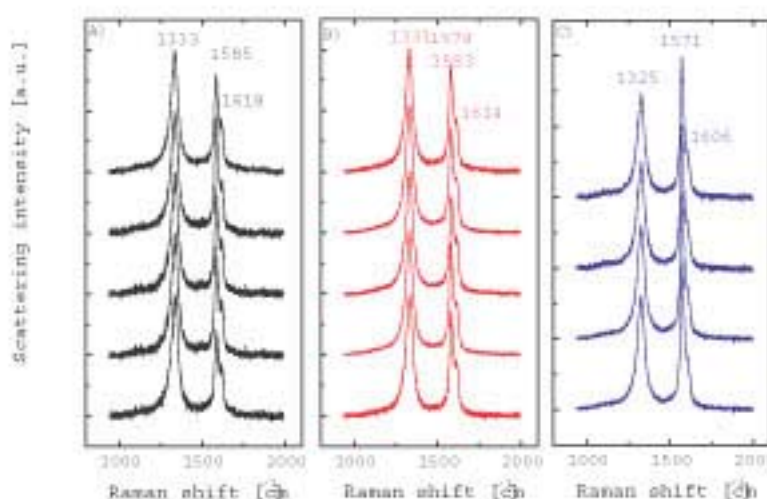


Abb. 34: Representative spectra taken for the sample d72 with two different laser powers: (A) 0.14 mW, (B-C) 14 mW. The evolution of the spectra recorded with 14 mW led to the transformation of spectra of group B into C.

The temporal evolution of the spectra recorded with 0.14 mW did not show any significant changes, see Abb. 34, but the temporal evolution of the spectra recorded with 14 mW exhibited two classes. The first phase is represented by group B and with a prolonged laser exposure the spectra were transformed into C, as shown in Abb. 34. It can be noticed that the spectra recorded with 14 mW exhibit some differences to the spectra recorded with 0.14 mW. Thus, the main stretching modes of graphite shift to lower frequencies: especially for the G and D' bands. The changes induced by prolonged laser exposure appear not only in the frequency shift but a dramatic change in band intensity. A significant decrease of the I_D/I_G and I_D/I_G ratios was observed upon prolonged measurements with 14 mW laser power. Abb. 35 shows the relationship between the I_D/I_G , I_D/I_D , and I_D/I_G ratios in percentage for all measured samples.

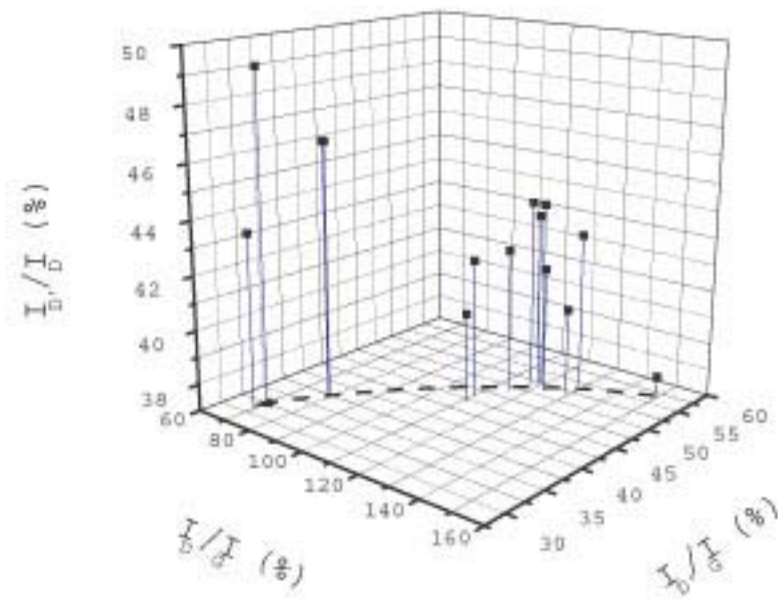


Abb. 35: 3D-Plot of the relationship between the band ratios I_D/I_G , I_D/I_D , and I_D/I_G for the sample d72 measured at different laser powers 0.14 and 14 mW.

This 3D plot shows a positive correlation between the I_D/I_G and I_D/I_G ratios. Simultaneously these two ratios may be positively correlated with the I_D/I_D ratio. This 3D-plot shows the maximum information assimilated with 3 variables. As soon as the number of variables increases, the finding of association patterns between samples and variables becomes more tricky and complicated. To facilitate the analysis of multivariate data, principal component analysis (PCA) was considered as one possible solution. The PCA methodology is explained in the Appendix with an illustrative analysis.

6.2.2.3.1 PCA applied to the classification and study of the laser power effect

PCA was conducted with the spectra of the d72 sample using both laser powers in order to identify whether the two sets of spectra are similar to each other: i.e. 0.14 and 14 mW belong to the same class. The second purpose is to identify correlated spectral features, which classify the spectra. Abb. 36 shows the score plot of the two first components t_1 and t_2 of this group of Raman spectra.

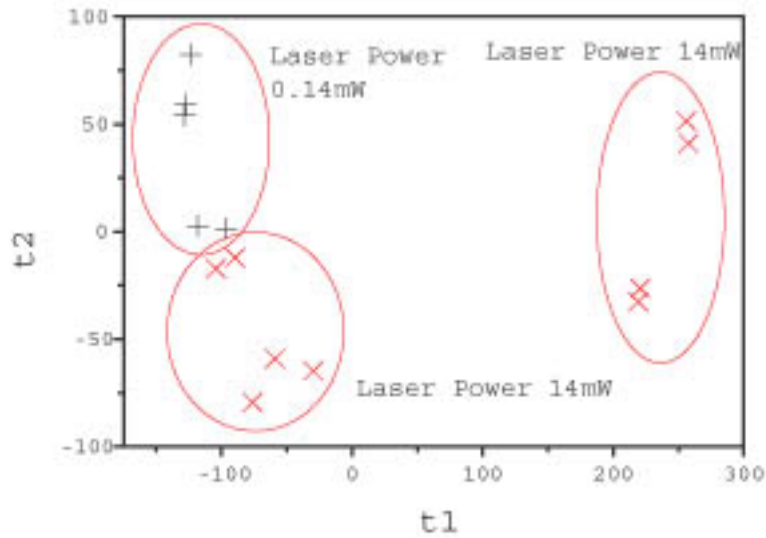


Abb. 36: Plot of scores, t , corresponding to the first and second PC for the \mathbf{X} matrix descriptor corresponding to the problem of the laser power [0.14-14 mW].

Self evidently, the samples are separated into two main groups along the horizontal axis, t_1 . The spectra recorded with 0.14 mW, marked by +, and some spectra recorded with 14 mW, marked by x, are located at the left side of the score plot. Some spectra obtained with 14 mW, marked by x, are located at its right side. There is also another separation, evident along the vertical axis, t_2 . The spectra recorded with 0.14 mW have positive t_2 values, while the spectra recorded with 14 mW have negative t_2 values. The mean spectrum of all recorded spectra is presented in Abb. 37 (A).

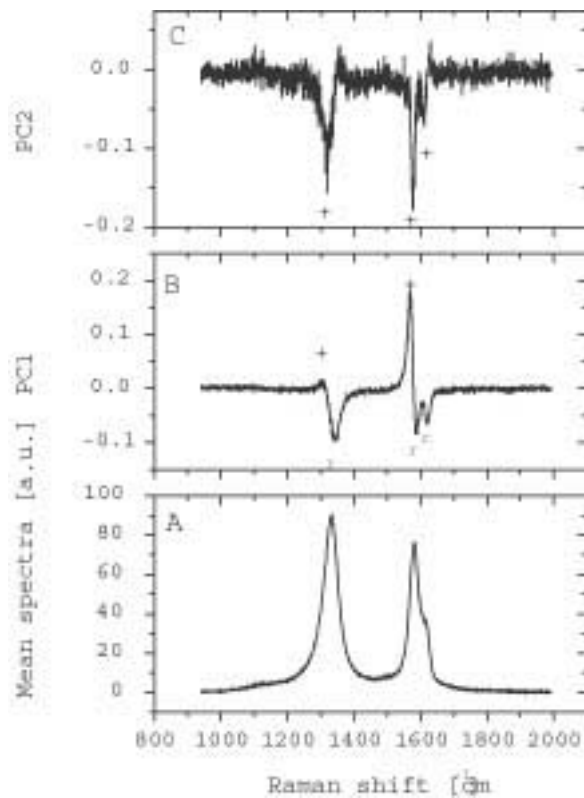


Abb. 37: (A) Mean 1st-order Raman spectra of the sample d72 measured with 0.14 and 14 mW laser power. (B-C) Loading plot, p, corresponding to the 1st and 2nd PC. The spectral region marked by \times and + represent two negatively correlated graphite species.

The stretching modes appear at 1331, 1581, and 1616 cm^{-1} , respectively. To understand the spectral differences, the loading plots of the two first principal components (PC1 and PC2) must be taken into consideration, which are also shown in Abb. 37. The PC1, shown in Abb. 37 (B), indicates a positive correlation between two regions of the spectrum, other regions are negatively correlated, while at the extremes of the Raman spectrum a no correlation exists. The spectral features of the PC1 appearing at 1338, 1586, and 1620 cm^{-1} , marked by (\times), are positively correlated. If one of these spectral features decrease in importance, the rest follows the same pattern and vice versa. Simultaneously, other spectral features appearing at 1308 and 1567 cm^{-1} , marked by (+), are positively correlated. These (+) spectral features are negatively correlated with the (\times) spectral features. It is important to note, that the PC's are no physically real bands. The PC's group the most important variables, in this case intensities of the Raman spectra, into a new variable, i.e. a PC. Their physical interpretation is the presence of at least of two different spectral species that are included in the experimental Raman spectra. The samples located at the right side of the scores plot, Abb. 36, are associated with the spectral species marked by (\times). The samples on the left side of the scores plot are associated with the spectral species marked by (+). Abb. 36 also reveals a differentiation of the spectral species with respect to the PC2 (vertical axis). The PC2 shows three main spectral regions, marked by (+), which all are positively correlated, as shown in Abb. 37 (C). PC2 is mainly associated with the samples recorded with 14 mW. The positively correlated spectral regions appear at 1318, 1576, and 1613 cm^{-1} , respectively. These two PCs explain about 90% of the variance of the data matrix (Tab 8) and are responsible for two different groups of bands: those originally arising from the sample measured at the lowest laser power with bands at 1333, 1584, and 1616 cm^{-1} and secondly those which are affected by the laser power and shifted to lower wavenumbers 1308-1318, 1567-1576, and 1608 cm^{-1} .

Tab. 8: PCA results corresponding to the classification of Raman spectra. Laser power effect (0.14 and 14 mW) in the Raman spectrum for sample d72.

No. of principal component	Eigenvalue 1×10^{-4}	Variance explained (%)	Total variance explained (%)
PC1	1.32	78.02	78.02
PC2	0.21	12.82	90.84
PC3	0.10	5.94	96.79

The shape and intensities of the second group of bands have drastically changed. The ratios I_D/I_G and I_D/I_G of this second group of bands corresponding to this laser group are lower than the intensities of the first group of bands. The exact value of these ratios, however, cannot be obtained because the physical real band shape is unknown. Nevertheless, PCA is able to separate and classify the spectral data and reveal the existence of correlated spectral features, which are content in the observed Raman spectra.

6.2.2.3.2 Conclusions on the laser power effect

The results of the analysis conducted with different graphite samples are summarized in the scheme given in Abb. 38. The observed downshifts depend on the incidence spot of the laser on the graphite crystal. If the laser incides on top of large basal planes, no effect or a very slight downshift will be observed. However, if the spot is located in the near of a domain border or prism the downshift will be expected. Furthermore, the increase of temperature due to the laser power

will burn-off amorphous structures present in the sample resulting in the damage of the sample.

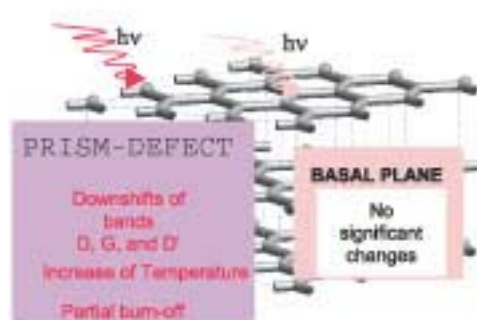


Abb. 38: Effect of the laser power and graphite structure on the first-order Raman spectrum of graphite.

6.2.2.4 Correlation of Raman spectra with XRD patterns

The Raman spectra for the series milled in absence of hexane, presented in Abb. 39, shows a decrease of absolute intensity with milling time. Upon increased milling, the band located at 1580 cm^{-1} decreases in intensity resulting in an increase of the I_D/I_G and $I_{D'}/I_G$ ratios.

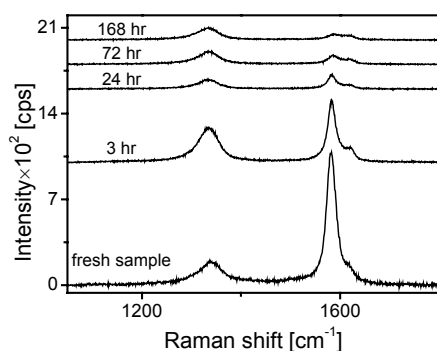


Abb. 39: Dependence of the Raman intensity for the mechanically activated graphite samples under dry conditions on the milling time.

Abb. 40 and 41 show that the observed decrease of XRD coherence lengths of the [002] and [110] directions are positively correlated with the increase of the I_D/I_G ratio. Because a direct correlation was found between Raman spectral features and XRD coherence lengths, a mathematical method partial least squares regression (PLS) was used to fully describe the correlation of the Raman spectra and the XRD diffractograms.

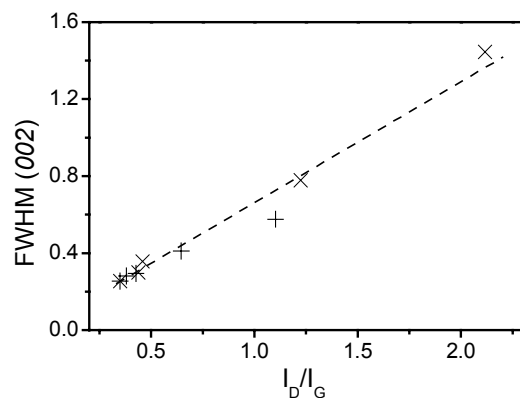


Abb. 40: Direct correlation between decrease of XRD coherence lengths in the [002] direction and the increase of the I_D/I_G intensity ratio.

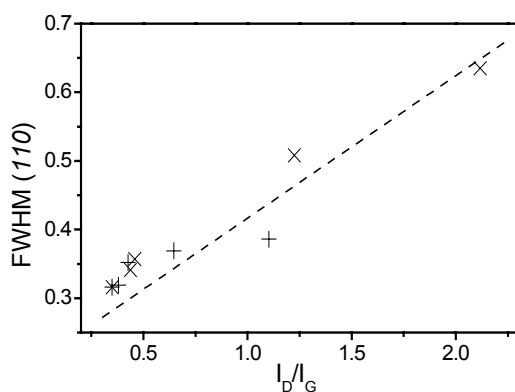


Abb. 41: Direct correlation between decrease of XRD coherence lengths in the [110] direction and the increase of the I_D/I_G intensity ratio.

6.2.2.5 Partial least squares (PLS) model

The whole range of the Raman spectra and of the diffractograms is included in the model. The collinearity of the data makes the use of multiple linear regression impossible [10,20,36]. Therefore, another mathematical approach must be applied to model these two data sets. The best-suited mathematical approach is PLS, see appendix part B.05 for the mathematics behind this method. PLS is an extension of multiple linear regression, but with the advantage that correlated variables can be used.

The results obtained from projection methods like PLS depend on the scaling of the data [20,31]. Using an appropriate scaling of the data, one can focus the model on more important Y- variables, and one can use experience and fundamental knowledge to increase the weights of those X-variables, which contain more information than the others. The X (XRD) and Y (Raman) descriptors were mean centred (see appendix). Several models were calculated depending on the scaling

used prior to PLS analysis: a) no scaling, b) division by 10, c) square root, d) cubic root, and e) logarithm of the **X** and **Y** matrices. The variance determined for the **X** and **Y** descriptor for each model are shown in Tab 9. Without scaling already up to 90% of the variance of the **X** and **Y** descriptor are captured, respectively. Therefore, this model was chosen to study the correlation between both descriptors.

Tab. 9: Percentage of variance captured for the **X** and **Y** descriptors for several scalings before PLS analysis.

Scaling	Σ Variance X			Σ Variance Y		
	PC1 _X	PC2 _X	PC3 _X	PC1 _Y	PC2 _Y	PC3 _Y
No scaling	83.7	90.5	92.7	70.7	91.0	93.0
Divide 10	80.1	86.5	87.4	69.4	89.1	91.3
Square root	74.5	83.4	85.7	68.5	88.1	92.7
Cubic root	75.1	79.6	82.3	67.8	86.8	92.9
Logarithm	66.3	70.3	73.7	66.5	84.9	93.18
No scaling						
XRD [002]	83.7	90.5	92.6	72.9	92.3	94.0
XRD [110]	83.6	90.5	92.9	72.8	91.2	93.0

Abb. 42 shows the first principal components, p1 and q1, for the **X** (left) and **Y** descriptors (right). Two distinct Raman features marked by × in Abb. 42 (left) appear at 1333 and 1620 cm⁻¹. These features are positively correlated and both are negatively correlated with the spectral feature at 1580 cm⁻¹. Hence, when the band at 1333 cm⁻¹ increases in intensity, the band at 1620 cm⁻¹ increases too, whereas the band at 1580 cm⁻¹, marked by + decreases (Abb. 42 left).

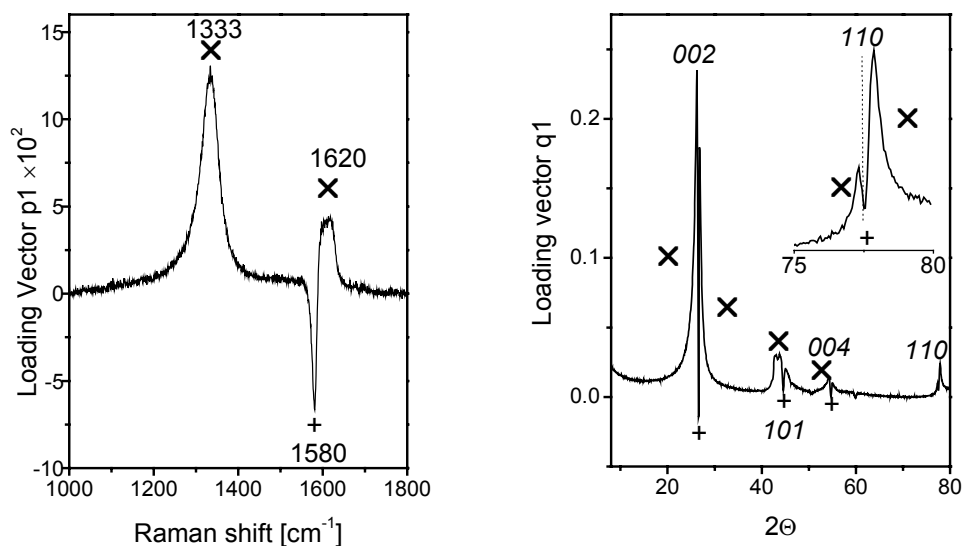


Abb. 42: First component p1 for the **X** (left) and q1 for the **Y** descriptor (right). The first component corresponding to the Raman data set (left) has three main features, two positively correlated, marked by \times , appearing at 1333 and 1620 cm^{-1} and one feature negatively correlated with the above cited at 1580 cm^{-1} , marked by $+$. The first component found in the XRD data set (right) has several positively correlated features which correspond to the broadening of the graphite reflections, marked by \times , and several features negatively correlated with the latter ones, marked by $+$, which correspond to the original sharp graphite reflections.

Several XRD features marked by \times in Abb. 42 (right) are positively correlated and represent the broadening and asymmetry of the 002, 100-101, 104 and 110 graphite reflections. These features, marked by \times , are negatively correlated with the sharp 002, 100-101, 104 and 110 reflections, marked by $+$. Hence, all reflections broaden simultaneously and exhibit an asymmetry, especially the 002 and 110 reflections.

The Raman bands marked by \times are positively correlated with the broadening of the XRD reflections also marked by \times . Simultaneously, the Raman spectral feature, marked by $+$, is negatively correlated with the broadening of the XRD reflections, marked by \times , but positively correlated with the 002, 101, 104 and 110 reflections marked by $+$. The inset of Abb. 42 (right) shows the 110 reflection for which the broadening and the asymmetry is positively correlated with the Raman spectral features 1333 and 1620 cm^{-1} and negatively correlated with the Raman spectral feature at 1580 cm^{-1} .

The score plot of the first component is presented in Abb. 43. The progression of the milling time is indicated by the arrow. The samples with lower milling times are located to the left and the samples with higher milling times are located to the right of the scores plot. A perfect linear correlation $R^2=1$ was not found in the linear PLS model relating the $Y(u1)$ and $X(t1)$ scores. The reason for this could be the low number of samples studied and/or that up to a certain amount of crystallite reduction no significant changes can be appreciated with XRD. However Raman is still able to determine them. Thus, up to a critical level XRD may not be so much affected by structural changes as Raman spectroscopy.

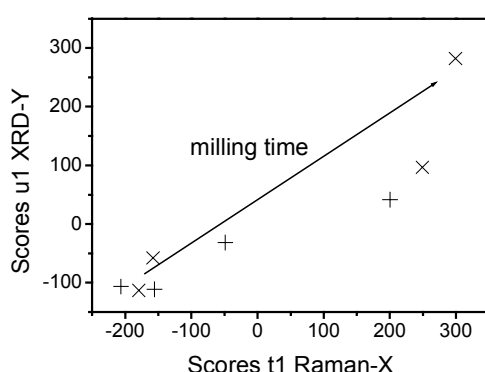


Abb. 43: Score plot of the first component t1 for the **X** descriptor and u1 for the **Y** descriptor. As the first component t1 increases upon milling so increases the first component u1.

The residuals, representing the difference between the experimental and the estimated spectra, give information about the quality of the model. The residuals for the same sample h168 for both the X_{ith} and Y_{ith} descriptors are plotted in Abb. 44. The proposed model for the **X** descriptor fits very well the observations for which the residual maximum value is 8%, see Abb. 44 (left). The residuals of the **Y** descriptor are slightly higher up to 15%. The higher differences between the model and the experimental diffractograms are observed for the modelling of the 002 reflection, see Abb. 44 (right). The low number of samples studied is responsible for errors. Increasing the number of samples will make the model more robust.

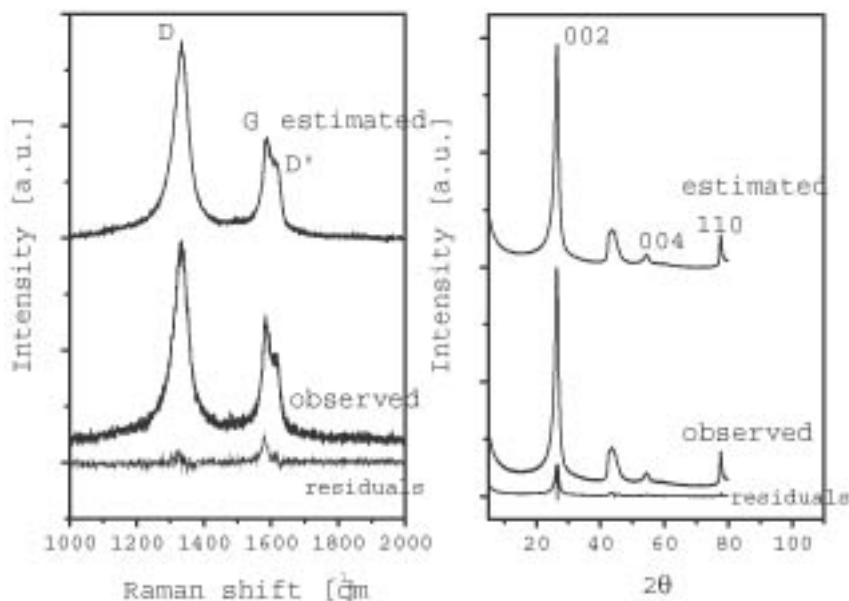


Abb. 44: Residuals corresponding to a milled sample after 168 hours in the absence of hexane for the Raman spectra (left) and for the XRD diffractogram (right).

To further study the relationship of the Raman forbidden modes and the broadening of the [00l] and $\{hk0\}$ directions, the XRD diffractogram is split into two regions, and two different models are calculated taking into account the structural anisotropy: a) reduction of the crystallite size in the [00l] direction and b) in the $[hk0]$ direction. The captured percentage of variance is given in Tab 9.

The first loading vectors for both the two **X** and the **Y** descriptors of these two models are plotted for comparison together with the whole PLS-XRD model and shown in Abb. 45. There is no significant difference in the first component, p_1 , of the **X** descriptor for the three models (Abb. 45 top). The **Y** descriptors are also presented in Abb. 45 for the PLS models of the [002] (middle) and [110] (bottom) crystallographic directions, respectively. There is a slight difference between the first component, q_1 , for the whole XRD and the model of the [002] direction (Abb. 45 middle). The first component, q_1 , for the whole XRD and the model of the [110] direction are almost identical (Abb. 45 bottom). The only difference is a scaling factor between both first components, q_1 . These results further prove the positive correlation found between the Raman-forbidden features and the broadening of the XRD reflections.

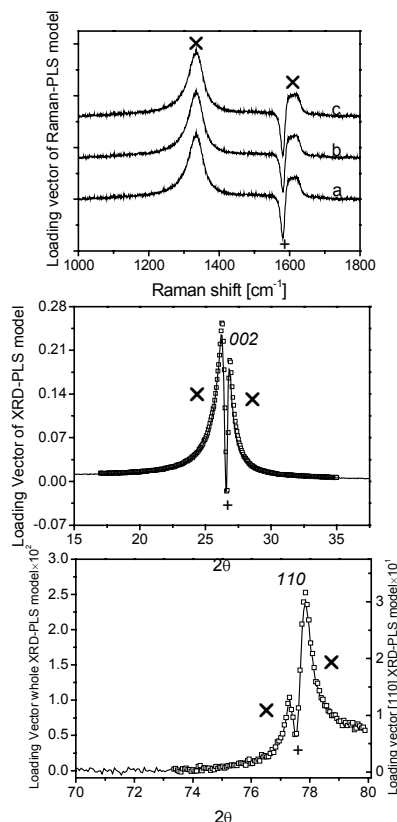


Abb. 45: Comparison of different PLS Raman-XRD models. (A) 1st PC, p1, of the PLS analysis for 3 different models: a) \mathbf{Y} descriptor, whole XRD-diffractogram; b) \mathbf{Y} descriptor, [002] direction; and c) \mathbf{Y} descriptor, [110] direction. Positively (×) correlated modes and negatively (+) correlated mode. (B) 1st PC, q1, of the \mathbf{Y} descriptor: whole XRD-diffractogram line (solid line), (box) model for the [002] direction, see the broadening and asymmetry (×) and the sharp 002 reflection (+). (C) 1st PC, q1, of the PLS analysis of the \mathbf{Y} descriptor: whole XRD-diffractogram (right) and model of the [110] direction (left). See the positive correlation of broadening and asymmetry (×) and the negative correlation of the sharp 110 reflection (+).

6.2.2.6 SIMPLISMA: identification of pure Raman spectral components

SIMPLISMA is a mathematical approach, which finds the minimum number of independent pure components, which reconstruct the original spectra [8]. In the experimental Raman spectra of graphite, two pure spectral components were found by SIMPLISMA. The first component the so called pristine graphite is identified by one Raman band at 1580 cm^{-1} which arises from the E_{2g} vibrational mode (Abb. 46). The second component exhibits three bands located at 1150 , 1333 , and 1620 cm^{-1} attributed to the decrease of coherence lengths by XRD. Tab 10 shows the progression in intensity contributions from HOPG and the milled graphite materials. The reference sample, HOPG, possesses almost exclusively the pure spectral component of pristine graphite. When the material is milled, the spectral component of pristine graphite decreases and the component associated with disorder/size-induced modes increases in importance.

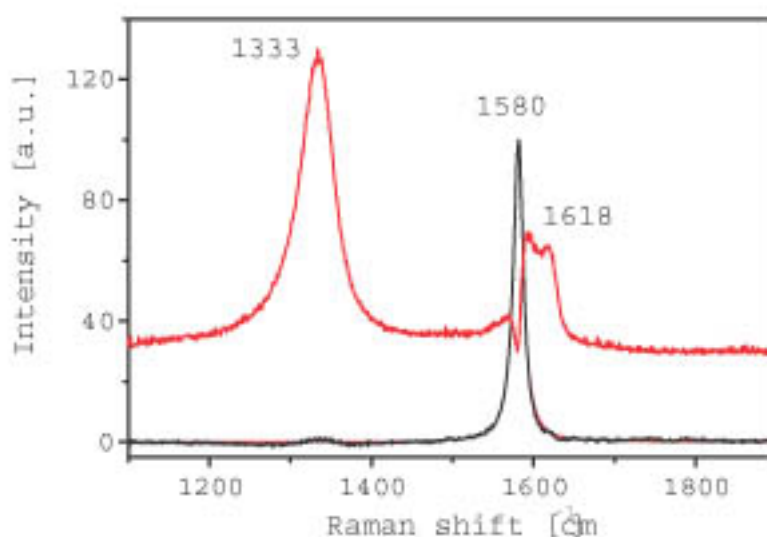


Abb. 46: Pure spectral components found in the first-order Raman spectrum of graphite. The first spectral component has only one stretching mode at 1580 cm^{-1} (bottom), assigned to the E_{2g} vibrational mode of HOPG. The second one presents two main bands appearing at 1333 and 1620 cm^{-1} , and a slight shoulder at 1150 cm^{-1} (top).

Tab. 10: SIMPLISMA analysis of the Raman spectra for the mechanically activated samples. The starting material and HOPG were included in the analysis. The mean and the standard deviation of each pure spectral component: pristine graphite band at 1580 cm^{-1} and milled with bands at 1150 , 1333 , and 1620 cm^{-1} is shown for each sample.

Sample	Spectral component (%)	
	Pristine-graphite	Decrease XRD coherence length
HOPG	95.76 ± 3.41	4.23 ± 3.41
<i>starting</i>	36.43 ± 1.46	63.56 ± 1.46
Mechanically activated samples		
h3	26.29 ± 5.81	73.70 ± 5.81
h24	30.14 ± 4.91	69.85 ± 4.91
h72	19.96 ± 2.81	80.03 ± 2.81
h168	12.56 ± 0.98	87.43 ± 0.98
d3	29.30 ± 9.94	70.69 ± 9.94
d24	27.85 ± 9.72	72.14 ± 9.72
d72	10.64 ± 1.34	89.35 ± 1.34
d168	5.39 ± 0.74	94.60 ± 0.74

6.2.2.7 On the simultaneous appearance of the D and D' bands in the first-order Raman spectrum of graphite

In the literature these Raman-forbidden modes are associated with maxima in the phonon dispersion curves for different directions of the Brillouin zone [1,49]. A comparison of the phonon dispersion curves with the identified pure spectral Raman components may help in understanding the evolution of the Raman spectra upon mechanical activation. To illustrate this, the phonon dispersion curves from Al-Jishi *et al.*¹ calculated from the Born-von-Kármán model are also shown in Abb. 47 (left). This comparison clarifies the relation of the different Raman bands with the phonon states in different crystallographic directions. The Raman band at 1580 cm^{-1} is caused by the E_{2g} vibrational mode at the zone center. The very weak Raman forbidden band at 1150 cm^{-1} may arise from the density of states at the horizontal branch of the phonon dispersion at the M point. The most important disorder-induced Raman line at 1333 cm^{-1} accordingly may be caused by the high density of states for zone-boundary phonons in the MK or $[-110]$ direction. Finally, the disorder-induced Raman line at 1620 cm^{-1} could be caused by the high density of states of mid-zone phonons in the GM or $[110]$ direction. The density of phonon states in the KG direction may also contribute to this band. This comparison between phonon dispersion curves and the pure spectral components may indicate that changes in crystallite size especially in the $[110]$ direction, and possibly in the $[100]$ direction too, could be correlated with changes of the Raman band at 1620 cm^{-1} . Changes in the crystallite size in the crystallographic $[\bar{1}10]$ direction hence should be related to the band at 1333 cm^{-1} .

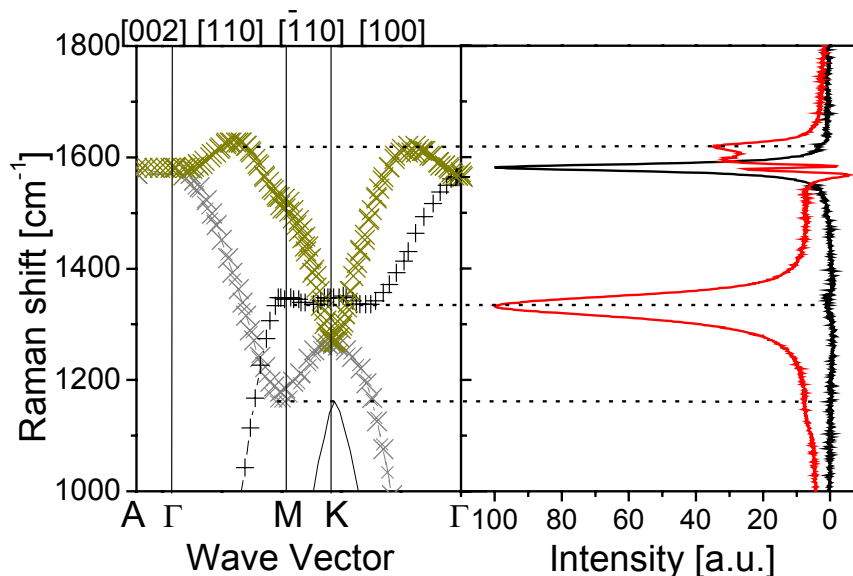


Abb. 47: 3D-Phonon dispersion curves calculated from the Born-von Kármán¹ model (left) and the pure spectral components found with SIMPLISMA (right).

Abb. 48 shows an electron diffraction pattern of the *starting* graphite showing the characteristic spots for the 100, 110, and the $\bar{1}10$ reflections of the graphite structure. It is noted, that the $[110]$ and $[\bar{1}10]$ crystallographic directions are not symmetric, and have not the same d-spacing value. Both directions have different d-spacing values and are not crystallographic equivalent. Abb.49 shows these two crystallographic directions in real space.

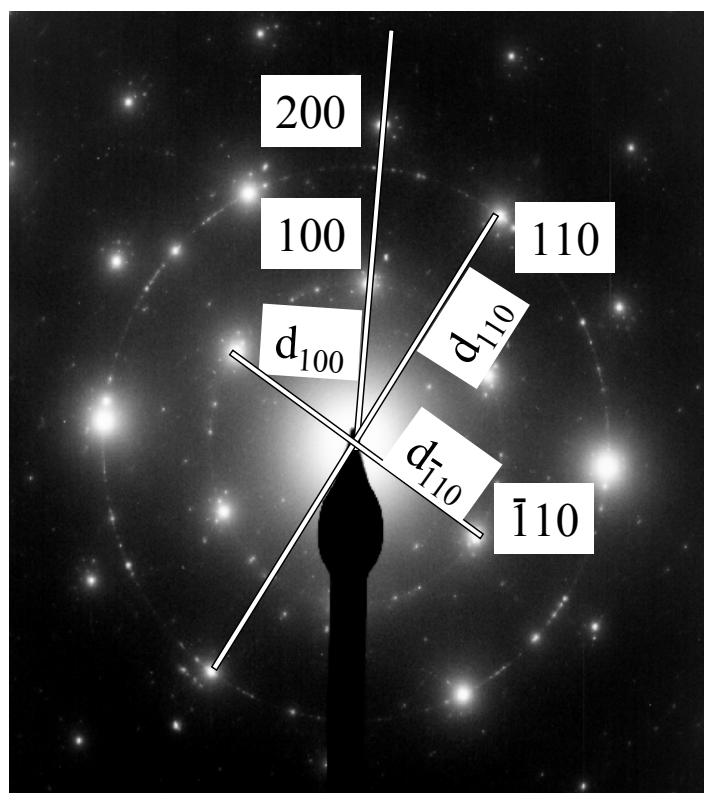


Abb. 48: Electron diffraction pattern of the *starting* material showing the 100, 110 and -110} reflections. The [100], [110], and [-110] directions as well as their respective d-spacing values are showed. The [110] and [-110] have different d-spacing values and are not crystallographic similar.

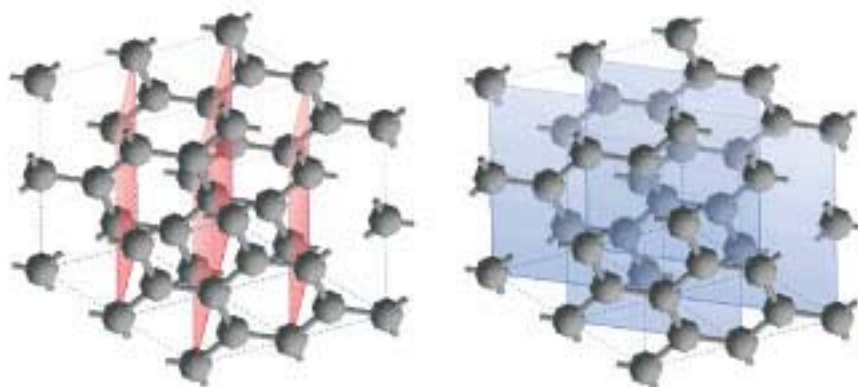


Abb. 49: The [110] and [-110] crystallographic directions in the graphite lattice. Both directions are clearly different, with different d-spacing values and different number and position of carbon atoms in each direction.

Abb. 50 shows a scheme of a graphene sheet with these two directions indicated which are related to the Raman-forbidden modes located at 1333 and 1620 cm^{-1} . Every disruption of a graphite layer will influence the coherence lengths in both directions as indicated by the dotted line. Therefore, if the XRD coherent graphite zones are reduced in size, e.g. by mechanical milling, the lattice

directions $[-110]$ and $[110]$ are both affected, and both bands at 1333 and at 1620 cm^{-1} appear simultaneously. Each carbon atom has two nearest carbon atoms in the $[-110]$ direction at a distance of 2.456 Å , while in the $[110]$ direction each carbon atom has one nearest carbon atom at a distance of 1.415 Å and the next nearest one at a distance of 2.834 Å . It is reasonable that the shortest C-C length of 1.415 Å should be related to the highest stretching frequency of 1620 cm^{-1} , while the increase of the two nearest carbon atoms distance to 2.456 Å is associated with the lower stretching mode frequency of 1333 cm^{-1} .

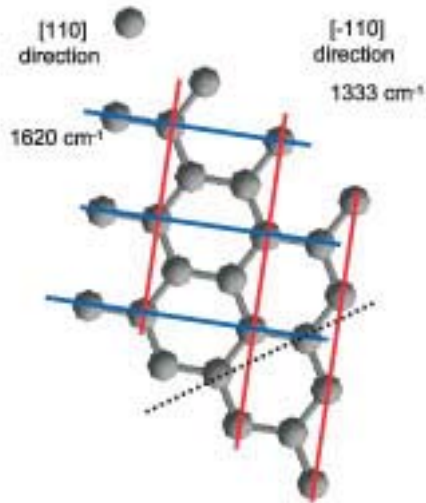


Abb. 50: Illustration proposed for the simultaneous appearance of two Raman forbidden modes. Any cut in the graphite lattice represented by the dotted line or any point defect affects both the $[110]$ and $[-110]$ crystallographic directions.

This explanation demonstrates why these two Raman bands appear simultaneously and form one component in the Raman spectrum of size-reduced graphite.

6.3 Electronic structure of the mechanically activated graphite

This section describes the investigations of the electronic structure of representative samples. The measurements conducted with XPS, UPS He II, and EELS showed no significant differences between the surface electronic structure of milled and the starting pristine graphite. On the other hand, a much more surface sensitive method such as NEXAFS shows a loss of the graphitic character upon milling under dry conditions.

6.3.1 X-ray photoelectron spectroscopy

The C1s and O1s spectra of the *starting* material and the milled material after 168 hours in presence and absence of hexane are presented in Abb. 51 and 52, respectively.

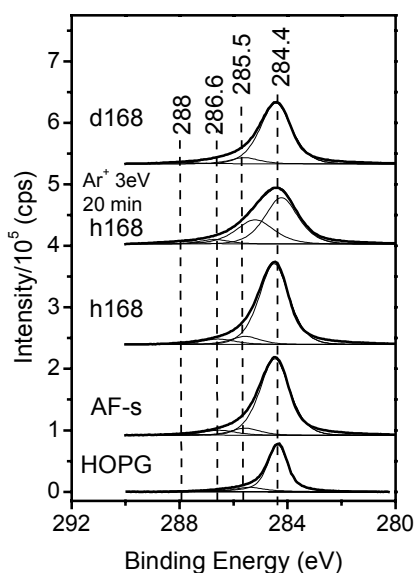


Abb. 51: C1s XPS spectra of the milled graphite samples after 168 hours in both presence and absence of hexane, HOPG, *starting* material, and sputtered graphite after milling in the presence of hexane for 168 hours.

HOPG was also investigated as a highly ordered reference material and in order to study a highly disordered material the sample h168 was submitted to sputtering with Ar⁺ at 3.5 keV for 20 minutes. Tab. 11 summarizes the results of the analysis of the C1s spectra. The C1s spectra can be separated into different contributions: the C1s peak corresponding to graphite is located at ~284.4 eV. The asymmetric Gauss deconvoluted Doniach-Sunjić (DS*) function was used to fit its characteristic profile [44,62,75], for the HOPG sample. The peaks of the other samples were fitted with a combined convoluted Gauss Lorentz function.

HOPG can be clearly distinguished from the *starting* and milled samples. It has a higher content of the 284.4 eV graphite species (85.3%) and a smaller FWHM of the Gauss (0.4 eV) and of the Lorentzian (0.7 eV) component. The content of this species in the *starting* and the milled samples varies between 82 to 83%. The FWHM is similar for the *starting* and h168 samples (1.4 eV) and

slightly increases to a value of 1.5 eV for the d168 sample. Sputtering in Ar⁺ clearly decreased the content of this species to 57.9% and the FWHM value was found to be 1.6 eV. The results are summarized in Tab. 11.

Additional peaks in the C1s spectra can be attributed to several carbon atoms in different chemical environments such as C-H (285.5 eV), C-OH (286.6 eV), and C=O (288.1 eV), respectively. HOPG has a lower content (13.58%) and a sharper FWHM (1.27 eV) of the C-H component at 285.4 eV compared to the *starting* and milled samples. The contents of the species related to non graphitic carbon in the *starting* sample is 8.6% and in the samples milled under hexane 9.1% and 8.8% in the absence of hexane. These slight differences do not allow a differentiation between the *starting* and the milled samples. However, sputtering significantly increased the content of the 285.4 eV species to 34% and the profile of this peak broadened to 1.8 eV. The species of oxygenated groups located at 286 eV and 288 eV varies between 7.8 % (*starting*), 7.2 % (h168) and 8.9 % (d168), respectively. The sample d168 has a greater amount of these species. Since these groups are located at dangling bonds, terraces, prism faces and defects, this is an indirect proof that sample d168 has a higher concentration of defects than the *starting* and h168 samples.

Tab. 11: Comparison of the C1s fitting for HOPG, the starting sample and the h168 and d168 samples. The sample h168 was sputtered in Ar⁺ at 3keV for 20 min. The C1s signal of HOPG was fitted with the asymmetric Gaussian convoluted DS function and the other peaks with GL functions. Γ and C are the respective FWHM and the content of each signal.

Sample	C1s π			C-H			C-OH			C=O		
	BE	Γ	C.	BE	Γ	C.	BE	Γ	C.	BE	Γ	C.
	[eV]	[eV]	[%]	[eV]	[eV]	[%]	[eV]	[eV]	[%]	[eV]	[eV]	[%]
HOPG	284.4	0.4G 0.7L	85.3	285.4	1.3	13.6						
starting	284.4	1.4	83	285.5	1.4	8.6	286.5	1.6	6.2	288	1.6	1.3
h168	284.5	1.4	83	285.5	1.3	9.1	286.5	1.6	6.2	288	1.4	1
h168 sputtered	284.2	1.6	57.9	285.2	1.8	34	286.7	1.4	4.8	288	1.6	2.2
d168	284.5	1.5	82.3	285.6	1.4	8.8	286.6	1.6	6.7	288	1.6	3.1

The O1s spectra show three different chemical environments for oxygen, which can be assigned to C-O, C=O (~530.7-9 eV), OH (~532.5 eV), and adsorbed H₂O (~533.8 eV), shown in Abb. 52.

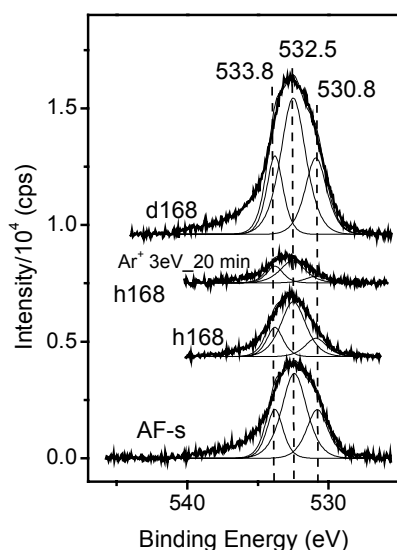


Abb. 52: O1s XPS spectra of the milled graphite samples after 168 hours in both presence and absence of hexane, *starting* material, and sputtered graphite after milling in the presence of hexane for 168 hours.

The results of the profile fits are presented in Tab. 12. Milling in the presence of hexane does not cause oxidation of the sample, in contrast to milling in absence of hexane clearly increases the oxygen content. The sample d168 has the highest concentration of OH functional groups compared to the rest of samples.

Hexane covers the graphite flakes and retards or prevents its oxidation. The low amount of oxygen found in the sample h168 may be possible due to diffusion of O₂ through the hexane film or to the reaction of the dangling bonds created with the hexane present, both facts hinder the reaction of oxygen from the atmosphere with the created dangling bonds. The sputtering with Ar⁺ eliminates oxygen groups from the surface as seen in Abb. 52 and Tab. 12. The amount of oxygen found on the surface of the samples was 2.25% for the *starting* material, 1.20% for the h168, and 4.26% for the d168 samples, respectively. Sputtering decreased the amount of oxygen to 0.60%. The ratios of the three species remained approximately the same for all the samples, which indicates the similarity of the oxygen environment in these samples. The shoulder at higher binding energies 535 eV cannot be assigned to any oxygen group and its presence is explained by sample charging indicating the transformation of the conducting in a partly insulating sample. The more defective the sample is the more pronounced is this effect. No signs for impurities such as Al or Si were found.

Tab. 12: Comparison of the O1s fittings for the starting sample and the milled samples h168 and d168. Additionally, the h168 sample was sputtered with Ar⁺ for 20 min with energy of 3 keV. All fits were conducted with combined Gauss-Lorentzian functions.

Sample	C=O			C-OH			H ₂ O		
	BE [eV]	Γ [eV]	Area [cps×10 ³]	BE [eV]	Γ [eV]	Area [cps×10 ³]	BE [eV]	Γ [eV]	Area [cps×10 ³]
starting	530.9	2	4.3	532.4	2.3	8.5	533.3	1.5	3.2
h168	530.9	2	1.6	532.5	2.3	5.5	533.3	1.5	1.9

h168	530.7	2	0.6	532.5	2.3	2.2	533.3	1.5	1.1
sputtered									
d168	530.8	2	6.7	532.5	2.3	13.7	533.8	1.5	5.1

6.3.2 Ultraviolet photoelectron spectroscopy

The spectra of the *starting* and the milled material in the presence of hexane shown in Abb. 53 are similar. This indicates that the electronic structure of the valence electrons of graphite is still intact in agreement with the XPS results despite the loss of long-range order as seen in XRD, Raman, and HR-TEM.

The valence band spectra of graphite consist of two main features appearing at ~ 7.6 eV and ~ 2.9 eV which correspond to π - σ and π bonds, and a weak π band at ~ 16.7 eV [44,62]. The graphite samples corresponding to the *starting* and the milled material in the presence of hexane have similar bands and do not differ much from each other. In contrast, the sample sputtered in Ar^+ which differ significantly from the before mentioned samples and the sample milled in the absence of hexane which showed a slight difference. The sample milled in the absence of hexane presents a more defined shoulder at ~ 8.9 - 10 eV which corresponds to a contribution of the O2p band underlying the graphite spectrum. However, this sample contains similar spectroscopical features like the other graphite samples. The sputtered sample exhibits more pronounced differences in the valence spectra with the rest of the samples. The π and the π - σ bands located at 2.9 and 16.7 eV disappear in the sputtering process. The π - π band at ~ 9 eV broadens and the fine structure of the valence band spectra is lost. The region near the Fermi level is more populated due to the creation of localized states (defects) near the Fermi level. All these effects are a result of the amorphization and introduction of disorder in the graphite structure. Sputtering in Ar^+ destroys the long range order of the graphite structure and the metallic electronic structure is lost as can be seen by the increase of emission near E_f arising from strongly localized defect states in the valence band spectra and the loss of the characteristic π bands.

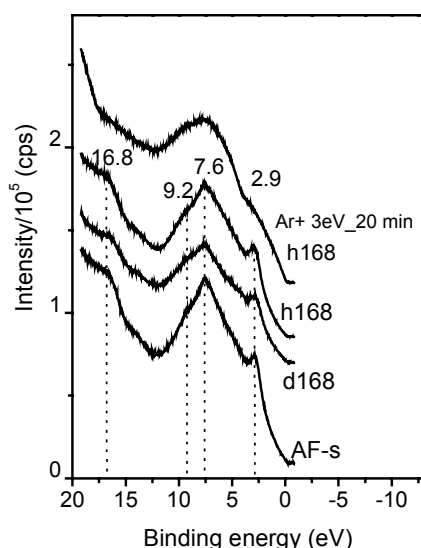


Abb. 53: UPS HeII valence band spectra of the milled graphite samples after 168 hours in both presence and absence of hexane, *starting* material, and sputtered h168 sample.

6.3.3 Electron energy loss spectroscopy

The EELS spectra of the milled graphite samples are presented in Abb. 54 along with EELS spectra of the *starting* and sputtered graphite.

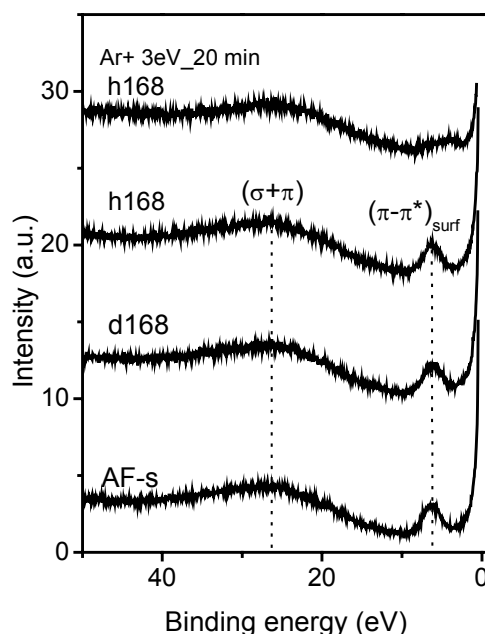


Abb. 54: EELS spectra of *starting* graphite (bottom curve), milled graphite in presence and absence of hexane after 168 hours, and sputtered h168 sample (top curve).

The spectra are calibrated to the same intensity of the inelastic peak at 0 eV. The pronounced peak located at 6.4 eV in all graphite samples except the sputtered graphite arises from $\pi-\pi^*$ transitions (surface plasmon). Sputtering with Ar^+ results in a decrease of the $\pi-\pi^*$ transition band intensity and a shift to lower energies, indicating the amorphization of the sample in agreement with the XPS and UPS results. The broad peak occurring at about 27 eV is associated with plasmon excitations involving all valence electrons per atom ($\sigma+\pi$). Again no significant differences could be found between the milled graphite and the *starting* samples. Regarding the $\pi-\pi^*$ and the ($\sigma+\pi$) peak intensities and positions no significant changes were observed between the *starting* and the milled samples, also in agreement with the XPS and UPS results.

6.3.4 K-edge X-ray absorption spectroscopy

A much more sensitive technique to the chemical environment of carbon atoms is carbon K-edge X-ray absorption spectroscopy (XAS), in which core electrons are excited into non occupied orbitals in the valence band. There are two kinds of resonances arising from transitions into flat portions of the various unoccupied σ and π bands [3,70]. The main features are an excitation into the antibonding π -band in the region of the M-Point around at 285.4 eV and a doublet with σ symmetry, which appears at 292.2 and 293.1 eV. It is known that the latter is very sensitive to structural modifications of graphite. The *starting* and the d168 samples are shown in Abb. 55. The integrated intensity of the π^* resonance provides information of the amount of graphitic structures

present in a sample [3]. The comparison between the integrated intensity of the π^* resonance, from 1.27 a.u. to 1.03 a.u., clearly shows the decrease of the amount of the graphitic structures upon milling due to the introduction of defects.

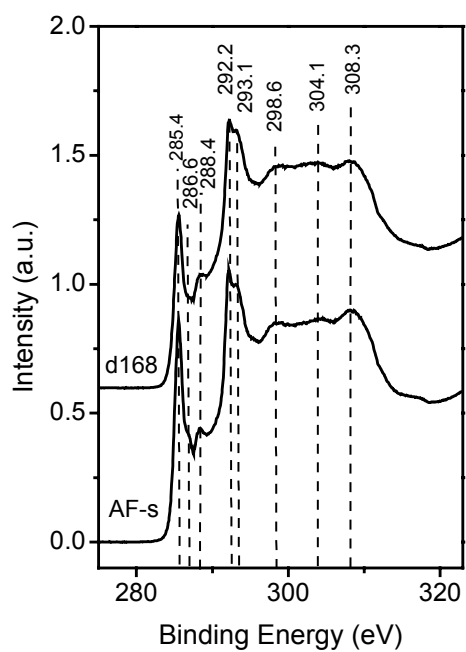


Abb. 55: XAS comparison of for the starting (bottom curve) and milled graphite in absence of hexane after 168 hours (top curve).

7 Chemical reactivity of the mechanically activated graphite

7.1 Combustion reactivity of mechanically activated graphite

This section describes the combustion of the mechanical activated graphite with molecular oxygen. The calculation of the apparent Activation energy for the combustion was calculated using the Kissinger Method.

7.1.1 Introduction

The gas phase reaction of oxygen with carbon was used as a test reaction to study the effect of mechanical milling in the reactivity of graphite. This reaction was followed by thermogravimetric (TG/DTG) methods. This study is not interested in the mechanistic aspects of this reaction but in the trend of the reactivity and its correlation with the observed structural changes. Thus, the main subject of this study is to find a correlation between changes in the graphite structure and the consequences for its chemical reactivity as probed by the combustion. The structural changes observed in the previous chapters, decrease of the crystallite size in both [002] and [110] directions, should affect the combustion reactivity of the milled samples. Therefore, quantitative and qualitative changes in the amount of C_a (BASAL PLANES) and C_b (DEFECTS) sites are expected to occur upon milling. These sites, which are necessary for the combustion, are postulated to affect the combustion reactivity in two different ways. The C_a (BASAL PLANES) donate electrons to the O_2 molecule resulting in the activation of this molecule and the C_b (DEFECTS) sites are responsible to fix the activated oxygen species to the carbon sample.

The extraneous lattice energy in form of structural defects [8,58,69] and the existence of different types of structural disorder may be responsible for different combustion behaviors and may lead to different activation energies (E_a) of combustion. An important objective is the identification of highly reactive species with low E_a for the combustion process and the correlation of their structure with their effect on the reaction.

7.1.2 Results

Abb. 56 shows the effect of the milling on the DTG signals of the samples milled under dry conditions. The experimental conditions were the same for all runs: the samples were ramped in a continuous flow of 100 ml ($N_2:O_2=1$)/min with a heating rate ϕ of 0.5 K/min.

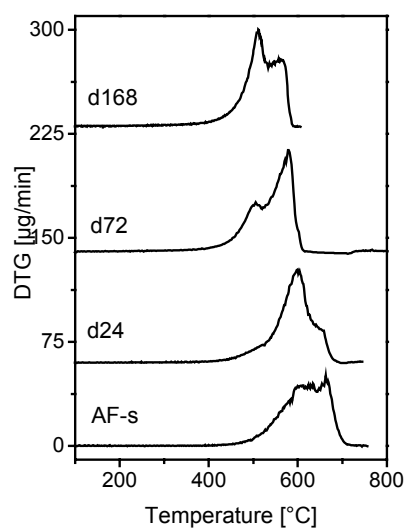


Abb. 56: Effect of the milling time in the reactivity of the dry milled samples.

As the material is progressively milled, an increase in the reactivity is clearly observed. This enhancement of the reactivity is observed by an overall downshift of the onset temperature and of the end temperature.

The development of two peaks can be clearly appreciated, as the first peak becomes more prominent with increasing milling for the dry series. At the same time, milling in the presence of hexane also causes an increase in the reactivity with molecular oxygen, as shown in Abb. 57.

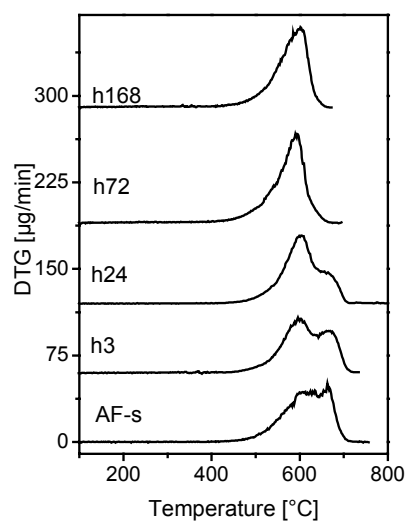


Abb. 57: Effect of the milling time in the reactivity of the hexane milled samples.

The development of the DTG signal with milling time is quite different for the series milled in the presence of hexane. In this case only one main peak develops as the material is milled. The time scale does not play such an important role in the variation of the DTG peak. The onset temperature lies between the one of the *starting* material and the one of the material milled under dry conditions.

Tab. 13 lists the onset and end of combustion temperature for the *starting* and the milled samples.

Tab. 13: Comparison between the on-set and end temperature of combustion of the two catalyst series in the TPO-DTG profiles Experimental conditions: heating rate 0.5 K/min, reactant flow 100 ml (O₂:N₂=1) /min}. Apparent activation energies calculated from the TPO experiments using the Kissinger's method [34].

Oxidation behaviour					
Sample	Temperature				
	On-set [C]	End [C]	1. peak [C]	2. peak [C]	E _a [kJ/mol]
starting	500	709	616	666	155±18 (1) 180±12 (2)
h3	515	706	598	662	-
h24	504	703	599	658	
h72	489	651	590		188±12
h168	490	641	596		185±8
d24	458	677	596	649	
d72	455	604	504	571	163±11 (1) 195±9 (2)
d168	419	583	508	561	158±2 (1) 199±6 (2)

7.1.3 Calculation of apparent activation energies of combustion

The differences in reactivities led us to determine the apparent E_a of the carbon combustion. Previously, other workers [57,8] have used the Kissinger method [34], to determine the E_a of a process with the aid of the TG apparatus. Each peak in Abb. 56 and 57 is associated with the maximum weight loss rate and is related to a E_a value of that combustion process.

7.1.3.1 Kissinger method

The Kissinger method to determine the apparent E_a of a process is based on the following equation:

$$\ln\left(\frac{\phi}{T_{\max}^2}\right) = \frac{E_a}{RT_{\max}} + C \text{ (eq.11),}$$

where $\{\phi\}$ is the heating rate, T_{\max} the temperature at which the maximum oxidation rate occurs, E_a the activation energy of the process, C a constant, and $R=8.31$ kJ/mol the ideal gas constant. Plotting $\ln(\phi/T_{\max}^2)$ versus $1/T_{\max}$, the activation energy can be obtained from the temperature of the maximum oxidation rate, equation 11. It is assumed [34] that the oxidation rate maximum occurs at the maximum of the DTG signal. With increasing heating rate, the amount of sample tested is inversely varied. This correlation avoids diffusion problems of the reaction products CO and CO₂ and ensures working under differential conditions. It is recommend following the DTG signal since its background line is well known and remains constant between different measurements.

Only the samples h72, h168, d72, and d168, as well as the *starting* material, were included in this analysis. Tab. 13 lists the calculated E_a for carbon combustion. It can be appreciated that the different milling conditions cause the appearance of two well resolved E_a values for the d series, see Abb. 56. The first peak of the DTG signal has a lower E_a than the second one indicating an easier combustion. On the other hand, the material milled in hexane presents only one E_a . If different kinetic parameters are involved in the reaction for both series, this may indicate a modification in the oxidation mechanism due to different carbon structures. The E_a value associated with the first peak for the d series lays around 160 kJ/mol while the second corresponds to a value of 190 kJ/mol. The latter E_a value is similar to the value obtained for the fresh and h series, around 180-190 kJ/mol}. This indicates that similar structures are involved in the combustion process for the latter case, while the 160 kJ/mol is associated with structures that are more reactive toward combustion. The hexane milled samples reveal only changes in the pre-exponential factor A [40] without detectable changes in E_a . This is attributed to more available active reaction sites for the samples milled in presence of hexane, than in the *starting* material.

7.2 Catalytic activity of the mechanically activated graphite

This section describes the catalytic activity of the mechanical activated graphite in the partial oxidation of MeOH to CH₂O. Response surface methods helped to determine the effect of the temperature and the MeOH:O₂ ratio in this reaction. Characterization of the samples after reaction was conducted to determine whether structural changes occurred during reaction. Thermal desorption spectroscopy (TDS) experiments were also conducted to study the production of different oxygenated CO_x groups on the carbon substrate at reaction temperatures.

7.2.1 Characterization after reaction

The results of the characterization of the milled samples after reaction are presented in Tab. 14. A weight loss was detected for the milled samples in the absence and presence of hexane, especially for the d72 and d168 samples around 10 and 20 % respectively. The samples h168 and *starting* did not show any significant mass losses after reaction. Milling increased the BET surface area, especially in presence of hexane with a surface area 8 times larger than the *starting* material. XRD analysis showed an increase of the XRD coherence lengths in both the [002] and [110] directions after catalysis, especially for the milled samples in absence of hexane. The crystallite size of the [002] direction changed significantly for the samples d72 and d168 after reaction from 93 to 106 pm and from 49 to 58 pm, respectively. The crystallite size was determined using the Scherrer formula. The crystallite size of the [110] direction increased after reaction from 178 to 193 pm and from 142 to 151 pm for the d72 and d168 sample, respectively. The position of the 002 peak for the d168 sample shifted from 338 to 336 pm after catalysis. Also the 002 and 110 peaks became less asymmetric as indicated by the increase of the m_L and m_R fitting factors. All these changes in the less crystalline samples correlate with amorphous structures burned-off during reaction. The oxygen content was determined before catalysis with XPS and shows that milling in absence of hexane resulted in an increase of the amount of CO_x groups on the surface.

Tab. 14: Effect of the reaction MeOH:O₂ in the structural parameters of the milled graphite catalysts. Split-Pearson VII fit of the XRD diffractograms, m_L = low angle exponent associated to asymmetry toward higher d-spacing values and m_R = right angle exponent associated to asymmetry toward lower d-spacing values (a.r. = after reaction).

Sample	Weight loss	BET [m ² /gr]	XRD					
			d_{002} [pm]	Γ_{002} [2 θ]	m_L	d_{110} [pm]	Γ_{110} [2 θ]	m_R
<i>starting</i>	--	11	335	0.255	1.975	123	0.316	4
h168	--	88.1	335	0.576	0.723	123	0.386	1.83
a.r.			335	0.536	0.882	123	0.42	6
d72	+	32.7	336	0.778	0.778	123	0.508	0.90
a.r.			336	0.681	0.713	123	0.469	3.88
d168	++	22.4	338	1.445	0.618	123	0.635	0.51
a.r.			336	1.249	0.69	123	0.598	2.03

7.2.2 Thermal desorption spectroscopy of oxygen complexes

The studied samples were the *starting* and the milled material in the absence of hexane d168. The samples were first ramped to 1173 K and then were pre-treated at 748 K with oxygen at a partial pressure of 0.2 mbar. The election of the pre-treatment temperature was due to the identification of oxygen complexes at reacting conditions in which graphite was known to be active for the partial oxidation of methanol.

7.2.2.1 TDS spectra of samples *starting* and d168

The TDS spectra of the samples *starting* and d168 are shown in Abb. 58 and 59. The main gases that desorb are CO₂ and CO, as well as H₂O and H₂.

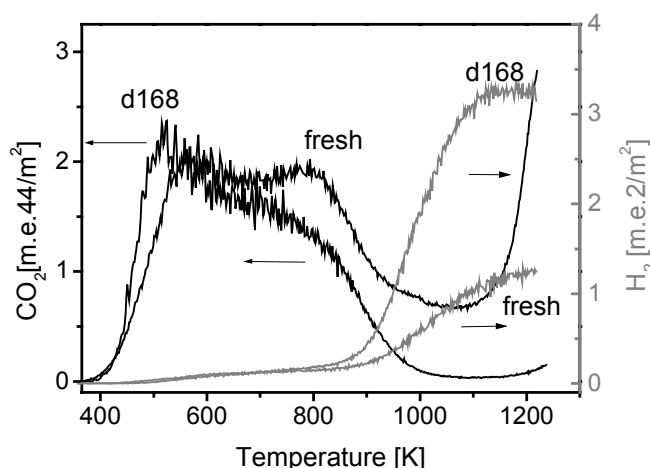


Abb. 58: TDS spectra for the desorption of CO₂ and H₂ corresponding to the *starting* and d168 samples

In case of the *starting* sample, the onset temperature for the desorption of CO₂ is at 400 K (Abb. 58). Two maxima appear at 585 and 774 K, respectively. As the temperature is increased further, the desorption of CO₂ decreases, to strongly increase above 1100 K. On the other hand, the CO₂ desorption temperature of the first event is lowered to 400 K and in addition more CO₂ is evolved for the sample d168. Furthermore, one maximum at 531 K and a shoulder at 740 K are detected. As in case of the *starting* sample, the desorption decreased upon increasing temperature, but with further increasing temperature a similar desorption of CO₂ was not detected. This is correlated with the presence of a higher concentration of C-H groups on the surface of mechanically activated carbon compared to the fresh material as evidenced with H₂ traces and in agreement with previous results. The H₂ desorption started at 480 K for both samples. The *starting* sample increased the H₂ desorption strongly increased at temperatures higher than 900 K for the *starting* sample to level off at still higher temperatures. Three to four times more H₂ desorbed from d168 than from the *starting* sample at temperatures above 900 K. The CO desorption started at 500 K from the *starting* sample with one broad peak at 891 K and raised again at 1169 K, see Abb. 59. The onset of the CO desorption was at 460 K for the sample d168 with one maximum at 828 K and decreased with further increasing temperature. The desorption of H₂O started at 400 K for both samples (Abb. 59) with a maximum desorption at 636 K, but the sample d168 also showed one shoulder at 530 K. The surfaces of both samples are covered with a similar amount of H₂O. The amount of CO and CO₂ is also similar both samples at lower and moderate temperatures. But at temperatures above

1000 K the *starting* sample presents more groups desorbing as CO and CO₂. This is explained by a larger amount of H₂ on the surface of d168. This sample has a higher concentration of defects, which are saturated with superficial groups.

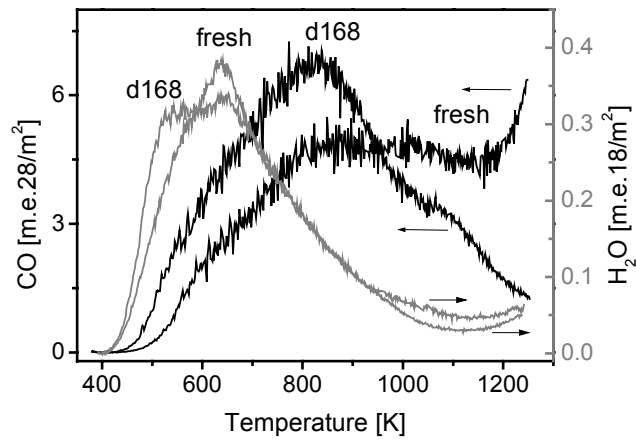


Abb. 59: TDS spectra for the desorption of CO and H₂O corresponding to the *starting* and d168 samples

7.2.2.2 TDS spectra of *starting* and d168 samples after O₂-748 K treatment

Abb. 60 shows the desorption of CO₂ for the *starting* and the d168 samples after O₂ treatment at 748 K.

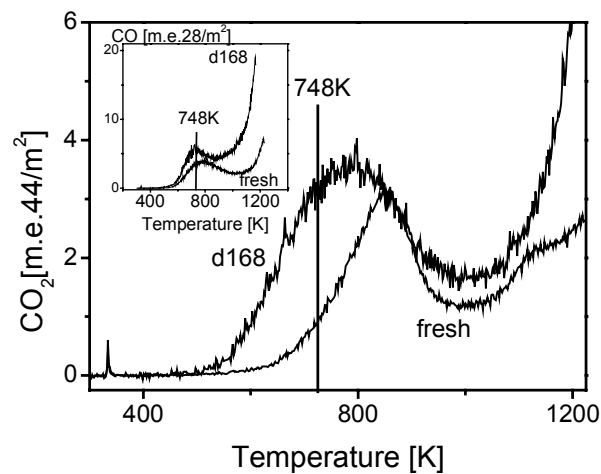


Abb. 60: TDS spectra of CO₂ desorption after O₂ 748 K treatment of the *starting* and d168 samples.

The sample d168 showed a larger desorption of CO₂ than of the *starting* sample, starting at 505 K with one broad desorption maximum at 786 K. In case of the *starting* sample, the CO₂ desorption started at a higher temperature of 600 K with a less broad maximum at 851 K. For both samples, CO₂ evolution increased for temperatures above 1000 K. The amount of CO₂ evolved from d168 exceeds that of the *starting* sample. The broad CO₂ TDS signal observed for the d168 sample suggests the presence of larger variety surface groups, which give desorbing CO₂. The BET surface area is 11 and 23 m²/gr of the *starting* and d168 samples, respectively. Thus, diffusion limitation due to pores can be ruled out.

The desorption of CO had the same pattern for both samples, with d168 giving a higher CO desorption signal (Abb. 60 inset). The onset and the maximum CO desorption occurred at 530 and 580 K, and at 726 and 777 K, respectively for the d168 and *starting* samples.

7.2.3 Catalytic activity in the partial oxidation of methanol

To determine the effect of the reaction parameters temperature and flow of O₂ in the feed (related to the MeOH:O₂ ratio) RSM was conducted for all the samples: e.g. *starting*, d72, d168, and h168. Tab. 15, showing the selected experiments, also lists the H₂CO yield at steady-state conditions for all samples.

Tab. 15: List of experiments conducted for the RSM studies with the *starting* AF-s, and the mechanically activated samples d72, d168, and h168.

Exp. Nr.	Reaction parameters		Yield CH ₂ O (%)			
	Temperature [K]	Flow O ₂ [ml/min]	<i>starting</i>	d72	d168	h168
1	745	2	9.5	4.8	3.1	12.9
2	748	3	12.7	6.5	4.2	16.8
3	748	4	15.2	7.6	5.0	20.3
4	748	3	12.7	6.5	4.2	16.7
5	724	3	9.3	4.7	3.0	12.4
6	724	4	10.8	5.4	3.6	14.5
7	724	6	13.5	6.8	4.4	18.0
8	722	2	9.5	4.8	3.1	12.7
9	698	5	8.1	4.1	2.7	10.8
10	697	3	6.6	3.3	2.2	8.8
11	674	4	4.5	2.6	1.5	6.0
12	673	6	5.4	2.7	1.7	7.1
13	674	2	3.6	1.8	1.2	4.8
14	674	4	4.5	2.3	1.5	5.6
15	651	3	2.1	1.6	0.7	2.8

16	650	5	2.7	1.4	0.9	3.5
17	622	6	1.2	0.6	0.4	1.6
18	620	2	0.9	0.4	0.3	1.1
19	598	3	0.4	0.2	0.1	0.6
20	597	5	1.0	0.3	0.3	0.9

7.2.3.1 H168

The RSM model was calculated for the h168 sample with an interaction model described in the appendix and in the literature [14]. The estimated coefficients with their standard deviations are given in Tab. 16. The complete model has a $F_{7,12}$ (7 dg due to 8-1 coefficients terms and 12 due to 19 total dg - 7) and R^2 value of 133.06 and 98.11%, respectively. From the t-tests of the estimated coefficients (b_i), it can be concluded that some coefficients are statistically significant with a 99% level of confidence, marked by † in Tab. 16.

Tab. 16: List of coefficient for the different models calculated for the yield of CH_2O with the standard deviation of each coefficient. The sign † denotes coefficients, which are statistically significant after conducting the t-test with a confidence level of 99%.

Coefficient	Responses $Y\{\text{CH}_2\text{O}\}$ [%]			
	<i>starting</i>	d72	d168	h168
b_0	4.52† (0.46)	2.28† (0.23)	1.48† (0.15)	5.91† (0.61)
b_1	7.26† (0.56)	3.66† (0.28)	2.38† (0.18)	9.74† (0.74)
b_2	-0.00 (0.51)	0.00 (0.25)	0.00 (0.16)	-0.01 (0.67)
b_3	3.05† (0.64)	1.51† (0.32)	0.98† (0.21)	4.04† (0.84)
b_4	0.38 (0.59)	0.17 (0.29)	0.11 (0.19)	0.65 (0.78)
b_5	1.80† (0.58)	0.88† (0.29)	0.57† (0.19)	2.42† (0.77)
b_6	2.86† (1.07)	1.42† (0.53)	0.92† (0.34)	3.84† (1.41)
b_7	0.08 (0.96)	0.01 (0.48)	0.01 (0.31)	0.09 (1.27)

The elimination of the statistically non significant terms in the model gives a better final $F_{4,15}$ dg due to 5-1 coefficient terms, and 15 dg to 19 total dg - 4) and R^2 value of 290.30 and 98.30%, respectively (Tab. 17). The tabulated $F_{99,9\%,4,15}=8.25$ is much lower than the calculated F-test. It can be concluded that the model accounts for the experimental data with a level of significance of the 99.9%. The final model, plotted in Abb. 61, shows the $Y_{\text{CH}_2\text{O}}$ yield contour surface and has the following form:

$$Y\{\text{CH}_2\text{O}_{_h168}\} = 5.91 + 9.74x_1 + 4.04x_1^2 + 2.42x_1 \cdot x_2 + 3.84x_1^2 \cdot x_2 \quad (\text{eq. 12})$$

Tab. 17: ANOVA Table for the model $Y_{\text{CH}_2\text{O}}$ (%) for the studied samples h168, *starting*, d72, and d168, showing the explained sum of squares by the model, the residual sum of squares, and the total sum of squares. The calculated F- and R^2 -value are also shown. ° Model corrections: terms O_2 , O_2^2 , and $\text{T} \times \text{O}_2^2$ were omitted.

		h168		<i>starting</i>		d72		d168	
Source	d.f.	SS	MS	SS	MS	SS	MS	SS	MS
Due to regression	7	750.0	107.1	419.1	59.9	106.1	15.2	44.8	6.4
Residual	12	9.7	0.8	5.5	0.5	1.4	0.1	0.6	0.04
Total	19	764.5	40.2	427.7	22.5	108.3	5.7	46.0	2.4
F-test_{7,12}			133.1		130.3		133.2		128.7
R^2			0.981		0.979		0.980		0.974
Model corrected °									
Due to regression	4	751.4	187.9	418.5	104.6	106.7	26.7	45.0	11.3
Residual	15	9.7	0.6	5.2	0.3	1.3	0.1	0.6	0.03
Total	19	764.5	40.2	427.7	22.5	108.3	5.7	46.0	2.4
F-test_{7,12}			290.3		299.3		313.2		302.2
R^2			0.983		0.978		0.985		0.979

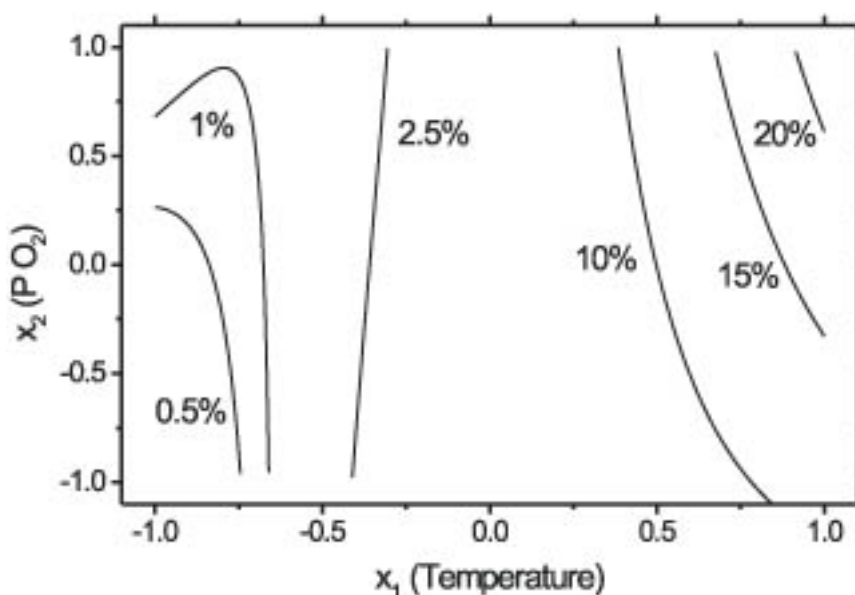


Abb. 61: CH_2O response surface calculated for the sample h168.

From Abb. 61, it is clear that both factors, temperature and the flow of O_2 in the feed have an effect on the yield. Increasing temperatures and O_2 flows significantly increase the yield of CH_2O . This effect is more significant when the temperature and the flow of O_2 get their highest values indicating the positive interaction between these two reaction parameters.

7.2.3.2 Graphite starting

The CH₂O yield surface for the *starting* material is shown in Abb. 62. Tab. 16 lists the calculated coefficients and the statistically significant terms with a level of confidence of 99% and Tab. 17 shows the ANOVA tests. The whole model has a $F_{7,12}$ and R^2 value of 130.3 and 97.9%, respectively. From Tab. 16, some terms in the model were excluded as being statistically non significant and the new ANOVA test gave a $F_{4,14}$ and R^2 value of 299.9 and 97.8%, respectively. The final equation for the CH₂O yield takes the following form:

$$Y\{CH_2O_AFS\} = 4.52 + 7.26x_1 + 3.05x_1^2 + 1.81x_1 \cdot x_2 + 2.87x_1^2 \cdot x_2 \quad (\text{eq.13}).$$

A behavior was found for this sample similar to h168, but with one difference: this sample was less active for the production of CH₂O. As before, the highest yield of CH₂O was achieved working at the highest temperature and O₂ flows, indicating that the samples *starting* and h168 behave similarly.

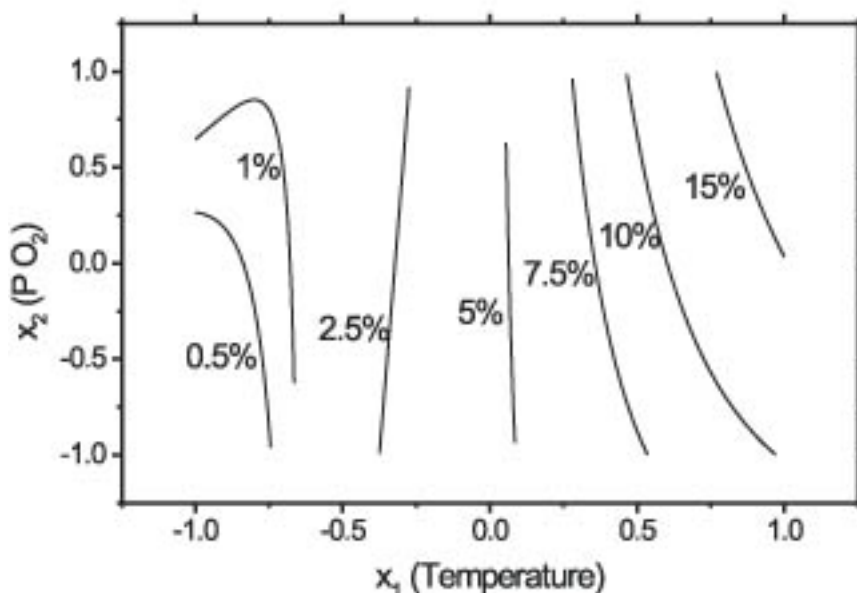


Abb. 62: CH₂O response surface for the *starting* sample.

7.2.3.3 d72 and d168

The results of the estimated parameters for the samples d72 and d168 and the significance of the estimated parameters are presented in Tab. 16. Tab. 17 shows the ANOVA tests for the whole and corrected models. The corrected models have an R^2 value of 98.5 and 97.9% for the d72 and d168 samples, respectively. The response surfaces, shown in Abb. 63 and 64, that build the CH₂O response for the d72 and d168 are listed below with all coefficients being statistically significant 99%:

$$Y\{CH_2O_d72\} = 2.28 + 3.66x_1 + 1.51x_1^2 + 0.87x_1 \cdot x_2 + 1.42x_1^2 \cdot x_2 \text{ (eq.14), and}$$

$$Y\{CH_2O_d168\} = 1.78 + 2.38 \cdot x_1 + 0.98x_1^2 + 0.57x_1x_2 + 0.92x_1^2x_2 \text{ (eq.15).}$$

Comparing the results plotted in Abb. 63 and 64 with the RSM models, it is clear that these two samples behave similar than the *starting* and h168 samples but with one difference: these samples d72 and d18 produce significantly less amounts of CH₂O compared to the other two.

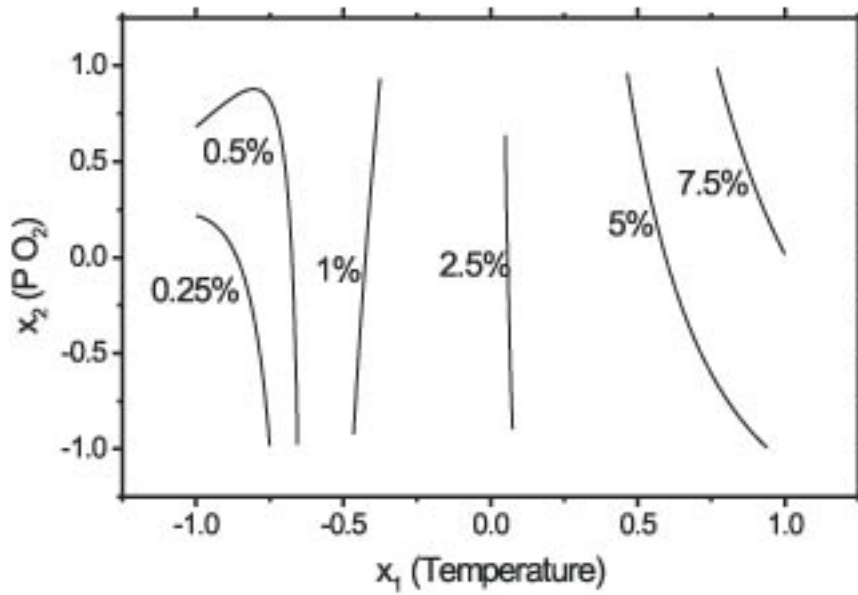


Abb. 63: CH₂O response surface calculated for the sample d72

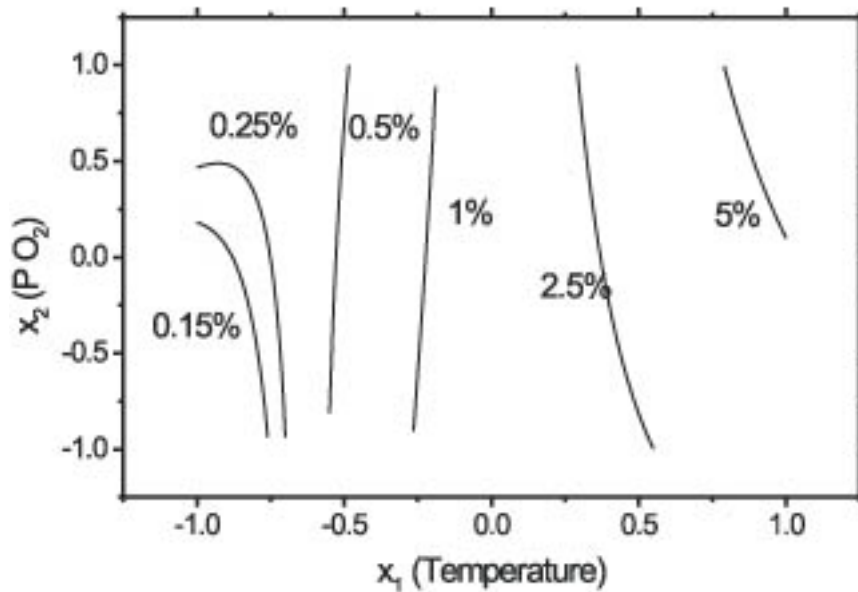


Abb. 64: CH₂O response surface calculated for the sample d168.

Abb. 65 shows the effect of the temperature for all studied samples when the MeOH:O₂ ratio was kept constant at 2.67. Clearly, milling in the absence of hexane decreases the yield of CH₂O. The yields are almost zero at temperatures around 598 K, but as the temperature is increased, the crystalline h168 and *starting* samples produce more CH₂O than the amorphous samples.

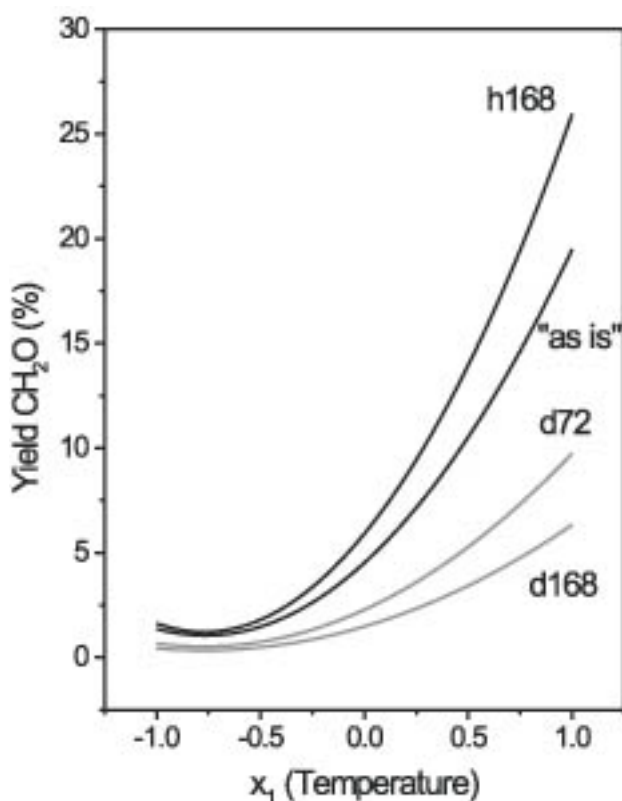


Abb. 65: Effect of increasing temperature on the CH₂O yield. Progressive milling in the absence of hexane leads to a decrease of activity.

7.2.3.4 Comparison of the catalysts

To compare different catalysts conversion-selectivity plots are used. Abb.66 shows the conversion of MeOH vs. selectivity for the *starting*, h168, and d72 samples. The data points show inverse, linear dependency of the selectivity to CH₂O on increasing conversion. Because all samples follow the same trend, the mechanism of the oxidation of MeOH over these samples is identical. The highest conversion is achieved with the h168 sample at 748 K with a selectivity of 50%. The maximum MeOH conversion over the other two samples achieved also at 748 K are marked by arrows in Abb. 66 with higher selectivities to CH₂O.

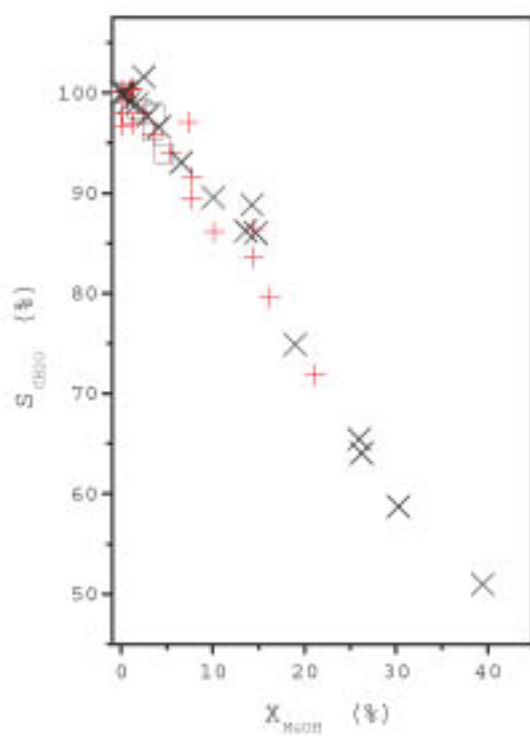


Abb. 66: CH_2O -selectivity vs. MeOH-conversion for the (+) starting, (x) h168, and (box) d72 samples

8 Conclusions

8.1 Structural changes upon milling

Mechanical milling led to the transformation from crystalline into amorphous graphite. The reduction of the crystallite size with increasing milling time was evidenced with XRD and Raman analysis, as well as with SEM and HR-TEM investigations. A clear effect of the presence of hexane on the final microstructure was found.

Milling in the absence of hexane led to an initial increase of the BET surface area, which decreased with progressive milling. This is in agreement with previous results [29] and with other systems like iron [57] and molybdenum oxides [46]. This behavior might be explained by sintering from a recombination of defects and dangling bonds. On the other hand, milling in the presence of hexane resulted in a continuous increase of the surface area. The presence of hexane increased the lubrication properties of graphite and modified its behavior in the ball milling chamber.

The SEM micrographs showed that both the *starting* and the h168 samples have a similar flake-like morphology, but the h168 sample has thinner particles. On the other hand, spherical amorphous-like particles were found in the d168 sample. The remarked amorphization for the dry series was also shown with HR-TEM and ED. The graphite flakes are mostly broken and distorted and a abundant presence of defects can be evidenced. The regions, where still an ordered stacking of the graphene planes exists, have been dramatically reduced. Furthermore, the ED patterns show broad rings for the 100 and 110 reflections confirming the extensive loss of long range order. On the other hand, large crystals are still found in the h168 sample. The ED patterns suggest the possibility that these particles must be crystalline and thin, in agreement with the before discussed results.

Milling in the absence of hexane resulted in a more pronounced broadening of the X-ray reflections concomitant with an increasing asymmetry of the reflections 002, 100 and 110 compared to milling in the presence of hexane. The broadening of the reflections is attributed to the loss of long range periodicity of the material upon milling in form of the decrease of the crystallite size and lattice distortions.

Statistical analysis (ANOVA) conducted with the evolution of the 002 and 110 crystallite sizes upon milling showed that, milling in absence of hexane resulted in a decrease of the [002] and [110] directions. Again, milling in presence of hexane resulted in a lower decrease of the [002] direction, while the [110] direction was not so much affected compared to milling in absence of hexane. The presence of hexane protects the crystallinity in the [hk0] directions.

The 002 reflection showed both an asymmetry as well as a significant shift to higher d-spacing values upon milling, explained by the turbostratic disorder of the graphite sheets. The weak forces between graphite sheets are responsible for the existence of crystallites with higher d-spacing values than the perfect graphite structure. The rotation along the a-axis of adjacent graphite sheets explains this asymmetry. The rotation along the c-axis is not clear if it may cause a bond weakening of adjacent graphite sheets.

The 110 reflection showed an asymmetry, but to lower d-spacing values upon milling especially for the dry series. The qualitative rotation models explained both the asymmetry and the shift to lower

d-spacing values. The rotation along the c-axis and a-axis creates interferences, known as Moiré patterns [78], which are responsible for the appearance of higher hk0 reflections resulting in both a shift and the asymmetry.

Milling also causes the transformation from hexagonal into rhombohedral graphite [4,7] caused by the weak forces between graphite sheets. This transformation occurs both in presence and in absence of hexane and has no effect in the 002 or 110 asymmetries.

Statistical analysis of both XRD and Raman spectroscopy showed that the Raman allowed band at 1580 cm^{-1} correlates with perfect graphite and the two Raman-forbidden bands located at 1333 cm^{-1} and 1620 cm^{-1} correlate with the decrease of the XRD coherence lengths. These two bands increased upon milling especially for the dry series in agreement with previous results [53]. The band at 1333 cm^{-1} is associated with the decrease of the crystallite size in the [110] direction and the band at 1620 cm^{-1} with the [-110] direction from the phonon dispersion curves, respectively. The explanation of the *simultaneous* appearance of the two Raman-forbidden bands for disordered graphite is every disruption (cut) of the graphene layer influences *simultaneously* both [110] and [-110] directions, therefore the Raman forbidden bands *simultaneously* appear. Hence, it is concluded that the relaxation of the k-selection rule due to the decrease of long order periodicity is responsible for their *simultaneous* appearance. These bands arise from nanocrystalline graphite and do not represent a new form of carbon. In contrast to the popular designation "disorder lines", these bands indicate the presence of small but well-ordered graphite particles.

The study of the surface electronic structure by XPS, UPS, and EELS showed no significant changes in the electronic structure of carbon upon milling. These results show that milling affects the long order periodicity of the crystal, but the local/atomic graphite structure is widely unaffected.

8.2 Reactivity Changes upon milling

8.2.1 Carbon combustion

All these structural changes should be related to changes in the reactivity towards combustion. The DTA-TG results indicate that the milled samples became more reactive towards the attack of oxygen compared to the *starting* material. The on-set temperature for the combustion shifted to lower temperatures as the milling progressed. The increase of BET upon milling is partly responsible for this shift to lower temperatures due to more area accessible to oxygen. However, milling in the absence of hexane shifted the on-set temperature to lower temperatures than in the presence of hexane although the BET surface area even decreased from 72 to 168 hours milling. This enhanced shift to lower on-set temperatures for the milled samples in the absence of hexane must be attributed to the observed increase of defective structures and not only to the increase of the BET specific surface area.

The loss of crystallinity increased the onset temperature and the reactivities specially for the samples milled in absence of hexane. But if the data are normalized to the starting surface area, the *starting* graphite is the most reactive sample per square meter, see Abb. 67.

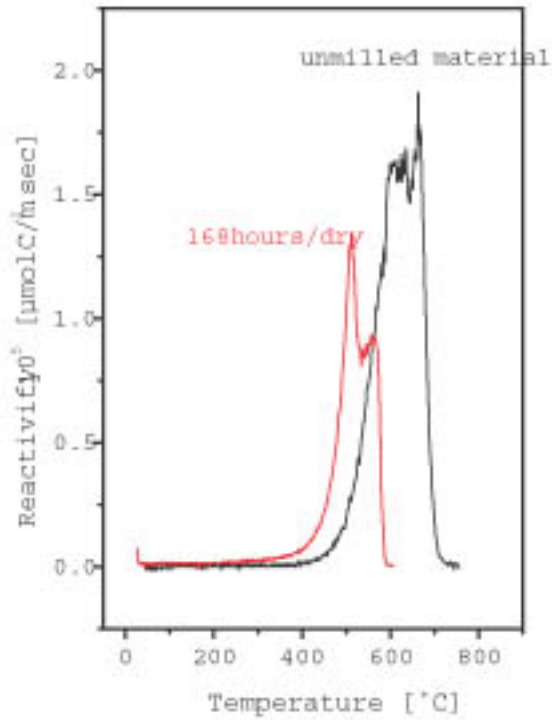
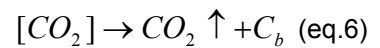
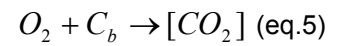
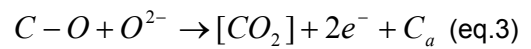
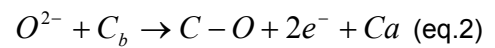
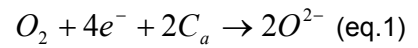


Abb. 67: Comparison of the combustion reactivity for the starting and d168 sample normalized to the surface area.

The reason for this effect is explained by the different rates of the rate-determining step. The model for the carbon combustion consists in the following steps:



With a graphite surface the rate determining step is the reaction of the activated oxygen species with the reaction site C_b (a defect or prism) to form a covalent bond with the carbon substrate, equation 2, in absence of diffusing limiting conditions. A crystalline sample has many C_a reaction sites, basal planes with delocalized π -e⁻, where O_2 is first activated, but fewer C_b reaction sites. On the other hand, with a distorted carbon structure, the density of defects, C_b , is much higher than the C_a reaction sites. This makes the activation of oxygen the rate limiting step, equation 1. As was

demonstrated before milling in absence of hexane decreases the amount of C_a (*BASAL PLANES*) and increases the number of C_b (*DEFECTS*) reaction sites. This decreases the reactivity of the combustion normalized to the starting surface area. However, care must be taken with the interpretation. The normalization of the reactivity to the surface area implies one error, because the surface area changes upon combustion. Nevertheless, this analysis demonstrates that graphite is the most reactive sample, when its combustion reactivity is normalized to the area accessible to O_2 attack.

Furthermore, the form of the DTG profiles are influenced by the milling time and the experimental conditions. Whereas two distinct weight losses are detectable for the d72 and d168 samples, only one peak was observed for the h72 and h168 samples. These combustion peaks are associated with different carbon structures, which react differently. The combustion peak detected in the milled samples in the presence of hexane, the *starting* material, and the second peak in the milled samples in the absence of hexane has an E_a value of 180-190 kJ/mol. On the other hand, the E_a value of the first combustion peak of the milled samples in the absence of hexane is 160 kJ/mol.

This indicates the difference in reactivities motivated by the different structures present upon milling and the influence of the experimental milling conditions. While milling in presence of hexane created a higher surface graphitic material, milling in absence of hexane resulted in a material which outer morphology is almost amorphous. This outer layer reacts with oxygen at much lower temperatures and has a lower E_a . The two different E_a values obtained indicate that the combustion for the *starting* material, the milled samples in the presence of hexane, and the second combustion peak of the milled samples in the absence of hexane is governed by the activation of oxygen on the basal planes. The second peak detected in the milled samples in the absence of hexane is explained by the presence of small graphite crystallites. The lower E_a value detected for the first peak suggests that the mechanism is governed by the gasification regime of electron-rich sites defects. These structures are shown in the previous characterization chapters. First, these distorted structures react with O_2 and until they are depleted the above mechanism is taking place with an E_a value of 160 kJ/mol. Afterwards, the remaining structure is crystalline and its combustion mechanism follows the same pattern as the *starting* material and the milled samples in the presence of hexane.

8.2.2 Methanol oxidation

The activity measurements showed that the milled samples in the absence of hexane were less active than the *starting* sample. Therefore, the transition from C_a sites into C_b sites has a negative effect on the partial oxidation of methanol. This finding is in contradiction with the general thought that a defect site is always more reactive. Strongly covalently bounded O species on C_b sites such as OH, carbonyl, ether, and others [CO_x] cannot react with MeOH. The analysis of the gases evolved with TDS showed that d168 had a greater amount of oxygen groups [CO_x] than the *starting* sample, which was in agreement with the XPS analysis. On the other hand, the *starting* sample, when treated in O_2 at reaction conditions desorbed a lesser amount of CO_x groups. These results further show that strongly covalently bound oxygen groups are not correlated with the activity found. Furthermore, the milled samples in the absence of hexane presented significant weight losses after steady state measurements and the analysis of these samples after reaction showed that notable amounts of amorphous parts burned-off due to the combustion with the reactant O_2 . These results also shows that C_b sites (*DEFECTS*): a) form a large variety of CO_x groups (shown with TDS), b) are not able to participate in the oxidation of MeOH, and c) desorb in form of CO_2/CO (weight losses).

Recently, Nisha et al. [51] reported the adsorption of ethanol on carbon nanohorns (multi-wall nanotubes). After adsorption a heat ramp experiment showed the production of acetaldehyde, but it was not clear from the experiment whether this was a catalytic reaction or a stoichiometric reaction between the adsorbed ethanol and O_2 . If well crystalline graphene planes with a metallic character

catalyze the oxidation of MeOH, they might as well catalyze the oxidation of long-chain alcohols.

The technological importance of finding good catalysts for the oxidation of long-chain alcohols makes necessary a deep study on the possibility of using carbonaceous materials as possible oxidation catalysts.

9 Appendix

9.1 Appendix A: Experimental apparatus

- Mechanical milling

The mechanical activation was conducted in a Retsch centrifugal ball mill S2. The crucible and the balls were composed of agate (diameter of 10 mm). The ratio sample to ball weight was 1:4 and the filling volume around 70%. The acceleration employed for all the experiments was 50 kg/ms².

- BET

The specific surface area measurements were done with the three points BET method using a Quantasorb Jr apparatus with N₂ adsorption at 77 K.

- X-ray diffraction

The x-ray diffraction analysis was conducted with a STOE STADI-P diffractometer in Debye-Scherrer geometry using CuK α radiation. Depending on the symmetry of the reflections profile, the symmetric Voigt or the asymmetric Split-Pearson VII function was used.

- Theoretical modeling of XRD

Different structural models were simulated and their respective x-ray diffractograms to determine the origin of selected asymmetries in the 002 and 110 reflections. The computer calculations were performed using the crystallographic applications of Cerius2 (Molecular Simulations, Inc.).

- Scanning electron microscopy

SEM micrographs were performed on a HITACHI 4000 microscope equipped with an EDAX DX-4 analysis system.

- High-resolution TEM

The High-Resolution TEM was conducted on a Phillips CM 200 FEG TEM with an electron beam of 200 kV energy.

- Raman spectroscopy

Raman experiments were recorded on an DILOR LABRAM spectrometer with an attached confocal microscope equipped with a computerised XY-table. The entrance slits were usually set to 200 μ m. The spectrometer resolution is 2 cm⁻¹. A notch filter was applied to filter out the laser line and the Rayleigh scattering up to \sim 150 cm⁻¹. The spectrometer is equipped with a CCD camera (1024 \times 298 diodes), which is peltier-cooled to 243 K reducing thermal noise. A He-laser (632.8 nm, Melles Griot) was used for excitation of the Raman spectra. The laser power was controlled from 0.14 to 14 mW using neutral-density filters. The light was focused on the sample using a microscope lens. Raman spectra were recorded in backscattering geometry on a line of about 40 mm length on the sample surface using the scanning multichannel technique.

- X-ray photoelectron spectroscopy

The XPS measurements were performed with a modified LHS 12 MCD system equipped with facilities for UPS (He I 21.22 eV) and XPS (Mg K α 1253.6 eV, 168 W power). For the XPS measurements a fixed analyser pass energy of 108 eV was used resulting in a resolution of 1.28 eV FWHM of the Ag 3d^{5/2} peak.

- Ultraviolet photoelectron spectroscopy

The UPS spectra were obtained with a fixed pass energy of 12 eV and the measuring chamber had a base pressure of 1 \times 10⁻¹⁰ mbar.

- Energy electron loss spectroscopy

Electron energy loss spectroscopy measurements were conducted with energy of the incident electrons of 500 eV and an energy resolution of 0.5 eV.

- K-edge x-ray absorption spectroscopy

The X-ray absorption spectroscopy experiments were carried out at the beamline HE-TGM1 at the Berliner Synchrotron Radiation source BESSY with an electron beam energy of 0.8 GeV. The measurements were conducted with total electron yield modus at 4.5 V in the soft X-ray range ($250 \text{ eV} \leq h\nu \leq 1000 \text{ eV}$) with a resolution of 1 eV at the C K-Edge.

- Thermogravimetry-TPO

The thermogravimetric oxidation experiments were conducted with a Seiko Instruments SSC5200 thermal analysis system. The sample was placed in an alumina crucible and burned with a continuous flow of 100 ml $\text{N}_2:\text{O}_2=1$ /min. The determination of the apparent E_A for the combustion was conducted with the Kissinger method [34]. The heating rate ϕ was varied between 0.5 and 20 K/min.

- Temperature programmed reaction spectroscopy

A tubular flow reactor (duran glass) was used with an inner diameter of 7.5 mm}. The gases used in the experiments were N_2 (5.0 LINDE AG) saturated with MeOH at room temperature and O_2 (5.0 LINDE AG). A heating rate of 5 K/min and an hourly-space-velocity of $4.6 \times 10^4 \text{ h}^{-1}$ were used in the catalytic runs. The products were monitored using an Ion-Molecule-Reaction-MS apparatus (IMR-MS 1100, ATOMIKA Instruments GmbH) [64].

- Temperature desorption spectroscopy

TDS measurements were performed in an UHV chamber with an average background pressure of 3×10^{-8} mbar. The vacuum was created with a oil-free Balzer's turbopump with a pump rate of 240 L/s. The desorption products were monitored with a Hiden (Hal2) quadropole mass spectrometer. The sample was heated with a water-cooled, infrared oven and the thermocouple was located below the sample and in direct contact with the quartz cell.

9.2 Appendix B: Methodology

In this section, different mathematical methods for statistical evaluation are briefly presented. ANOVA and multiple linear regression belong to classical statistic methods to analyze uni and bivariate data. In addition, more powerful methods for analyzing huge amount of multivariate data such as PCA, PLS, and SIMPLISMA belong to a new class of methods grouped in the field of chemometrics.

9.2.1 Analysis of variance

The studied case is to discern whether the variance of the milling time [A], the experimental conditions [B], and the interaction between these parameters [A×B], is larger than the variation of the experimental error. The responses studied were crystallite size in both the [002], S_{002} , and [110], S_{110} directions. The experiments were repeated to determine the experimental error. The parameters and levels can be found in Tab. \ref{tabanova1}.

The total variation or sum of squares, (SS_{Total}), can be divided into the variation due to parameter A (SS_A), parameter B (SS_B), the interaction A×B ($SS_{A×B}$), and the residual random error (SS_{error}):

$$SS_{TOTAL} = SS_A + SS_B + SS_{A×B} + SS_{error} \quad (\text{eq.16}),$$

where the total sum of squares can be calculated with the values from the experiments with the expression;

$$\begin{aligned} SS_{TOTAL} &= \left[\sum_{i=1}^N y_i^2 \right] - \frac{T^2}{N} = \\ &= 280^2 + 280^2 + 93.3^2 + \dots - \frac{1985.2^2}{12} = 93486.3 \end{aligned} \quad (\text{eq.17}),$$

where y_i is the measured response (Tab. 5) between $i=1, \dots, N=12$ number of experiments, and T is the sum of all measured responses. In this case $T=1985.2$. Additionally, the SS of a determined parameter is calculated with:

$$\begin{aligned} SS_A &= \left[\sum_{i=1}^{k_A} \left(\frac{A_i^2}{nA_i} \right) \right] - \frac{T^2}{N} = \\ &= \frac{A_1^2}{nA_1} + \frac{A_2^2}{nA_2} + \frac{A_3^2}{nA_3} + \dots + \frac{A_k^2}{nA_k} - \frac{T^2}{N} \end{aligned} \quad (\text{eq.18}),$$

where A_1 is the sum of all responses when the parameter A gets the level 1, and k_A is the number

of levels of the parameter A. In this case the parameter A gets three levels, where $A_1 = 1111.2$, $A_2 = 526.5$, and $A_3 = 347.4$. The value n_{A1} is the number of observations conducted with A_1 , in this case $n_{A1} = n_{A2} = n_{A3} = 4$. The Sum of squares for the parameter A and parameter B are then:

$$SS_A = \frac{1111.2^2}{4} + \frac{526.6^2}{4} + \frac{347.4^2}{4} - \frac{1985.2^2}{12} = 79771.7, \text{ and}$$

$$SS_B = \frac{843.2^2}{6} + \frac{1142.0^2}{6} - \frac{1985.2^2}{12} = 7440.1. \text{ (eq.18i)}$$

To calculate the variation of $A \times B$, the data is first organized into all possible parameter combinations. Then, the data are summed for each combination. Let $(AB)_i$ represent the sum of data under the i^{th} condition of the A and B combination. Also, let c represent the number of possible combinations of the interacting parameters and $n(A \times B)$ the number of data points under this condition. Then,

$$SS_{A \times B} = \left[\sum_{i=1}^c \left(\frac{(A \times B)_i^2}{n_{A \times B i}} \right) \right] - \frac{T^2}{N} - SS_A - SS_B \text{ (eq.19).}$$

For the considered experiment;

$$A_1B_1=(A \times B)_1=569.4, A_1B_2=(A \times B)_2=541.8, \dots, \text{ and } A_3B_2=(A \times B)_6=247.4.$$

$$SS_{A \times B} = \frac{569.4^2}{2} + \frac{541.8^2}{2} + \dots + \frac{247.4^2}{2} - \frac{1985.2^2}{12} - 79771.7 - 7440.1 = 6192.6$$

(eq.19i)

Whatever variation is left over corresponds to the residual random error, see equation 16, where:

$$SS_{error} = SS_{TOTAL} - SS_A - SS_B - SS_{A \times B} = 93486.3 - 79771.7 - 7440.1 - 6192.6 = 82.3$$

To complete the ANOVA calculations, another element must be considered, the degrees of freedom, v . In a statistical sense, a v is associated with each piece of information that is estimated from the data.

$$\text{Total } v, v_T = N - 1 = 12 - 1$$

$$\text{Parameter A } v; v_A = k_A - 1 = 3 - 1$$

$$\text{Parameter B } v; v_B = k_B - 1 = 2 - 1$$

$$\text{Interaction (A}\times\text{B) } \nu; \nu_{A\times B} = (\nu_A)(\nu_B) = 2 \times 1$$

After calculating the SS and the number of ν , we have to determine whether the parameters and the interaction are significant or not. There is a statistical tool which provides a decision at a given confidence level, the F-test. This test is named after Sir Ronald Fisher, a British statistician, who invented the ANOVA method. The F-test is simply the ratio of variances:

$$F = \frac{V_1}{V_2} \quad (\text{eq.20})$$

where V_1 is the variance of the parameter A or A{ \times }B and V_2 is the variance of the experimental error. When this ratio becomes large enough, then the two sample variances are accepted as being unequal at some confidence level. To calculate this ratio, three items are necessary: first the level of confidence, second the ν of the numerator, and third the ν of the denominator. The usual format is then $F_{\alpha; \nu_1; \nu_2}$, where α is the risk, $1-\alpha$ is the confidence, and ν_1 are the degrees of freedom for the numerator and ν_2 for the denominator, respectively. The F-ratio compares the variation of each parameter with the variance of the detected error.

9.2.2 Response surface methods

Response surface methods (RSM) play an important role in the field of experimental design [10,36,55] and are based on the least squares estimation. The main features of RSM are:

- The design of a set of experiments which will yield adequate and reliable data on the response of interest, e.g. MeOH conversion, H₂CO yield...
- The determination of a mathematical model, which fits best the collected data of the chosen design, by appropriately testing hypotheses concerning the parameters of the model.
- The determination of the optimum experimental parameters, which result in the maximum (or minimum) of the response.

The response, Y, of any system can empirically be described by a homogeneous equation system in which the factors, X_i , are multiplied by unknown coefficients β .

$$Y = \sum \beta_i X_i + \sum \beta_j X_j^2 + \dots \quad (\text{eq.21})$$

It must be noted that these regression coefficients β , have no physical meaning. The mathematical model is adjusted to the experimental data, response, by optimizing these equations. The response variable is the measured quantity, which is changed by the levels of some factors. In the absence of an experimental error, the true response is denoted η . The measured response, Y, differs from the true response, η , by the experimental error, ε :

$$Y = \eta + \varepsilon \quad (\text{eq.22})$$

The value of the true response, η , depends of the levels ϕ of k quantitative factors: X_1, X_2, \dots, X_k . Therefore, a function exists of X_1, \dots, X_k

$$\eta = \phi(X_1, X_2, \dots, X_k) \quad (\text{eq.23})$$

which gives the value of the true response. ϕ is assumed to be a continuous function of X_i . Considering a continuous function depending only on one factor X_1 , it is possible to represent this function locally, to any required degree of approximation, by a Taylor series expansion about some arbitrary point X_{10} ,

$$\eta = \phi(X_{10}) + \phi'(X_{10})(X_1 - X_{10}) + \frac{1}{2}\phi''(X_{10})(X_1 - X_{10})^2 + \dots \quad (\text{eq.24})$$

where $\phi'(X_{10})$ and $\phi''(X_{10})$ are the first and second derivatives with respect to X_1 evaluated at X_{10} , respectively. The equation 24 can be rewritten as:

$$\eta = \beta_0 + \beta_1 X_1 + \beta_2 X_1^2 + \dots \quad (\text{eq.25})$$

in which the coefficients, β_i , are parameters which depend on X_{10} and the derivatives of ϕX_1 at X_{10} . RSM finds estimates of these parameters, β , by means of the least squares method. Considering a response function, Y with N trials, which is a linear combination of k factors, the model can be written as:

$$Y_u = \beta_0 + \beta_1 X_{u1} + \beta_2 X_{u2} + \dots + \beta_k X_{uk} + \varepsilon_k \quad (\text{eq.26})$$

with $u=1, \dots, N$ Y_u specifying the response for the u^{th} trial, X_{iu} representing the level of factor i for the u^{th} trial, and β_i representing the unknown parameter of the factor i for the u^{th} trial. In multiple regression some assumptions are made about the experimental error, ε_i . It has a zero mean and common variance. The different ε_i are also mutually independent and normally distributed. The least squares selects as estimates for the unknown parameters, β_i , in equation 26, such values which minimize the following expression:

$$R(\beta_0, \beta_1, \dots, \beta_k) = \sum_{u=1}^k Y_u - (\beta_0 + \beta_1 X_{u1} + \beta_2 X_{u2} + \dots + \beta_k X_{uk}) \quad (\text{eq.27})$$

where β_i is the unknown parameter, Y_u is the response at the u^{th} trial, and X_{u1} is the factor 1 at the u^{th} .

In matrix notation the N -equations, equation 26, can be written as,

$$\mathbf{Y} = \boldsymbol{\beta}\mathbf{X} + \boldsymbol{\varepsilon} \quad (\text{eq.28})$$

\mathbf{Y} is the matrix of the responses, Y , with the dimension $(1 \times N)$, \mathbf{X} is the matrix of the factors, X_i , with the dimension $(N \times k+1)$, $\boldsymbol{\beta}$ is the matrix of the estimates, β_i , with the dimension $(k+1 \times 1)$, and $\boldsymbol{\varepsilon}$ is the matrix for the experimental error, ε_i , with the dimension $(N \times 1)$. The solution, \mathbf{b} , of the homogeneous equation system is calculated by matrix operations:

$$\mathbf{b} = \mathbf{X}'\mathbf{X} - \mathbf{X}'\mathbf{Y} \quad (\text{eq.29})$$

It can be demonstrated that the variance-covariance matrix [10,36] is calculated as:

$$\mathbf{Var}(\mathbf{b}) = \mathbf{X}'\mathbf{X} - \mathbf{1}\sigma^2 \quad (\text{eq.30})$$

where σ is the standard error of the estimates, b_i . To check how well the mathematical model fits the observed responses, Y_i , the residuals, r_u , must be taken into account:

$$r_u = Y_u - \hat{Y}(X_u) \quad (\text{eq.31})$$

where $u=1,2,\dots,N$, in which r_u are the individual residuals at the u^{th} trial, and $\hat{Y}(X_u)$ is the response predicted for the model at the u^{th} trial. The analysis of variance (ANOVA-test) [10,36] verifies if the parameters are statistically significant and checks a possible lack-of-fit of the model. This lack-of-fit results from neglecting higher order terms of the factors, interactions between them, or from the existence of external factors, not included in the model which contribute to the variation in the response. In order to calculate the ANOVA test, several expressions must be calculated.

The total variation in the set of a data is called the total sum of squares SS_T :

$$SS_T = \sum_{u=1}^N (Y_u - \bar{Y})^2 \quad (\text{eq.32})$$

in which Y_u is the experimental response at the u^{th} trial and \bar{Y} is the mean of the Y_u responses. The degrees of freedom, ν , associated with SS_T are $N-1$. The SS_T can be divided into: the sum of squares due to regression, SS_R , equation 33 (sum of squares explained by the model) and the sum of squares unaccounted for by the fitted model, SS_E , equation 34. SS_R and SS_E have associated $k-1$ and $n-k$ ν , respectively, where k is the number of parameters and N the number of trials,

$$SS_R = \sum_{u=1}^N (\hat{Y}(x_u) - \bar{Y})^2 \quad (\text{eq.33}), \text{ and}$$

$$SS_E = \sum_{u=1}^N (Y_u - \hat{Y})^2 \quad (\text{eq.34}).$$

The usual test of significance is a zero-Hypothesis test H_0 : all values excluding β_0 are zero. This test involves the calculation of the value of the F-statistics [36].

$$F = \frac{\text{Meansquare regression}}{\text{Meansquare residual}} = \frac{\frac{SS_R}{k-1}}{\frac{SS_E}{N-k}} \quad (\text{eq.35})$$

After calculating the F-test, this value must be compared with the tabulated data [10,36], $F_{\alpha,k-1,N-p}$. This tabulated data, $F_{\alpha,k-1,N-p}$, is the upper 100 α percent point of the F distribution with $k-1$ and $n-p$, respectively. If the F-value calculated in equation 35 exceeds $F_{\alpha,k-1,N-p}$, then the zero-hypothesis is rejected at the α level of significance. In other words, the variation accounted for by the model is significantly greater than the unexplained variation. The measurement of the proportion of total variation of the values of Y_u about the mean, \bar{Y} , explained by the model is given by the R^2 value.

$$R^2 = \frac{SS_R}{SS_T} \quad (\text{eq.36})$$

The acceptance or rejection of the zero-hypothesis, H_0 , declares that a fitted model, with all estimated $b_i \neq 0$, accounts for the observed variance or not within a significance level. If the estimated parameters $b_i \neq 0$ are statistically significant is determined by t-tests. A t-test is performed by comparing the parameter estimates, b_i , in the fitted model to their respective estimated standard errors and conducting a test of zero-hypothesis, H_0 , $\beta_i = 0$,

$$t = \frac{b_i}{\text{est.s.e.}(b_i)} \quad (\text{eq.37})$$

Subsequently, the calculated t-value is compared with a tabulated value, $t(\alpha)$ [10,36]. After determining all the significant factors, the last test to conduct is the lack-of-fit test. This test takes into account the residual sum of squares, SS_E . SS_E , can be partitioned into two sources of variation; the variation among replicates, SS_{PE} , and the variation arising from the lack-of-fit of the fitted model, SS_{LOF} :

$$SS_E = SS_{PE} + SS_{LOF} \quad (\text{eq.38})$$

The sum of squares due to lack-of-fit is found by subtraction from eq. 38, and the variation among replicates is defined as:

$$SSPE = \sum_{l=1}^n \sum_{u=1}^{r_l} (Y_{ul} - \bar{Y}_l)^2 \quad (\text{eq.39})$$

where Y_{ul} is the u^{th} observation of the response at a determined design point l^{th} , where $u=1,2,\dots,r_l \geq 1$, and $l=1,2,\dots,n$. \bar{Y}_l is defined as the average of the r_l observations at the l^{th} design point. The test of the null hypothesis of adequacy of fit (or lack of fit is zero) involves calculating the value of the F-ratio

$$F = \frac{\frac{SS_{LOF}}{n-p}}{\frac{SS_{PE}}{N-n}} \quad (\text{eq. 40})$$

this F-value is compared with the tabulated ones. Lack-of-fit is assumed at the a level of significance if the calculated F-value in equation 40, exceeds the tabulated one. If lack-of-fit is not rejected, new terms must be added to the model. On the other hand, if the zero-hypothesis is not rejected, then there is no reason to doubt the adequacy of the fitted model. A quadratic model was chosen to fit the formaldehyde yield. Two reaction parameters the temperature, X_1 , and the flow of O_2 , X_2 , were studied. To simplify the calculations, the variables X_i are coded in the following way:

$$xi = 2 \frac{(X_i - X_{i0})}{(X_{i-1} - X_{i+1})} \quad (\text{eq.41})$$

With this substitution, the proposed empirical model for the response Y has the following form:

$$Y = b_0 + b_1x_1 + b_2x_2 + b_3x_1^2 + b_4x_2^2 + b_5x_1x_2 \quad (\text{eq.42})$$

The analysis of the data showed that this polynomial model was not suited to fit the experimental data. An interaction model [14] was therefore chosen to fit the response. This interaction model has two additional terms added to the model shown in 42 and has the following form:

$$Y = b_0 + b_1x_1 + b_2x_2 + b_3x_1^2 + b_4x_2^2 + b_5x_1x_2 + b_6x_1^2x_2 + b_7x_1x_2^2 \quad (\text{eq.43})$$

9.2.3 Principal component analysis

Principal component analysis (PCA) [28,55,8] finds applications in diverse fields such as: analytical chemistry [13,24], image processing data analysis in astronomy [30], and in molecular biology [79]. Algorithms such as PCA are designed to reduce large complex data sets into a series of optimized and interpretable. views. PCA analyzes natural groupings in the data set and shows which variables most strongly influence these relations. The starting point of a PCA analysis is the data matrix, \mathbf{X} , with $\{n \times m\}$ dimensions, n objects or samples and m variables. The columns represent the measured variables and the rows the objects or samples. The data matrix \mathbf{X} can be decomposed into a scores \mathbf{T} and loading \mathbf{P} matrix where \mathbf{E} is the residual matrix, as shown in Abb. 68.

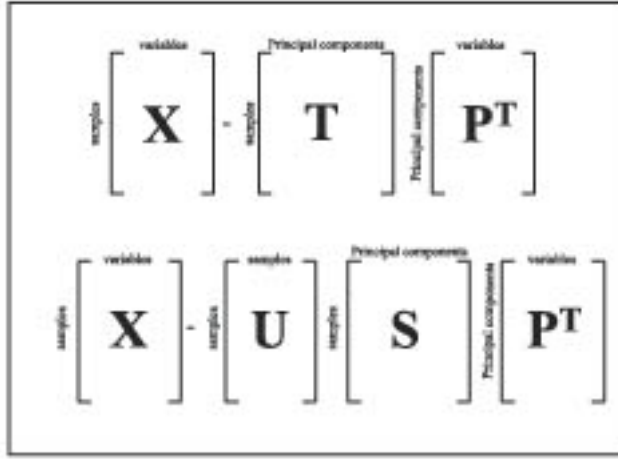


Abb. 68: Decomposition of the data matrix \mathbf{X} into the scores, \mathbf{T} , (eigenvalues) and loadings, \mathbf{P} , (eigenvectors) matrices (top) and decomposition using the SVD algorithm (bottom).

The loading vectors \mathbf{p}_i are the eigenvectors of the covariance matrix $\mathbf{X}^T\mathbf{X}$, and the score vectors \mathbf{t}_i are its corresponding eigenvalues. This decomposition of the data matrix converts \mathbf{X} into a few informative plots (score and loading plots) and models the systematic structure in \mathbf{X} . PCA attempts to combine those variables that are highly correlated into a new variable called a PC. The PCA calculation was conducted using the single-value-decomposition (SVD) [28,55,8] algorithm with the mathematical functions included in MATLAB 5.0. The SVD algorithm, used to calculate the principal components, decomposes the data matrix \mathbf{X} into the product of three matrices with $\mathbf{US}=\mathbf{T}$, as shown in Abb. 68 (bottom).

Prior to the PCA analysis, the data matrix \mathbf{X} first must be mean-centered. As the analysis of the PCA depends on the way the data are autoscaled, the formula used for the mean-centering is presented in the following equations:

$$x_{ik} = d_{ik} - \bar{d}_k \quad (\text{eq.44}) \text{ and}$$

$$\bar{d}_k = \frac{1}{n} \sum_{i=1}^n d_{ik} \quad (\text{eq.45}),$$

where d_{ik} is the measured value of the i^{th} sample row and k^{th} measured variable, \bar{d}_k is the mean, and n is the number of samples or objects.

Once all the PC's of the data matrix have been calculated, the maximum number of PC's of a matrix equals the rank of the matrix $R = n^\circ$ variables m , the determination of significant PC is conducted. The first component is chosen to have the largest possible variance. To determine how much of the data variance is explained by the PC's \mathbf{S} is squared. \mathbf{S} is a diagonal matrix which contains the singular values of each PC. Its square gives the variances of each PC or the eigenvalues, λ_i . The explained variance is calculated by the expression:

$$\text{ExplainedVariance} = \frac{\lambda_i}{\sum \lambda_i} \quad (\text{eq.46})$$

The explained variance or its logarithm is plotted versus the number of calculated PCs. Some

authors recommend to find a doglet or a large drop in the eigenvalues in this plot to decide how many PC are significant. With the expression in equation 46, knowledge about the importance of each PC can be obtained, and subsequently the important information can be gathered in form of score and loading vectors. For example, considering a set of data with three variables as shown in Abb. 69 (left).

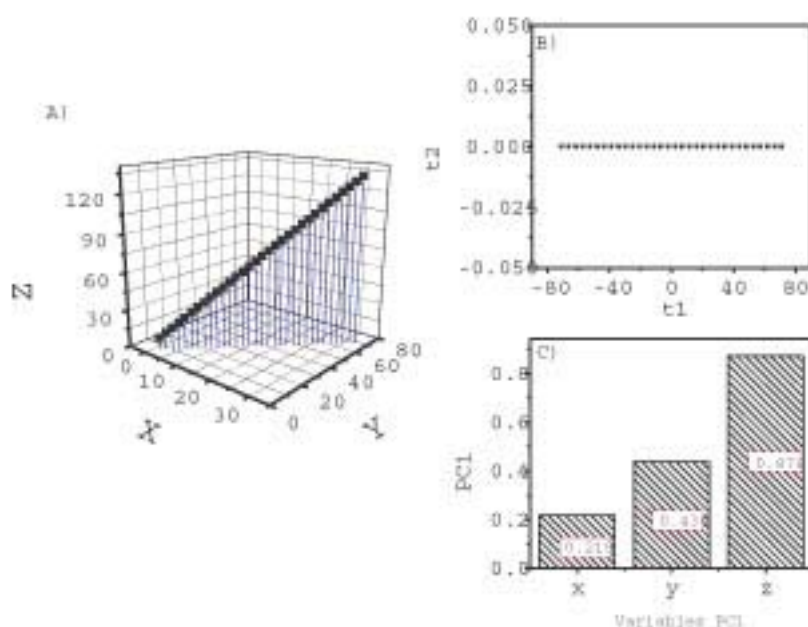


Abb. 69: Example of PCA analysis. A) 3-D plot of generated data with $y=5+2x$ and $z=y+2x$. B) Score plot t_1 vs. t_2 . C) Loading plot of the first principal component.

The data were generated by the following formulas $y=5+2x$ and $z=y+2x$. The set of data expand in a line in the 3D-space. The score plot shows the position of the data after conducting PCA, see Abb. 69 (right top). The data fall in a line due to the rotation of the axes, x , y , and z . The rotation matrix or loading matrix is presented for the PC1 in Abb. 69 (right bottom). The most important variable is z (largest loading value). The PCA analysis of this set of data shows that only one PC explains 100 % of the variance of the data, see Tab. 18.

Tab. 18: Results of Principal component analysis with data generated as $y=5+2x$ and $z=y+2x$.

No. of principal component	Eigenvalue	Variance explained (%)	Total variance explained (%)
PC1	1.0175×10^4	100	100
PC2	0	0	
PC3			
Parameters	PC1	PC2	PC3
x	0.2182	-0.9759	0

y	0.4364	0.0976	0.8944
z	0.8729	0.1952	-0.4472

The other two PC's are considered to be noise or error. The first component states that, p_1 is a linear combination of the old axes, specifically of $p_1 = 0.2182x + 0.4364y + 0.8729z$. Notice that $0.4364/0.2182 = 1.995$ and $0.8729/0.2182 = 3.98$. This implies that the z axis, y axis and x axis are used in a ratio 4:2:1} to generate the new PC1, which exactly coincides how the data were generated. In this simple example of PCA, the data dimension was reduced from 3D to a line due to the structure of the data.

9.2.4 Partial-least-squares

It is important to develop relationships between the reactivity of a catalyst and its structural properties. For this purpose a physicochemical variable measured by one characterization technique, is plotted versus activity or selectivity. The same approach can be used when relationships have to be developed between results of two different characterization techniques. Another way to obtain information on functional relationships between data sets is to build empirical models by RSM [10,36]. The underlying assumptions for the use of MLR are not longer valid when linear combinations of variables are included in the model [10,20]. In the respect of large spectral data sets, other statistical techniques are more suited to build structure-activity models. One of the best suited techniques to solve the collinearity problem arises from partial least-squares projections to latent structures (PLS) [20]. A Quantitative-Structure-Activity-Relationship QSAR model relates the structure descriptor, \mathbf{X} , with the activity descriptor \mathbf{Y} . Structural parameters, physical and chemical properties are included in the \mathbf{X} matrix, with the hope to describe the studied samples. Activity or reactivity measurements are included in the \mathbf{Y} matrix. The power of a PLS analysis arises from its ability to find combinations of the structural descriptors, t_A , which correctly predict the considered response Y_i and approximate the structure descriptor matrix, \mathbf{X} . The first property of PLS is similar to MLR techniques, but with the advantage correlated \mathbf{X} -variables can be used. The \mathbf{X} and \mathbf{Y} descriptors are approximated by a model consisting of scores and loading vectors :

$$\mathbf{X} = \mathbf{TP}' + \mathbf{E} \quad (\text{eq.47}), \text{ and}$$

$$\mathbf{Y} = \mathbf{UQ}' + \mathbf{F} \quad (\text{eq.48})$$

Where \mathbf{T} and \mathbf{P} are the score and loading matrices of \mathbf{X} , and \mathbf{U} and \mathbf{Q} the score and loading matrices of \mathbf{Y} , respectively. The \mathbf{E} and \mathbf{F} matrices are the residuals of \mathbf{X} and \mathbf{Y} , respectively. Both descriptors are related through the following equation

$$\mathbf{U} = \mathbf{TB} + \mathbf{H} \quad (\text{eq.49})$$

where \mathbf{B} is diagonal matrix and equation pls4 gives the predictive formulation of \mathbf{Y} . The PLS regression model may be written as:

$$\mathbf{Y} = \mathbf{XB}_{PLS} + \mathbf{F} \quad (\text{eq.50})$$

which at first sight is not different from what one expects from RSM, except that coefficients are calculated using PLS and the assumptions for PLS are radically different from RSM. In RSM, the variables are assumed to be mathematically independent, and exact. For PLS, this is not necessary because the presence of collinear variables is considered and, realistically, variables may be perturbed by noise. The physicochemical meaning of the PLS model must be tracked to the calculated scores t and u . Both scores contain the information of the experimental observations and their similarities/dissimilarities in X-space and Y-space with respect to the given problem and model. At the same time, the X and Y-loadings, p and q , supply information on the possible combination of variables to form the scores t and u , which express the quantitative relation between \mathbf{X} and \mathbf{Y} .

9.2.5 Simplisma

Simplisma (Simple-to-use interactive self-modeling mixture analysis) [8] is based on a simple algorithm which calculates the minimum number of linearly independent pure spectral components. This statistical tool provides information about the number of peaks, their position, and shapes belonging to the same pure spectral component. The original data matrix $\mathbf{X} = x_{ij}$ with $n \times m$ dimensions, where n is the number of spectra and m is the number of recorded frequency/wavenumber points. The assumption that these spectra are linear superpositions of independent, pure spectral components, leads to the following equation:

$$\mathbf{X}^T = \mathbf{C} \times \mathbf{E} \quad (\text{eq.51})$$

with \mathbf{E} the pure component spectra matrix, and \mathbf{C} the matrix of the weight factors. The matrix can be solved by with the aid of the least squares method giving:

$$\mathbf{E} = (\mathbf{C}^T \times \mathbf{C})^{-1} \mathbf{C}^T \times \mathbf{X}^T \quad (\text{eq.52})$$

The selection of pure components is based upon purity values, p_j ($j=1, \dots, m$),

$$p_j = w_j \frac{\sigma_j}{\mu_j + \alpha} \quad (\text{eq.53})$$

with σ_j being the standard deviation at a given wavenumber j , μ_j being the mean scattered intensity at a given wavenumber j , α being a noise reduction parameter, and w_j a weight factor to correct for previously selected pure variables and for the normalisation applied to the data matrix. The initial value of w_j is one. The standard deviation at a given wavenumber j , σ_j , and the mean scattered intensity at a given wavenumber j , μ_j , are calculated from the following formula:

$$\sigma_j = \sqrt{\frac{\sum (d_{ij} - \mu_j)^2}{n}} \quad (\text{eq.54}), \text{ and}$$

$$\mu_j = \sum \frac{d_{ij}}{n} \quad (\text{eq.55})$$

10 Bibliography

- 1 Al-Jishi R. and Dresselhaus G.: Phys. Rev. 1982, *B26*, p.4514,
- 2 Andrews G.L., Groszek A.J., and Hairs N.: ASLE Transactions. 1972, *15*, p.1984,
- 3 Atamny F., Blöcker, J., Dübotzky, A., Kurt, H., Timpe, O., Loose, G., Mahdi, W. and Schlögl, R.: Molec. Phys.. 1992, *76*, p.851,
- 4 Bacon, G.E.: Acta Cryst.. 1950, *3*, p.320,
- 5 Belz, T., Find, J., Herein, D., Pfänder, N., Rühle, T., Werner, H., Wohlers, M. and Schlögl, R.: Ber. Bunsenges. Phys. Chem.. 1997, *702*, p.101,
- 6 Benjamin, J.S., and Volin, T.E.: Met. Trans.. 1974, *7*, p.1929,
- 7 Boehm, H.-P., and Hofmann, U.: Z. anorg. Allg. Chemie. 1955, *278*, p.58,
- 8 Boldyrev, V. and Meyer, K.: Festkörperchemie- Beiträge aus Forschung und Praxis. vol 1. Leipzig, VEB Deutscher Verlag für Grundstoffindustrie, 1973
- 9 Bowden, F.F. and Tabor, D.: The friction and lubrication of solids. vol 1. 1 Oxford, Oxford, 1958
- 10 Box, P.E., Hunter, W.G. and Hunter, J.S.: Statistics for Experimenters: An introduction to Design, Data Analysis, and Model Building. vol 1. 1 New York, John Wiley & Sons, 1978
- 11 Chen, H.S: Rep. Prog. Phys.. 1980, *43*, p.353,
- 12 Chieu, T.C., Dresselhaus, M.S., and Endo, M.: Phys. Rev.. 1982, *B26*, p.5867,
- 13 Cole, R. and Phelps, K.: J. Sci. Food Agril.. 1979, *30*, p.669,
- 14 Cornell, J.A. and Montgomery, D.C.: J. Quality Tech.. 1996, *28*,
- 15 Cuesta, A., Dhamelincourt, P., Laureyns, J., Martinez-Alonso, A., and Tascon, J.M.D.: Carbon. 1994, *32*, p.1523,
- 16 Dresselhaus, M.S. and Dresselhaus, G.: Adv. Phys.. 1981, *30*, p.139,
- 17 Dresselhaus, M. and Dresselhaus, G.: Topics in Applied Physics: Light Scattering in Solids III. vol Carbon. Frankfurt, Springer Verlag, 1982
- 18 Eklund P.C., Holden J.M., and Al-Jishi R.A.: Carbon. 1995, *33*, p.959,
- 19 Erbil, A., Postman, M., Dresselhaus, G., and Dresselhaus, M.S.: Ext. Abs. And Program, 15th Bienn. Conf. Of Carbon. Ed.: Carbon: vol 1. 1 Pennsylvania, Carbon, 1981
- 20 Eriksson L., Hermens J.L.M., Johansson E., Verhaar H.J.M., and Wold S.: Aquatic. Sci.. 1995, *57*, p.3,
- 21 Everall, N.J., Lumsdon, J., and Christopher, D.J.: Carbon. 1991, *29*, p.133,
- 22 Fink, M.: Trans. Am. Soc. f. Steel Treating. 1986, *24*, p.365,
- 23 Fishbach, D.B. and Couzi, M.: Carbon. 1986, *24*, p.365,
- 24 Forgacs, E. and Cserhádi, T.: J. Chromatogr. A. 1998, *797*, p.33,
- 25 Foster, A.I., James, P.G., McCarrol, J.J., and Tennison, S.R.: British Patent No. 1565 074. vol 1. 1 London, 1980
- 26 Greenwood, N.N. and Earnshaw, A.: Chemistry of the elements. vol 1. 1 Oxford, Pergamon Press, 1994
- 27 Hennig, G.R.: Chemistry and Physics of Carbon. vol 1. 2th New York, New York Publisher, 1966
- 28 Henrion, R. and Henrion, G.: Multivariate Analyse: Methodik und Anwendungen in der Chemie und verwandten Gebieten. vol 1. 1 Frankfurt, Springer Verlag, 1994
- 29 Hermann, H., Schubert, Th., Gruner, W. and Mattern, N.: Nanostructured Materials. 1997, *8*,

- p.215,
- 30 Heyer, M.H. and Peter-Schloerb, F.: *Astrophysical Journal*. 1997, 475, p.173,
 - 31 Hoeskuldsson, A.: *J. Chemometrics*. 1988, 2, p.211,
 - 32 Juntgen, H.: *Fuel*. 1986, 65, p.1436,
 - 33 Kawashima, Y., and Katagiri, G.: *Phys. Rev.* 1995, B52, p.10053,
 - 34 Kissinger, H.E.: *Anal. Chem.* 1957, 29, p.1703,
 - 35 Knight, D.S., and White, W.B.: *J. Mater. Res.* 1989, 4, p.385,
 - 36 Khuri, A.I. and Cornell, J.A.: *Response Surfaces, Design, and Analyses*. vol 1. 3th New York, Marcel Dekker Inc., 1996
 - 37 Koch, C.C.: *Nanostructured Materials*. 1997, 9, p.13,
 - 38 Kroto, H.W., Heath, J.R., O'Brian, S.C., Curl, R.F., and Smalley, R.E.: *Nature*. 1985, 318, p.162,
 - 39 -: *International Tables for Crystallography*, . vol A. 3th London, Kluwer Academic Publishers, 1996
 - 40 Laidler, K.J.: *Reaction Kinetics*. vol 1. 5th Oxford, Pergamon Press Ltd., 1963
 - 41 Lefferts, L., van Ommen, J.G., and Ross, J.R.H.: *Appl. Catal.* 1987, 34, p.329,
 - 42 Maeda, M., Kuramoto, Y., and Hoire, C.: *J. Phys. Soc. Jpn.* 1979, 47, p.337,
 - 43 Marsh, H.: *Chem. Soc. - Spec. Publ.* 1977, 32, p.133,
 - 44 McFeely, F.R., Kowalczyck, S.P., Ley, L., Cavell, R.G., Pollak, R.A., and Shirley D.A.: *Phys. Rev.* 1974, B9, p.5268,
 - 45 Mennella, V., Monaco, G., Colangeli, L., and Bussoletti, E.: *Carbon*. 1995, 33, p.115,
 - 46 Mestl, G., Herzog, B., Schlögl R., and Knözinger, H.: *Langmuir*. 1995, 11, p.3207,
 - 47 Muolijn, J. A. and Kapteijn F.: *Carbon*. 1995, 33, p.1153,
 - 48 Nagy, A., Mestl, G., Rühle, T., Weinberg, G., and Schlögl, R.: *J. Catal.* 1998, 179, p.548,
 - 49 Nemanich, R. J. and Solin, S. A.: *Phys. Rev.* 1979, B20, p.392,
 - 50 Nicklow, R., Wakabayashi, N., and Smith, H.G.: *Phys. Rev.* 1972, B5, p.4951,
 - 51 Nisha, J. A., Yudasaka, M., Bandow, S., Kokai, F., Takahashi, K., and Iijima, S.: *Berlin EUROCARBON 2000 Proceedings*. Ed.: Carbon: vol 2. 1 Berlin, Carbon, 2000
 - 52 Niwase, K.: *Phys. Rev.* 1995, B52, p.15785,
 - 53 Niwase, K., Tanaka, T., Kakimoto, Y., Ishihara, K. N., and Shingu, P. H.: *Mat. Trans. JIM*. 1995, 36, p.282,
 - 54 Oswald, K.: *Handbuch der allg. Chemie*. vol 1. 1 Frankfurt, Springer Verlag, 1919
 - 55 Otto, M.: *Chemometrie: Statistik und Computereinsatz in der Analytik*. vol 1. 1 Weinheim, AVCH Verlag Weinheim, 1997
 - 56 Rodriguez-Reinoso, F.: *Carbon*. 1998, 36, p.159,
 - 57 Rühle, Thomas: *Mechanische Aktivierung*, PhD.. vol 1. 1 Berlin, 1997
 - 58 Rühle, T., Herein, D., Weinberg, G., Pfänder, N., and Schlögl, R.: *Ber. Bunsen Gesellschaft*. 2001, 36, p.9,
 - 59 Sanchez-Cortezon, E., Schoonmaker, R., Wild, U., Herein, D. and Schlögl, R.: *Oxygen activation on amorphous materials for the partial oxidation of methanol*. *Carbon*. 2003 erscheint vorr.,

- 60 Schadler, L. S., Amer, M. S., and Iskandarani, B.: Mech. Materials. 1996, 23, p.205,
- 61 Schlögl, R.: Handbook of Heterogeneous Catalysis. vol 1. 2th Frankfurt, VCH Verlag, 1995
- 62 Schlögl, R. and Boehm, H.P.: Carbon. 1983, 21, p.345,
- 63 Schrader, R., Deren, J., Fritsche, B., and Ziolkowski, J.: Z. Anorg. Allg. Chem.. 1970, 25, p.379,
- 64 Schubert, H., Guntow, U., Hofmann, K., and Schlogl, R.: Fresenius Journal of Analytical Chemistry. 1996, 356, p.127,
- 65 Schwarz, R.B. and Johnson, W. L.: Phys. Rev. Lett.. 1983, 51, p.415,
- 66 Shriver, D.F., Atkins, P.W. and Langford, C.H.: Inorganic Chemistry. vol 1. 5th Oxford, Oxford University Press, 1990
- 67 Singer, I.L.: J. Vac. Sci. Technol. A. 1994, 12, p.5,
- 68 Spielbauer, D.: Appl. Spectrosc.. 1994, 44, p.776,
- 69 Steinike, U. and Hennig, H.P.: KONA. 1992, 10, p.15,
- 70 Stoehr, J.: NEXAFS Spectroscopy. vol 1. 4th Berlin, Berlin Springer-Verlag, 1992
- 71 Taguchi, G.: Introduction to Quality Engineering.
vol : Designing Quality into Products and Processes. 1, 5th, Tokio, Asian Productivity Organisation p.1986,
- 72Tamman, G.Z. Elektrochem.19293521
- 73Tang, J., Zhao, W., Li, L., Falster, A. U., Simmon, W. B., Zhou, W. L., Ikuhara, Y., and Zhang, J.H. J. Mat. Res.1996113
- 74Thomas, J.M., Evans, E. L., Barber, M., and Swift,P.J. Chem. Soc. Faraday Trans.1971671875
- 75Tuinstra, F. and Koenig, J. L.J. Chem. Phys.1970531126
- 76UllmanEncyclopedia of Industrial Chemistry15thFrankfurtSpringer Verlag1988
- 77Vainshtein, B.K.Structure Analysis by electron diffraction12thOxfordPergamon Press1964
- 78van Heel, M.J. Mol. Biol.1991220877
- 79Vidano, R.P., Fischbach, D. B., Willis, L. J., and Loehr, T. M.S. Stat. Commun.198139341
- 80Walker, P.L., Hart, P. J., and Vastola, F. J.Chemistry and Physics of Carbon-Fundamentals of Gas-Surface Interaction12thNew YorkAcademic Press1967
- 81Weeber, A.W., and Bakker, H.Physica B198815393
- 82Weeks, M.E.J. Chem. Educ. Publ.195612
- 83Welham, N.J. and Williams, J. S.Carbon1998361309
- 84Wilhelm, H., Lelaurain, M., McRae, E., and B. Humbert, B.J. Appl. Phys.1998846552
- 85Wimmers, O.J., Arnoldy, P., and Moulijn, J.A.J. Phys. Chem.1986901331
- 86Windig, W. and Markel, S.J. Mol. Struct.1992292161
- 87Wold, S., Esbensen, K., and Geladi, P.Chem. Int. Lab. Syst.1987237
- 88Yang, T. and Wong, C.Science1981214437
- 89Young, J.A. and Koppel, J.U.J. Chem. Phys.19651281120

11 Lebenslauf

Name: Emilio Sanchez-Cortezon

16. 11/1973 Geboren in Alicante/Spanien

7/1979 -- 6/1987 Grundschule Vistahermosa de la Cruz in Alicante/Spanien

7/1987 -- 6/1989 Jesus y Maria-Gymnasium in Alicante/Spanien

7/1989 -- 6/1991 Inmaculada Concepcion Jesuiten-Gymnasium in Alicante/Spanien

6/1991 Abitur

7/1991 -- 6/1996 Studium der Chemie an der Universitaet von Alicante/Spanien

10/1996 -- 3/1997 Praktikum BAYER AG in Leverkusen/Deutschland

4/1997 -- 11/2000 Doktorand am Fritz-Haber-Institut in Berlin/Deutschland

12/2000 -- 02/2002 ZeTek Power SAS in Le Bourget Du Lac/Frankreich

02/2002 --Heute Independent Power Technologies SAS in Le Bourget Du Lac/Frankreich